Lattice QCD studies of Upsilon physics

Iain D. Kendall

School of Physics and Astronomy, Glasgow University

Thesis submitted to the University of Glasgow
for the degree of Doctor of Philosophy
September 2010

Abstract

Non-Relativistic QCD (henceforth NRQCD) is a non-relativistic effective theory that models the strong interaction. We use this formulation to perform lattice simulations of the bound states of b quarks, known as the Υ spectrum. These simulations are performed on a range of gauge ensembles provided by the MILC collaboration that include three flavours of quark content - one at the approximate mass of the strange quark, and two degenerate flavours that range from about a half to a tenth of the mass of the strange quark.

We implement a random wall algorithm in the creation of our b quark propagators, and develop a technique to combine the random wall with smearing functions, which are used to assist in picking out the relevant quantum numbers in the the resulting meson correlator. This is the first time these techniques have been used in this manner.

We employ a Bayesian fitting procedure to extract energies and amplitudes from our simulated correlators. By using the $2S-1S$ Υ splitting on each configuration, and matching to experimental results, we are able to extract the lattice spacings for each ensemble from which we determine the heavy quark potential scale parameter r_1. In concert with results from our collaborators, we outline the procedure for combining multiple determinations of r_1, and present the collaborative result. We then use this parameter in a determination of the strong coupling constant α_s in the $\overline{MS}$ scheme.

We investigate the dispersion relation of the NRQCD action, and note some undesirable features that we are able to resolve with the precision attainable using the random wall. We look at a number of ways to address these issues, including non-perturbative and perturbative tuning of coefficients. Using the perturbative coefficients, we then proceed to calculate heavy-heavy currents, which are perturbatively matched to the continuum, and allow us to give results for the Υ leptonic width.

Acknowledgements

I would like to thank my supervisor, Christine Davies, for her support, guidance, patience and insight throughout the process of creating this thesis. I would also like to thank the other members of the Glasgow PPT group. In particular, I would like to thank Andrew Davies for the QFT tutorials he provided, Eric Gregory, Craig McNeile, Kit Wong and Rachel Dowdall for many helpful discussions, and Jonna Koponen for all the support and advice that helped me get through my final year. Thanks also to my fellow students who have come and gone during the course of this research: David Thompson, Peter Athron, Dan Guise and Luo Rui.

Further afield, I would like to thank the staff at the Fermilab computing centre for all their computing assistance in the course of running my simulations.

Finally, I would like to express my appreciation of everyone in the HPQCD collaboration.

Declaration

" I declare that, with the exception of chapters 1, 2 and 3 or where explicit reference is made to the contribution of others, that this thesis is the result of my own work and has not been submitted for any other degree at the University of Glasgow or any other institution."

Contents

List of Figures

List of Tables

Chapter 1

Introduction

1.1 Standard Model & Motivation

Our current understanding of the nature of particle physics is encompassed in The Standard Model (henceforth, the SM). In this model, matter is composed of elementary particles called *quarks* and *leptons*, and the interactions between these particles is mediated by the *gauge bosons*. These particles are tabulated in Table 1.1.

Quarks	Charge (e)	Mass	Spin	Leptons	Charge (e)	Mass (MeV)	Spin
u	$+2/3$	1.5 - 3.3 MeV	1/2	e	-1	$0.510998910 \pm 1.3 \times 10^{8}$	1/2
d	$-1/3$	3.5 - 6 MeV	1/2	ν_e	0	< 0.460	1/2
c	$+2/3$	$1.27^{+0.07}_{-0.11}$ GeV	1/2	μ	-1	$105.658367 \pm 4 \times 10^{6}$	1/2
s	$-1/3$	105^{+25}_{-35} MeV	1/2	ν_μ	0	< 0.19	1/2
t	$+2/3$	$171.3 \pm 1.1 \pm 1.2$ GeV	1/2	τ	-1	1776.84 ± 0.17	1/2
b	$-1/3$	$4.2^{+0.17}_{-0.07}$ GeV	1/2	ν_τ	0	< 18.2	1/2
Gauge Bosons	Charge (e)	Mass	Spin		Charge (e)	Mass (GeV)	Spin
γ	0	0	1	$W^{\pm}$	1	80.398 ± 0.025	± 1
g	0	0	1	Z	1	91.1876 ± 0.0021	1

Table 1.1: Particles of the Standard Model [1].

Quantum field theory has been highly successful in making calculations and predictions

of the Weak and Electromagnetic interactions of the SM (those interactions mediated by the $Z/W^{\pm}$ and γ respectively). This is largely due to the fact that one can employ perturbation theory to the study of these forces, a process which involves making an expansion in the coupling constant of the relevant governing theory. Such a process will only work if the coupling constant is small; in the case of the strong force, governed by Quantum Chromodynamics, this is frequently not the case.

When studying bound states of quarks, the running of the coupling constant brings it too close to 1 for perturbation to be valid, and so one requires a non-perturbative, first principles method to proceed. Lattice QCD is such a method.

The last decade or so has been an important time for lattice QCD. While the principles of the approach to QCD were developed in the 1970's, computing power at that time was inadequate for handling the calculations necessary to make a realistic calculation. The statistical nature of lattice techniques is very costly in terms of processing; as are the difficulties associated with making the vacuum polarisation quark masses sufficiently small and, indeed, the effort required to include such quarks at all. However, since the 1970's many algorithmic improvements have been made, while, at the same time, the technology available for processing has improved dramatically; and what was once inconceivable is now possible.

1.2 Quantum Field Theory

1.2.1 Path Integrals

Feynman showed in 1948 that the expectation values of the physical observables in a quantum field theory can be calculated using path integrals to compute time-ordered products of the theory's fields, called *correlation functions*.

$$\langle 0|T(\phi(x_1)\dots\phi(x_n)|0\rangle = \frac{\int(\mathcal{D}\phi)\phi(x_1)\dots\phi(x_n)e^{iS}}{\int(\mathcal{D}\phi)e^{iS}} \tag{1.1}$$

where the T operator time-orders the fields; and S is the action of the theory, which comes from the Lagrangian Density, $\mathcal{L}(\phi, \partial_\mu\phi)$

$$S = \int d^4x\mathcal{L}(\phi, \partial_\mu\phi) \tag{1.2}$$

Such a path integral is over all values of $\phi(x)$, over all values of x - resulting in an integral with an uncountably infinite number of degrees of freedom, due to the continuous nature of space-time. These infinities must be removed by regularising the theory, which can be achieved by imposing a space-time lattice. This approach, applied to the theory of Quantum Chromodynamics, is the basis of this thesis.

1.2.2 Quantum Chromodynamics

Quantum Chromodynamics (QCD) is the Standard Model theory used to describe the strong force. It is described by a *gauge theory* based in SU(3) group theory. Gauge theories are those theories which are invariant under local gauge transformations, and are used in the SM to describe the electromagnetic, weak and strong forces.

The Lagrangian of QCD is given by

$$\mathcal{L} = \bar{\psi}^i(x)(i\gamma^\mu\partial_\mu - m)\psi^i(x) - \frac{1}{4}F^a_{\mu\nu}F^{\mu\nu}_a, \tag{1.3}$$

where the index i denotes flavour and

$$\bar{\psi}(x) = \psi^\dagger(x)\gamma^0 \tag{1.4}$$

The field strength tensor in the Lagrangian is given by equation 1.5, in which the f^{abc} are the SU(3) structure constants [7].

$$F^a_{\mu\nu} = \partial_\mu A^a_\nu - \partial_\nu A^a_\mu + gf^{abc}A^b_\mu A^c_\nu \tag{1.5}$$

We require that the Lagrangian is symmetric under the gauge transformation

$$\psi(x) \rightarrow e^{i\alpha_a(x)\frac{\lambda^a}{2}}\psi(x) \tag{1.6}$$

where λ_a are the eight Gell-Mann matrices - the generators of SU(3) in the fundamental representation. These are related to the eight gluons from table 1.1, which transform as the adjoint representation of SU(3). Invariance under this local phase rotation necessitates replacing ∂_μ with $\mathcal{D}_\mu$, the covariant derivative. $\mathcal{D}_\mu$ is defined as:

$$\mathcal{D}_\mu = \partial_\mu - i\frac{\lambda_a}{2}A^a_\mu(x). \tag{1.7}$$

The field A^a_μ transforms as

$$A^a_\mu \rightarrow A^a_\mu - \frac{i}{g}\partial_\mu\alpha_a(x) \tag{1.8}$$

While our theory is gauge invariant, it can be useful to impose a particular gauge, depending on one's purpose. This is done by imposing a constraint on the field A_μ. There are many possibilities, but notable gauges are the *Landau* (equation 1.9) and *Coulomb* (equation 1.10) gauges defined below, where the Greek index denotes space-time and the Roman index denotes only space:

$$\partial_\mu A_\mu = 0 \tag{1.9}$$

$$\partial_i A_i = 0 \tag{1.10}$$

The lattice version of Coulomb gauge is used for the vast majority of work in this thesis, and Landau is used on occasion, for example for defining the parameter u_0 (see equation 2.33).

1.2.3 Consequences

The gluon fields couple to the quarks via the colour charge g, a quantum number also carried by the gluon fields themselves. The non-abelian nature of SU(3) adds a self-interaction between these fields, and this unusual feature is believed to be connected to the other special features of QCD.

First, there is the phenomenon known as *confinement* - coloured states are not observed, only colour singlets (either 3 quarks of differing colour bound together [baryons], or a quark and anti-quark of complimentary colour/anti-colour [mesons]). These singlet states are known collectively as hadrons.

QCD also features *asymptotic freedom* - the coupling constant in QED, for example, decreases as the scale increases. The situation for QCD is the opposite - the coupling decreases with *decreasing* distance scale. This means that, as small distances (high energies) the particles are essentially free. This also means that perturbation theory is only applicable at high energies, and not at the internal energy scales of the hadrons we wish to study.

Chapter 2

Lattice Methodology

2.1 Discretisation

As described in section 1.2, imposing a discrete lattice on to Quantum Field Theory allows us to regularise otherwise infinite numbers of degrees of freedom in the path integrals. This was first demonstrated by Wilson [8] in 1975. Such a lattice, of spatial volume L^3 and temporal extent T, takes the form:

$$\Lambda = \{x | x \in a\mathbb{Z}^4; x^{1,2,3} = 0, a, ..., a(L-1); x^4 = 0, a, ..., a(T-1)\}, \tag{2.1}$$

where a is the spacing between adjacent lattice points.

Fermion fields are only defined on the lattice points x_μ, and thus derivatives simply become differences:

$$\Delta_\mu \psi(x) = \frac{1}{a}(\psi(x + a\hat{\mu}) - \psi(x)) \tag{2.2}$$

$$\Delta^*_\mu \psi(x) = \frac{1}{a}(\psi(x) - \psi(x - a\hat{\mu})) \tag{2.3}$$

$$\delta_\mu \psi(x) = \frac{1}{2}(\Delta_\mu \psi(x) + \Delta^*_\mu \psi(x)) = \frac{1}{2a}(\psi(x + a\hat{\mu}) - \psi(x - a\hat{\mu})) \tag{2.4}$$

The gluon fields are defined on the links between these lattice points, which will be discussed later.

With only a finite number of fields, the path integral becomes well-defined:

$$\langle 0|T(\phi(x_1)\dots\phi(x_n)|0\rangle = \frac{\int(\prod_i d\phi_i)\phi(x_1)\dots\phi(x_n)e^{iS}}{\int(\prod_i d\phi_i)e^{iS}} \tag{2.5}$$

2.2 Minkowski to Euclidean Space

Since our goal is to simulate the integral numerically, we must deal with the imaginary exponent e^{iS} in 2.1 as the oscillations resulting from this term that will otherwise make our goal impossible. This can be done via a *Wick Rotation*, moving from Minkowski space to Euclidean. The appropriate changes are:

$$x_M^0 = -ix_E^4 \tag{2.6}$$

$$\gamma_0^M = \gamma_4^E \tag{2.7}$$

$$\gamma_i^M = -i\gamma_i^E \tag{2.8}$$

$$A_M^0 = -iA_E^4 \tag{2.9}$$

$$\partial_M^0 = i\partial_E^4 \tag{2.10}$$

$$D_M^0 = iD_E^4, \tag{2.11}$$

which changes the Lagrangian (suppressing the E subscript henceforth) to

$$\mathcal{L} = \bar{\psi}^i(x)(\gamma^\mu\partial_\mu + m)\psi^i(x) - \frac{1}{4}F^a_{\mu\nu}F_a^{\mu\nu}, \tag{2.12}$$

and the exponent becomes e^{-S}.

2.3 Monte Carlo

Having discretised the problem on to a lattice, we are now left with a finite, albeit large, number of degrees of freedom. In such a situation, one finds Monte Carlo techniques

particularly well suited to finding a numerical approximation to the integral.

Monte Carlo involves generating a random sample of the integrand phase-space, which are then averaged over. An operator, $\mathcal{O}$ is approximated as:

$$\langle \mathcal{O} \rangle = \frac{\Sigma_{i=1}^{N} \mathcal{O}_i e^{-S_i}}{\Sigma_{i=1}^{N} e^{-S_i}} \tag{2.13}$$

The technique chosen to generate such a sample can have a profound effect on the efficiency of the Monte Carlo integration. The most natural method for doing this would be a flat distribution, however this proves to be inefficient as most of the contributions to the sum comes from those configurations that minimise S. It makes sense, then, to use *importance sampling* to generate configurations with a probability related to their weight in the sum: e^{-S}.

A simple method of doing this is the *Metropolis algorithm* [9], described below:

- Create a starting configuration, C_1.
- Suggest a small change to C_1, giving C_2.
- Compute $dS = S(C_2) - S(C_1)$.
- Accept the suggested change, and replace C_1 with C_2 if $e^{-dS} \geq R$, where R is a random number in the range $[0, 1]$.
- Repeat.

The procedure usually starts with a "thermalisation" step at the beginning, where a number of cycles are performed to initialise the starting C before configurations are recorded. Additionally, only every n'th configuration is recorded, where n is chosen before production. This helps to ensure that two adjacent stored configurations will not be overly auto-correlated.

This algorithm works well for gluon configurations in the quenched approximation (an approximation to QCD in which the only quarks are the valence quarks, see section 2.9), but for what we require, more sophisticated algorithms are used [10].

2.4 Regularising QCD on a lattice

The description of the regularisation of a theory using a lattice has been relatively general thus far. We will now look at the specifics of placing the QCD fermion (quark) and gauge (gluon) fields on to the lattice.

The gauge fields, in the path integral language of section 1.2.1, serve to add a phase to a fermion as it travels a path from position x_1 to x_2. On a lattice, this path is made up of discrete steps, taking a fermion from x to $x + \hat{\mu}$. We can then define *parallel transport fields* linking adjacent lattice sites. This is the natural way to codify the lattice gauge fields, $U_\mu(x)$:

$$U_\mu(x, x+\hat{\mu}) = U_\mu(x) \equiv \mathcal{P} \exp\left(ig \int_x^{x+\hat{\mu}} A_\mu dx^\mu\right) \tag{2.14}$$

The link $U(x+\hat{\mu}, x)$, the link reverse link from $x+\hat{\mu}$ back to x would then be $U_{-\mu}(x+\hat{\mu}) = U_\mu^{-1}(x) = U_\mu^\dagger(x)$ (the last equality because U is unitary).

The U matrices transform under gauge transformations in a straight-forward way:

$$U_\mu(x) \to G(x) U_\mu(x) G^{-1}(x+\hat{\mu}), \tag{2.15}$$

which means that any closed loop of these matrices is gauge invariant - for example the *plaquette*, which is a 1×1 square of lattice links:

$$U_{plaq} = U_\mu(x) U_\nu(x+\hat{\mu}) U_\mu^\dagger(x+\hat{\nu}) U_\nu^\dagger(x). \tag{2.16}$$

The action for the gauge field needs to be gauge invariant, so it makes sense to write it in terms of such loops, giving rise to the Wilson gauge action:

$$S_G = \beta \sum_{plaq} \left(1 - \frac{1}{3} \mathrm{ReTr} U_{plaq}\right) \tag{2.17}$$

where $\beta = \frac{6}{g^2}$. In the continuum limit (that is: $a \to 0$), this will tend towards the $\frac{1}{4}\int d^4x F^a_{\mu\nu}F^{\mu\nu}_a$ term that comes from equation 2.12.

For the fermions $\psi(x)$, we look at the Dirac equation (in Euclidean space), which is of the form:

$$\overline{\psi}(x)(\gamma^\mu\partial_\mu + m)\psi(x). \tag{2.18}$$

On the lattice, the fermion fields are only defined on the lattice sites x_μ, becoming $\psi(x_\mu)$, and the Dirac equation becomes

$$\sum_{i,j,\mu}\overline{\psi}(x_i)\left(\frac{1}{2}(\delta_{i,j-\hat{\mu}} - \delta_{i,j+\hat{\mu}}) + m\delta_{i,j}\right)\psi(x_j), \tag{2.19}$$

where $\delta_{m,n}$ is the Kronecker-δ function:

$$\delta_{m,n} = \left(\frac{1}{2\pi}\right)^4 \int_{-\pi}^{\pi} d^4p e^{ip(m-n)} \tag{2.20}$$

Using the Fourier transform, we find the free propagator to be

$$\sum_\mu i\gamma^\mu \sin(p_\mu) + m. \tag{2.21}$$

As expected from the mass shell condition ($p^2 + m^2 = 0$), the propagator has a pole when $p = m = 0$, however, since the sine function is symmetrical under $p_\mu \to \pi = p_\mu$ it also has poles when $m = 0$ and $p_\mu = \pi$, i.e at the corners of the Brillouin zone. This causes each momentum state to be doubled for each μ, leading to 16 states instead of just one. These degenerate states are referred to as "tastes" since they do not represent true physical flavours. [11].

A solution to the doubling problem was suggested by Wilson himself. One may add an irrelevant operator to the action, with the intention of giving the doublers in the corners of the Brillouin zone an infinite mass [12].

$$S_F^{(W)} = S_F - \frac{r}{2}\sum_x \overline{\psi}(x)\Delta^{(2)}\psi(x), \tag{2.22}$$

where r is the Wilson parameter, and $\Delta^{(2)}$ is the lattice Laplacean:

$$\Delta^{(2)} = \sum_\mu \nabla^*_\mu\nabla_\mu\psi = \frac{1}{a^2}\sum_\mu \left(\psi(x+\hat{\mu}) + \psi(x-\hat{\mu}) - 2\psi(x)\right). \tag{2.23}$$

This extra term vanishes linearly with a as $a \to 0$. We can then write the Wilson Action as:

$$\begin{aligned} S_W &= \sum_{i,j,\mu} \overline{\psi}(x_i) \left(\frac{1}{2}(\delta_{i,j-\hat{\mu}} - \delta_{i,j+\hat{\mu}}) + m\delta_{i,j} \right) \psi(x_j) - \sum_{i,j,\mu} \psi(x_i) \left(\frac{r}{2}(\delta_{i,j-\hat{\mu}} + \delta_{i,j+\hat{\mu}} + 2\delta_{i,j}) \right) \psi(x_j) \\ &= \sum_{i,j} \overline{\psi}(x_i) \left(-\frac{1}{2} \sum_{\mu} [(r-1)\delta_{i,j-\hat{\mu}} + (r+1)\delta_{i,j+\hat{\mu}}] + (m+4r)\delta_{i,j} \right) \psi(x_j) \end{aligned} \tag{2.24}$$

Which means the free propagator is:

$$\begin{aligned} & \textstyle\sum_\mu i \sin(p_\mu) + m + \quad r \sum_\mu (1 - \cos(p_\mu)) \\ = \; & \textstyle\sum_\mu i \sin(p_\mu) + m + \quad 2r \sum_\mu \sin^2(\frac{p_\mu}{2}) \end{aligned} \tag{2.25}$$

We then get (with a shown explicitly now):

$$M(p) = m + \frac{2r}{a} \sum_{\mu} \sin^2(p_\mu a/2). \tag{2.26}$$

This has the desired property that for p_μ not in the corners of the Brillouin zone, $M(p) \to M$ as $a \to 0$, but for $p_\mu \approx \pi/a$ (the momentum of the doublers) the expression diverges, decoupling them from the physics of the problem. Unfortunately, we have lost chiral symmetry by adding the Wilson term for any $r \neq 0$, even when $M = 0$.

2.5 Lattice Path Integrals and Correlators

The discrete path integral from section 2.1, written specifically for QCD takes the form

$$\langle \mathcal{O} \rangle = \frac{\int \prod_{i,j,k} dU_i d\overline{\psi}_j d\psi_k \mathcal{O} e^{-S_{LQCD}}}{\int \prod_{l,m,n} dU_l d\overline{\psi}_m d\psi_n e^{-S_{LQCD}}}. \tag{2.27}$$

The Monte Carlo techniques from section 2.3 cannot proceed directly for this equation because the fermion fields are Grassmann variables, and these cannot be represented as numbers on a computer. We can, however, integrate the quark fields by hand, which will then allow for the application of the Monte Carlo procedure.

For a Gaussian integral involving Grassmann numbers θ and θ^* and an hermitian matrix B with eigenvalues b_i [13],

$$\left(\prod_i \int d\theta_i^* d\theta_i\right) e^{-\theta_i^* B_{ij} \theta_j} = \left(\prod_i \int d\theta_i^* d\theta_i\right) e^{-\Sigma_i \theta_i^* b_i \theta_i} = \prod_i b_i = \det(B) \quad (2.28)$$

$$\left(\prod_i \int d\theta_i^* d\theta_i\right) \theta_k \theta_l^* e^{-\theta_i^* B_{ij} \theta_j} = \det(B) B_{kl}^{-1} \quad (2.29)$$

Therefore, writing $S = S_g + S_f$ where the subscripts represent *gluonic* and *fermionic*, we get

$$\int \prod_{i,j,k} dU_i d\overline{\psi}_j d\psi_k \mathcal{O} e^{-S_{LQCD}} = \int \prod_{i,j,k} dU_i d\overline{\psi}_j d\psi_k \mathcal{O} e^{-(S_g+S_f)} = \int \prod_{i,j,k} dU_i d\overline{\psi}_j d\psi_k \mathcal{O} e^{-(S_g+\overline{\psi} M(U) \psi)} \quad (2.30)$$

in which we can replace the fermionic integral with $\det M(U)$. Any fermion fields that appear in $\mathcal{O}$ can be changed to quark propagators M^{-1} by invoking equation 2.29. This results in

$$\langle \mathcal{O} \rangle = \frac{\int \prod_i dU_i \det(M) \mathbf{O} e^{-S_g}}{\int \prod_j dU_j \det(M) e^{-S_g}}, \quad (2.31)$$

where $\mathbf{O}$ is now a time-ordered operator containing only gauge fields and quark propagators.

2.6 Improvement schemes

2.6.1 Tadpole Improvement

Tadpole diagrams appear in lattice perturbation theory due to higher order terms that allow multiple gluons to couple to a single quark, terms that have no analogue in the continuum where only a single gluon may couple to a quark. These terms cause renormalisations, which causes problems with lattice perturbation theory, it is therefore important to remove their contribution. [14]

If we can evaluate the mean contribution of these tadpoles, we can remove them if we simply make the change:

$$U_\mu \to \frac{U_\mu}{u_0} \tag{2.32}$$

The mean field factor u_0 can be evaluated by several means, such as the mean Landau link:

$$u_0 = \overline{\frac{1}{3}\mathrm{ReTr}(U_\mu)} \tag{2.33}$$

when the U_μ fields are in Landau gauge, or from the average plaquette [15]

$$u_0 = \left\langle \frac{1}{3}\mathrm{Tr}(U_{plaquette}) \right\rangle^{1/4}, \tag{2.34}$$

the former being favoured [16], and the method used through out this thesis.

2.6.2 Symanzik Improvement

When calculating a physical quantity using the lattice, the usual method for finding the continuum limit is to simulate at multiple values of the lattice spacing a, and extrapolate $a \to 0$. Typically, a lattice simulation will not have a large enough number of different values of a to do this satisfactorily because of the high computational cost of generating and then simulating on such a large number of gauge configurations, particularly since the cost of generating an ensemble becomes very high for small value of a.

To remedy this, Symanzik suggested [17] modifying the lattice action in such a way as to improve the approach to the $a = 0$ limit. Writing the lattice action in a way that explicitly demonstrates the a spacing dependence, (where $\mathcal{L}_k$ for $k > 0$ are local operators of dimension $k + 4$):

$$S_{eff} = \int d^4x \sum_{k=0}^{\infty} a^k \mathcal{L}_k(x) = \int d^4x \mathcal{L}_{QCD}(x) + \int d^4x \sum_{k=1}^{\infty} a^k \mathcal{L}_k(x), \tag{2.35}$$

Symanzik realised that one could add operators to the action with the sole purpose of cancelling the terms dependent on a, hastening the theory's approach to the continuum.

2.6.3 Improvement of the gluon action

The action given previously for gluons is correct up to $\mathcal{O}(a^2)$. This can be improved by adding additional loops to the action composed of higher numbers of links [18]. This can be done using two 6-link operators, illustrated in figure 2.1. The action becomes correct up to $\mathcal{O}(a^2\alpha_s^2, a^4)$, with the coefficients of the new terms being computing by matching physical quantities to the continuum theory. The new action takes the form:

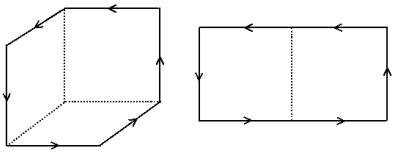

Figure 2.1: Corner-cube and rectangular gauge loops.

$$
\begin{aligned}
S &= \beta \sum_{x,\mu>\nu} \left(1 - \frac{1}{3}\mathrm{ReTr}U^{\mathrm{plaq}}_{\mu\nu}\right) && (2.36)\\
&+ \beta_{\mathrm{rect}} \sum_{x,\mu>\nu} \left(1 - \frac{1}{3}\mathrm{ReTr}U^{\mathrm{rect}}_{\mu\nu}\right) && (2.37)\\
&+ \beta_{\mathrm{rect}} \sum_{x,\mu>\nu} \left(1 - \frac{1}{3}\mathrm{ReTr}U^{\mathrm{rect}}_{\nu\mu}\right) && (2.38)\\
&+ \beta_{\mathrm{cc}} \sum_{x,\mu>\nu>\sigma} \left(1 - \frac{1}{3}\mathrm{ReTr}U^{\mathrm{cc}}_{\mu\nu\sigma}\right) && (2.39)
\end{aligned}
$$

Tadpole improvement has a large effect on the coefficients of these new terms [18].

2.6.4 Improvement of the Wilson fermion action

The simple Wilson action given in equation 2.22 has errors at $\mathcal{O}(a)$, as shown in equation 2.35. To account for these through to the next order, one must account for the $\mathcal{O}(5)$ operators responsible for this error and add appropriate counter-terms [19]. At this order, there are only two such operators that satisfy the criterion of preserving the symmetries

of the Lagrangian. These are:

$$i\overline{\psi}\sigma_{\mu\nu}F^{\mu\nu}\psi \text{ and } \overline{\psi}\left(D_\mu D^\mu + D_\nu D^\nu\right)\psi \tag{2.40}$$

although the latter is unnecessary and can be absorbed in to scaling of the mass. The former motivates making an addition to the Wilson action, so that we get:

$$S = S_{Wilson} + a^5 \sum_x c_{SW}\overline{\psi}(x)\frac{i}{4}\sigma\mu\nu\hat{F}_{\mu\nu}(x)\psi(x), \tag{2.41}$$

where the $\hat{F}_{\mu\nu}$ term is called the clover term, related to the plaquette, and arises from a symmetric definition of the lattice field tensor:

$$\hat{F}_{\mu\nu}(x) = \frac{1}{8a^2}\{Q_{\mu\nu}(x) - Q_{\nu\mu}(x)\}, \tag{2.42}$$

$Q_{\mu\nu}$ is the sum of the fields illustrated in figure 2.2. The choice of c_{SW} must be appropriate to achieve the desired level of improvement, and can be calculated either perturbatively or non-perturbatively. It is 1 at tree-level, giving an action correct through to $\mathcal{O}(a^2)$. This improvement was first suggested by Sheikholeslami and Wohlert in 1985.

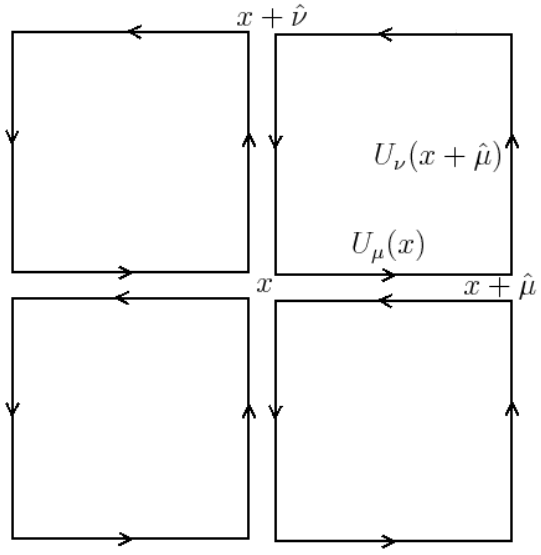

Figure 2.2: The cloverleaf arrangement of lattice gauge fields.

2.7 Staggered Quarks

Another method of addressing the doublers in the fermion action is by using *staggered quarks* [20, 21]. The doubling is caused by the fact that equation 2.21 vanishes at the corners of the Brillouin zone. If we can double the effective length of the zone, then we can dilute the doublers seen inside the lattice [12]. This is done by blocking the lattice in to hypercubes of size 2^4. Our treatment here follows [22].

The fields ψ in the naïve quark action are replaced by χ with the transformation

$$\begin{aligned} \psi(x) &\to \Omega(x)\chi(x) \\ \overline{\psi}(x) &\to \overline{\chi}(x)\Omega^\dagger(x) \end{aligned} \tag{2.43}$$

where

$$\Omega(x) \equiv \prod_{\mu=0}^{3} \gamma_\mu^{x_\mu}. \tag{2.44}$$

Expressing the naïve action in terms of the χ fields, we then get that

$$\overline{\psi}(x)(\gamma \cdot \Delta + m)\psi(x) = \overline{\chi}(x)(\alpha(x) \cdot \Delta + m)\chi(x). \tag{2.45}$$

$$\alpha_\mu(x) = \Omega^\dagger(x)\gamma_\mu\Omega(x+\mu) \tag{2.46}$$

which is diagonal in spinor space, and moreover every spin component of a χ field is equivalent to the other components.

For the naïve quark action, the doublers appear as

$$\psi(x) \to B_\zeta(x)\psi(x) \qquad \overline{\psi}(x) \to \overline{\psi}(x)B_\zeta^\dagger(x) \tag{2.47}$$

$$B_\zeta(x) \equiv \gamma_{\overline{\zeta}}(-1)^{\zeta\cdot x} \propto \prod_\rho (\gamma_5\gamma_\rho)\exp(ix\zeta\cdot\pi) \tag{2.48}$$

where $\zeta_\rho \in (\mathbb{Z}_2)^4$, giving 16 doublers (15 high momentum copies, plus the original fermion). A typical fermion field will contain contributions from all 16 of these fields, and hypercubic blocking can be used to (approximately) separate these. This procedure involves taking an average over a 2^4 hypercube within the lattice:

$$\psi_B^{(\zeta)} = \frac{1}{16}\sum_{\delta x \in (\mathbb{Z}_2)^4} \mathcal{B}_\zeta(x+\delta x)\psi(x+\delta x) \tag{2.49}$$

When $\zeta = 0$, the average will suppress contributions from ψ where $p \approx \pi$. For all $\zeta \neq 0$, the B operator will transform that component to $\zeta = 0$, and therefore the average will preserve that component and suppress everything else.

When one repeats this procedure in the staggered formulation, the factor of four reduction in the spinors translates in to a factor of four reduction in the doublers:

$$\psi_B^{(\zeta)} = \frac{1}{16} \sum_{\delta x \in (\mathbb{Z}_2)^4} \mathcal{B}_\zeta(x+\delta x)\psi(x+\delta x) = \sum_{\delta x} \gamma_{\delta x} B_\zeta(0) \begin{bmatrix} \chi_1(x+\delta x) \\ 0 \\ 0 \\ 0 \end{bmatrix} \tag{2.50}$$

where

$$\gamma_{\delta x} \equiv \prod_{\mu=0}^{3} (\gamma_\mu)^{\delta x_\mu}. \tag{2.51}$$

Since the $B_\zeta(0)$ operator can only permute the χ fields and multiply by ± 1 or $\pm i$, there can only be four independent $\psi_B^{(\zeta)}$, referred to as "tastes" of a quark. Further, the spinors' effect, each being equivalent, can be reduced to just one quark by taking the fourth root of the quark determinant. The validity of using the fourth root has been a topic of some controversy - in particular the locality of the operator, and so there remain some unanswered theoretical concerns regarding staggered quarks. Nevertheless, much empirical evidence exists that justifies the staggered formulation. This issue is beyond the scope of this thesis, and we simply assume that staggered quarks are valid on the basis of its many past successes. For an over-view of the situation, see [23, 24, 25, 26].

To complete the formulation of the staggered quark action, it must be Symanzik improved to remove $\mathcal{O}(a^2)$ errors. These errors appear because of taste changing interactions that do not occur in normal QCD. Consider a high momentum gluon ($p \approx \pi/a$) being absorbed by a quark; in QCD this would push the quark off-shell, but with staggered quarks it transforms the quark in to a different taste of an on-shell quark [27].

To correct for these taste-changing interactions, one may suppress high momentum quarks by using a precess dubbed "link fattening". A single link is replaced by a number

of different paths between the same two lattice sites consisting of 1-, 3-, 5- and 7-link terms, summarised in figure 2.3. An extra terms, the Lepage term, is then added to correct for low momentum errors caused by the addition of the previous extra terms. All of these terms are tadpole improved (as in equation 2.32). The Naik term [28] used to correct simple errors in Δ, and the resulting action is called the *ASQTAD action*.

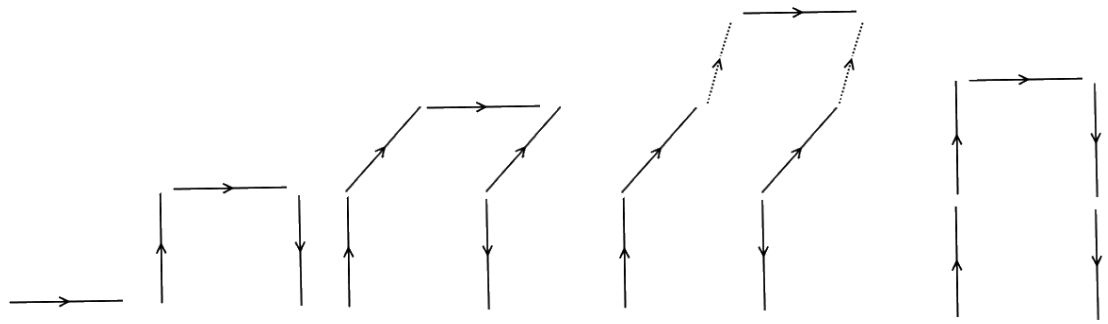

Figure 2.3: The fattened link staples, and the Lepage term (far right).

2.8 Highly-Improved Staggered Quarks

In recent years, the staggered quark action has been subject to further improvement, resulting in an even further improved action, known as Highly-Improved Staggered Quarks, or "HISQ". The goal of HISQ is to remove higher order taste-exchanging interactions than the tree-level corrections possible with staggered quarks. While simulations in this thesis do not use HISQ directly, HISQ is important to work that combines simulations from this thesis with that of collaborators, which will be described in chapter 4. Here, we outline the basic idea behind the HISQ action, following [11].

The link smearing of the ASQTAD action is effectively introducing a form factor to

suppress the taste changing interactions:

$$\begin{aligned} f_\mu(q) &\rightarrow 1, q \rightarrow 0 \\ f_\mu(q) &\rightarrow 0, q \rightarrow \zeta\pi/a \text{ where } \zeta^2 \neq 0, \zeta_\mu = 0. \end{aligned} \tag{2.52}$$

This form factor is implemented by replacing the gauge links U_μ with $\mathcal{F}_\mu U_\mu(x)$, where

$$\mathcal{F}_\mu \equiv \prod_{\rho\neq\mu} \left(1 + \frac{a^2\delta_\rho^{(2)}}{4}\right)$$

is the smearing operator, and the function $\delta_\rho^{(2)}$ approximates a covariant second-derivative.

$$\begin{aligned} \delta_\rho^{(2)} U_\mu(x) &\equiv \frac{1}{a^2}[U_\rho(x)U_\mu(x+a\hat{\rho})U_\rho^\dagger(x+a\hat{\mu}) - 2U_\mu(x) \\ &+ U_\rho^\dagger(x-a\hat{\rho})U_\mu(x-a\hat{\rho})U_\rho(x-a\hat{\rho}+a\hat{\mu})]. \end{aligned} \tag{2.53}$$

This works because $\delta_\rho^{(2)} \sim -4/a^2$ (which means $\mathcal{F} \sim 0$) when $q_\rho \approx \pi/a$.

The ASQTAD action also adds an additional term

$$\mathcal{F}_\mu \rightarrow \mathcal{F}_\mu - \sum_{\rho\neq\mu} \frac{a^2(\delta_\rho)^2}{2},$$

to cancel $\mathcal{O}(a^2)$ errors in $\mathcal{F}_\mu$. This is the Lepage term in figure 2.3.

Repeated application of the smearing operator further suppresses the taste-dependent properties, which is unsurprising as these have their roots in perturbation theory. Normally this would create new $\mathcal{O}(a^2)$ errors, but this does not occur when using the ASQTAD action, since it is already a^2 improved. Another problem of repeated application of $\mathcal{F}$ is that, if N is the number of terms in the smearing, two gluon vertices grow as $\sqrt{N}$ - enhancing 1 loop diagrams that have 2 gluon vertices. This can be entirely avoided if we reunitarise the gauge links, which we indicate with the operator $\mathcal{U}$.

Because of this, ASQTAD action can be further improved to form the HISQ action by applying the link smearing operation twice:

$$\mathcal{F}_{\text{HISQ}} = \left(\mathcal{F} - \sum_{\rho\neq\mu} \frac{a^2(\delta_\rho)^2}{2}\right) \mathcal{U}\mathcal{F}_\mu.$$

The HISQ action has been shown to be extremely useful for the simulation of charm quarks. In most discretisations, large errors occur unless $am \ll 1$, however the HISQ formulation has achieved an accuracy of a few percent for charm masses as high as $am_c \approx 1/2$. Without this improvement, the alternative would be to use an effective theory. This approach works well for b quarks (and is the basis of chapter 3) which are unquestionably "heavy", but not for charm, which are much lighter and occupy a niche between light and truly heavy quarks.

2.9 MILC configurations

The MILC collaboration have produced a large number of lattice ensembles on which QCD simulations may be performed. These range from lattice spacings of about 0.18fm down to 0.045fm. All spacings are merely approximate, as setting the scale is non-trivial; in fact much of the work of this thesis involves trying to make accurate scale determinations.

The gauge fields are simulated with an $\mathcal{O}(\alpha a^2)$ Symanzik improved action, and the asqtad improved staggered action ($\mathcal{O}(a^2)$ improved) was used for the vacuum polarization quarks (known as "sea quarks") [3].

Historically, *quenched configurations* were used in lattice simulations. Quenched configurations are produced without any sea quarks present, making them faster and easier to create. While removing the sea quarks from the theory can be economical, doing so compromises the consistency of the simulation and does not lead to realistic results. This is done by simply setting $\det(M) = 1$ (see section 2.5) during ensemble production.

Unquenched configurations - such as those produced by MILC - include sea quarks, although not necessarily using the accepted number of flavours (i.e. they are partially quenched), nor at the established masses. It is easy to justify the former - common ensembles of configurations include only the u, d and s quarks as the heavier quarks, having such high masses, have only very small effects on the theory as sea quarks. The

latter issue, the unphysical masses used, is a necessity of computing time and power - the calculation cost of configuration production (specifically, the computational cost of $\det(M)$) increases dramatically as sea quark mass falls. For the sake of feasibility, it is therefore generally wiser to simulate at a higher mass, and extrapolate final results to the physical limit. For this reason, numerous different quark masses are simulated for the same (approximate) lattice spacing.

Monte Carlo configurations are generated using, for example, algorithms such as Hybrid Monte Carlo for Wilson quarks, or, for Staggered quarks, the R Algorithm [10].

The configurations used in this thesis (see table 4.1) are of the "2+1" variety. This means that they include the s quark at approximately the correct mass, in addition to the u and d quarks at degenerate masses of approximately m_s to $m_s/10$; c, b and t sea quarks are omitted.

Other ensembles, created using different formulations, are available. In recent work by Stefan Meinel [29, 30], the same valence quark action used in this thesis was used to study b quarks on domain-wall lattices. The results are similar to those obtained here, lending weight to the validity of the staggered quark ensembles.

Chapter 3

Simulating Heavy Quark Mesons

3.1 Studying the Υ meson

Reliable lattice results are essential for various physics programmes, for example: limits on the CKM matrix. The B meson system in particular is used to access these CKM parameters. For this reason, the b quark needs to be well understood in lattice QCD; and so the Υ meson (and the bottomonium system) are therefore important to lattice QCD, as they allow us to test heavy quark lattice QCD actions.

The Υ system contains many "gold-plated[1]" states, which can be calculated accurately. Further, the Υ spectrum is also a useful system to study because its radial splitting (i.e. the splitting in which the two states are labelled by different radial excitation quantum numbers n, in this case 2S-1S) is a good quantity for setting the lattice spacing. Υ energy splittings (e.g. the 2S-1S or 1P-1S) are known to be insensitive to the heavy quark mass, which is important to obviate entering in to a circular problem between determining lattice spacing and lattice quark mass. As can be seen in figure 3.1, the energy splittings for the Υ (bottomonium) system and the ψ (charmonium) system approximately correspond to each other, despite the differences in mass between the constituent valence quarks. Each

[1]hadronically stable, narrow and experimentally well-characterised.

system's zero has been set to the mass of the spin average of the respective $\chi(^3P_{0,1,2})$:

$$M_\chi = \frac{M_{\chi_0} + 3M_{\chi_1} + 5M_{\chi_2}}{9} \tag{3.1}$$

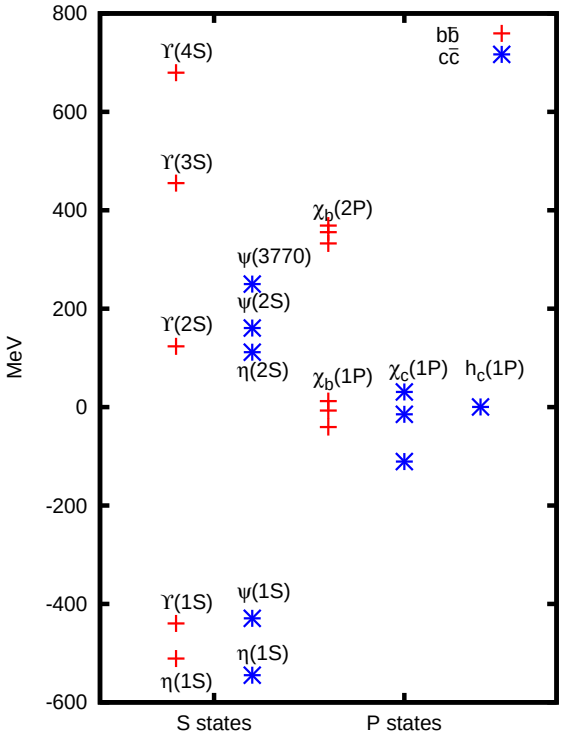

Figure 3.1: The heavy quarkonium systems.

Experimentally, the Υ was first found is 1977 at Fermilab, in proton/nuclei collisions [31]. Radiative decays of the $2S$ and $3S$ states in 1982-1983 subsequently led to the detection of the χ_b states [32, 33, 34]. In 2008, BaBar observed the η_b for the first time [35, 36].

It has been estimated [37] that, for an Υ meson, the b quark velocity, $v^2 \sim 0.1c^2$ due to the large mass of the b-quark. This property allows us to treat the Υ with a non-relativistic effective theory, and this is the basis of Non-Relativistic QCD (NRQCD). In this formulation, quark and anti-quark degrees of freedom are decoupled (we will use the symbol ψ for quarks and χ for anti-quarks), leading to two important consequences - the propagator has only one pole, avoiding a problem known as 'doubling' that plagues

other formulations (as in sections 2.4 and 2.7), and its evaluation is far simpler as it is first order in ∂_t [2].

3.1.1 Alternatives to NRQCD

NRQCD is not the only method currently being employed to simulate heavy valence quarks on the lattice. Before going in to detail about the NRQCD action used in this thesis, we briefly present some details of alternative approaches.

Heavy Quark Effective Theory

Heavy quark effective theory, or HQET (for a proper description, see for example [38]), treats the heavy quark as being infinitely heavy "static" colour source on the lattice, and then makes systematic corrections in $1/m_Q$ as a series expansion. In practice, carrying HQET out beyond $\mathcal{O}(1/m_Q)$ is very difficult, however corrections at this order are believed to be small because of the magnitude of the expansion parameter.

HQET does suffer a major drawback in that the statistical errors grow strongly with the time in the correlation functions, although current thinking does include avenues to overcome this problem.

Fermilab Heavy Quarks

The effective theory described in [39] is an alternative approach to describing heavy quarks, typically referred to as the Fermilab formulation. Here we will recount the superficial details, see [39] for a full treatment.

The Fermilab formulation is based on the Wilson action, and so treats doublers using the mechanism described in equation 2.22, however the Fermilab method differs in that it is designed to be able to handle both light and heavy quarks by including classes of interactions from both the small am_q and large m_Q/Λ_{QCD} limits in the effective Lagrangian of equation 2.35. To achieve this, they do not impose

a symmetry between interactions related by the exchanging a spatial axis with the temporal axis.

HISQ

Development of the HISQ formulation (described in section 2.8) is pushing the upper-bound on the quark masses that can be simulated to a point where they are approaching m_b. While not currently being used to simulate b quarks, HISQ may become viable for this purpose in the future. At present, HISQ is invaluable for simulations involving the charm quark, which would have previously been simulated with a heavy quark action such as NRQCD.

3.2 The NRQCD action

For a heavy-heavy system, there are three important scales to consider: the quark mass M_Q, momentum $p \sim M_Q v$ and kinetic energy $K \sim M_Q v^2$, with $M_Q >> M_Q v >> M_Q v^2$. The effective theory employs an ultra-violet cut-off at the order of the quark mass ($a \sim 1/M_Q$), exploiting the fact that the physics of the objects we are interested in, quark bound states, occurs at the scales of the momentum and energy (as evidenced by figure 3.1). This decreases the otherwise very broad spread of scales by allowing us to drop the mass term, and makes the problem tractable. Relativistic corrections may then be added by means of additional local interactions in the Lagrangian, because relativistic states are highly virtual and do not propagate long distances.

3.2.1 Building Blocks of NRQCD: Power Counting in the Continuum Effective Theory

The Lagrangian for a continuum effective theory may be found using a power counting argument following [2], using the various fields that can appear: ψ, ϕ, $A(x)$, and starting

with:

$$\mathcal{L}_{NRQCD} = \psi^\dagger(x)\left(iD_t + \frac{\mathbf{D^2}}{2M}\right)\psi(x) - \frac{1}{4}F_{\mu\nu}F^{\mu\nu}. \tag{3.2}$$

We have dropped the term $\psi^\dagger M\psi$, which has no effect on energy differences, serving only to shift the overall energy scale. This means that the "ground state" energy of a meson will not correspond to its mass, but rather its mass plus some unknown offset.

The number operator for heavy quarks has an expectation value of 1 for a heavy quark meson, localised within a region $\delta x \sim 1/p$. This means that we expect $\int d^3x \sim 1/p^3$; therefore:

$$\int d^3x\psi^\dagger(x)\psi(x) \sim 1 \Rightarrow \psi^\dagger(x)\psi(x) \sim p^3, \tag{3.3}$$

which means that $\psi \sim p^{3/2}$. Using this and the kinetic energy operator (which by definition has expectation value K):

$$\int d^3x\psi^\dagger(x)\frac{\mathbf{D}^2}{2M}\psi(x), \tag{3.4}$$

we can see that $\frac{\mathbf{D}^2}{2M} \sim K$ therefore

$$\mathbf{D} \sim (2MK)^{1/2} \sim p. \tag{3.5}$$

The field equation implies that

$$\left(iD_t + \frac{\mathbf{D}^2}{2M}\right)\psi = 0, \tag{3.6}$$

so that

$$D_t \sim \frac{\mathbf{D}^2}{2M} \sim K \tag{3.7}$$

Continuing specifically in the Coulomb gauge, which is the natural gauge for a non-relativistic problem (because the spatial gluon field is minimised and $\mathbf{D}^2$ is like $\mathbf{p}^2$ from the Schrödinger equation), we next observe that the vector potential $\mathbf{A}$ is small in this gauge, and therefore can be neglected in the field equation, which becomes:

$$\left(i\partial_t - g\phi(x) + \frac{\nabla^2}{2M}\right)\psi \approx 0. \tag{3.8}$$

The operator $g\phi$ is the operator through which the potential energy enters, and - as this is a bound system - it must balance the kinetic energy term. Therefore $g\phi(x) \sim K$ in Coulomb gauge.

The field equation for ϕ (with the vector potential neglected as before) would give us:

$$\nabla^2 g\phi(x) = -g^2\psi^\dagger(x)\psi(x) \Rightarrow g\phi(x) \sim \frac{1}{p^2}g^2p^3 \sim g^2p, \tag{3.9}$$

which is consistent with the previous assertion if the effective low energy coupling constant, $\alpha_s \sim g^2 \sim v$.

If we now include the vector potential in our solution for the field equations, we get that

$$(\partial_t^2 - \nabla^2)g\mathbf{A} = \frac{g^2}{M}\psi^\dagger\nabla\psi + g\phi\nabla g\phi + ... \tag{3.10}$$

Using our previous estimates, we can use this to estimate the order of the field A as

$$g\mathbf{A}(x) \sim \frac{1}{p^2}\left(\frac{g^2}{M}p^4 + pK^2\right) \sim vK. \tag{3.11}$$

Finally, we can estimate the nonabelian electric and magnetic fields:

$$\begin{aligned} g\mathbf{E} &= -\nabla g\phi + ... \sim pK \\ g\mathbf{B} &= \nabla \times g\mathbf{A} + ... \sim K^2 \end{aligned} \tag{3.12}$$

3.2.2 Building Blocks of NRQCD: Adding Correction Terms

The power counting of the previous section enables us to evaluate which correction terms are necessary to the leading order equation so that important quarkonium physics is not lost. It is sufficient to do this for the quark creation field, as charge-conjugation demands that the total action is invariant under the change $\psi \leftrightarrow \chi$, and this, like all symmetries of the theory, must be respected. Similarly; parity, gauge invariance, unitarity etcetera must be maintained, further restricting which interactions may appear in the action. For example, electric dipoles are forbidden due to parity, whereas magnetic dipoles are not.

Operator	Name	Power counting estimate
ψ	quark annihilation field	$(Mv)^{3/2}$
χ	anti-quark creation field	$(Mv)^{3/2}$
D_t	temporal covariant derivative	Mv^2
$\mathbf{D}$	spatial covariant derivative	Mv
$g\phi$	scalar potential (Coulomb gauge)	Mv^2
$g\mathbf{A}$	vector potential (Coulomb gauge)	Mv^3
$g\mathbf{E}$	chromoelectric field	M^2v^3
$g\mathbf{B}$	chromomagnetic field	M^2v^4

Table 3.1: Summary of estimates of operator magnitudes from power-counting argument for the NRQCD heavy quark action, given in terms of quark mass M and typical quark velocity v [2].

Terms that do match the symmetries of the theory may be added, up to whatever order we wish to work to. Any of these terms that includes a temporal derivative is inconvenient, as they make numerical evaluation much more difficult, but may be obviated by using the field equation for ψ to make the replacement

$$iD_t\psi(x) \sim \frac{-\mathbf{D}^2}{2M}\psi(x). \tag{3.13}$$

Bilinear corrections, suppressed by v^2 compared to the leading order, are required to achieve an accuracy of at least 10% for the Υ, and take the form

$$\begin{aligned}
\delta\mathcal{L}_{bilinear} &\equiv c_1\frac{1}{M^3}\psi^\dagger\mathbf{D}^4\psi \\
&+ c_2\frac{g}{M^2}\psi^\dagger(\mathbf{D}\cdot\mathbf{E}-\mathbf{E}\cdot\mathbf{D})\psi \\
&+ c_3\frac{ig}{M^2}\psi^\dagger\boldsymbol{\sigma}\cdot(\mathbf{D}\times\mathbf{E}-\mathbf{E}\times\mathbf{D})\psi \\
&+ c_4\frac{g}{M}\psi^\dagger\boldsymbol{\sigma}\cdot\mathbf{B}\psi
\end{aligned} \tag{3.14}$$

Next, we would add interactions involving a quark and an anti-quark through four-fermion contact terms, but these terms (equation 3.15) are not present in relativistic QCD,

and so must be suppressed to one loop order or beyond. Therefore, their coefficients are of order $\alpha_s^2(\pi/a)$ and are thus less significant than the bilinears. For this reason, they are not included.

$$\begin{aligned}\delta\mathcal{L}_{contact} &\equiv d_1\frac{1}{M^2}\psi^\dagger\chi\chi^\dagger\psi \\ &+ d_2\frac{1}{M^2}\psi^\dagger\boldsymbol{\sigma}\chi\cdot\chi^\dagger\boldsymbol{\sigma}\psi. \end{aligned} \tag{3.15}$$

There are also four-fermion terms in which the operators couple to coloured states:

$$\begin{aligned}\delta\mathcal{L}_{colour} &\equiv d_3\frac{1}{M^2}\sum_a\psi^\dagger T^a\chi\chi^\dagger T^a\psi \\ &+ d_4\frac{1}{M^2}\sum_a\psi^\dagger T^a\boldsymbol{\sigma}\chi\cdot\chi^\dagger T^a\boldsymbol{\sigma}\psi \end{aligned} \tag{3.16}$$

These are also less significant and are not included because not only are both d_3 and d_4 of order $\alpha_s^2(\pi/a)$, but additionally can only interact with a colour-singlet meson if the meson becomes coloured - which can only happen if the meson emits a virtual gluon, a process suppressed by a further v^2.

Finally, there exist additional spin dependent terms. As the first occurrence of non-trivial spin terms occurred at $\mathcal{O}(v^2)$ relative to the leading order, these correction terms must be taken to an additional power of v^2, i.e. $\mathcal{O}(v^4)$. We do not generally include these in our action, although they may become necessary to determine spin-dependent splittings to the desired accuracy (see chapter 5). These terms are

$$\begin{aligned}\delta\mathcal{L}_{spin} &\equiv f_1\frac{g}{M^3}\psi^\dagger\{\mathbf{D}^2,\boldsymbol{\sigma}\cdot\mathbf{B}\}\psi \\ &+ f_2\frac{ig}{M^4}\psi^\dagger\{\mathbf{D}^2,\boldsymbol{\sigma}\cdot(\mathbf{D}\times\mathbf{E}-\mathbf{E}\cdot\mathbf{D})\}\psi \\ &+ f_3\frac{ig^2}{M^3}\psi^\dagger\boldsymbol{\sigma}\cdot\mathbf{E}\times\mathbf{E}\psi. \end{aligned} \tag{3.17}$$

3.2.3 Relativistic Correction Coefficients

All of the corrections in the previous section contain unknown coefficients. Continuing in the manner of [2] one can compare QCD and NRQCD, matching the NRQCD coefficients

so that any predictions would agree with QCD (to v^2). We can make a very simple match to the formula for the relativistic energy for a non-interacting quark:

$$\sqrt{p^2 + M^2} \approx M + \frac{p^2}{2M} - \frac{p^4}{8M^3}, \tag{3.18}$$

which we recognise as the first of our bilinear corrections in equation 3.14; thus setting $c_1 = 1/8$.

Since many of our correction terms include gE, it makes sense to look next at the scattering of a quark from a static electric field in QCD.

$$T_E(p, q) = \overline{u}(q)\gamma^0 g\phi(q - p)u(p). \tag{3.19}$$

Substituting in the Dirac spinors, which are normalised non-relativistically, and look like:

$$u(p) = \left(\frac{E_p + M}{2E_p}\right)^{\frac{1}{2}} \begin{bmatrix} \psi \\ \frac{\boldsymbol{\sigma}\cdot\mathbf{p}}{E_p+M}\psi \end{bmatrix}, \tag{3.20}$$

(where $E_p \equiv \sqrt{p^2 + M^2}$), we obtain the following:

$$\begin{aligned} T_E(\mathbf{p}, \mathbf{q}) &= \sqrt{\frac{(E_p + M)(E_q + M)}{4E_pE_q}} \\ &\times \quad \psi^\dagger \left[1 + \frac{\mathbf{p}\cdot\mathbf{q} + i\boldsymbol{\sigma}\cdot\mathbf{p}\times\mathbf{q}}{(E_p + M)(E_q + M)}\right] g\phi(\mathbf{q} - \mathbf{p})\psi \\ &\equiv \quad S_E(\mathbf{p}, \mathbf{q}) + V_E(\mathbf{p}, \mathbf{q}), \end{aligned} \tag{3.21}$$

using the identity $(\boldsymbol{\sigma}\cdot\mathbf{p})(\boldsymbol{\sigma}\cdot\mathbf{q}) = \mathbf{p}\cdot\mathbf{q} + i\boldsymbol{\sigma}\cdot\mathbf{p}\times\mathbf{q}$. Expanding the scalar part of 3.21, S_E, in terms of $\mathbf{p}/M$ and $\mathbf{q}/M$, we see that

$$S_E(\mathbf{p}, \mathbf{q}) = \left(1 - \frac{(\mathbf{p} - \mathbf{q})^2}{8M^2}\right)\psi^\dagger g\phi(\mathbf{q} - \mathbf{p})\psi. \tag{3.22}$$

The latter term in equation 3.21 is the spin-dependent term, and this can also be expanded in the same terms.

$$V_E(\mathbf{p}, \mathbf{q}) = \left(\frac{i}{4M^2} - \frac{3i}{32M^4}(\mathbf{p}^2 + \mathbf{q}^2)\right)\psi^\dagger\boldsymbol{\sigma}\cdot(\mathbf{q}\times\mathbf{p})g\phi(\mathbf{q} - \mathbf{p})\psi \tag{3.23}$$

The first term of S_E is the scattering predicted by the lowest order action, but the others require the addition of new interactions to the NRQCD action:

$$\begin{aligned}\delta\mathcal{L}_E &= \frac{g}{8M^2}\psi^\dagger(\mathbf{D}\cdot\mathbf{E}-\mathbf{E}\cdot\mathbf{D})\psi \\ &+ \frac{ig}{8M^2}\psi^\dagger(\boldsymbol{\sigma}\cdot\mathbf{D}\times\mathbf{E}-\boldsymbol{\sigma}\cdot\mathbf{E}\times\mathbf{D})\psi \\ &+ \frac{3ig}{64M^4}\psi^\dagger\{\mathbf{D}^2,\boldsymbol{\sigma}\cdot\mathbf{D}\times\mathbf{E}-\boldsymbol{\sigma}\cdot\mathbf{E}\times\mathbf{D}\}\psi. \qquad (3.24)\end{aligned}$$

This sets the second and third terms in equation 3.14, so that $c_2 = c_3 = 1/8$, and also means that $f_2 = 3/64$ in equation 3.17.

We can repeat this calculation for the static vector potential $\mathbf{A}$, and from this $c_4 = 1/2$ and $f_1 = 1/8$. We can also make an expansion for the double scattering of a quark from an external static electric field, and doing so would give us the last coefficient: $f_3 = -1/8$.

3.2.4 Lattice NRQCD

By replacing the continuum fields in the NRQCD action with discrete counterparts, and derivatives with finite differences; we can reformulate NRQCD to Lattice NRQCD. If we wish to maintain our level of precision, we must make corrections to these discretisations at the same level as in the previous section. The field $F_{\mu\nu}$ is represented using the cloverleaf operators, discussed earlier(see diagram 2.2). The finite difference operators (also discussed previously, see equations 2.2 - 2.4 and 2.23) are given below with the lattice QCD fields explicitly included.

$$a\Delta_\mu^{(+)} = U_\mu(x)\psi(x+a\hat{\mu}) - \psi(x) \qquad (3.25)$$

$$a\Delta_\mu^{(-)} = \psi(x) - U_\mu^\dagger(x-a\hat{\mu})\psi(x-a\hat{\mu}) \qquad (3.26)$$

$$\Delta_\mu^{(\pm)} = \frac{1}{2}(\Delta_\mu^{(+)} + \Delta_\mu^{(-)}) \qquad (3.27)$$

$$\Delta^{(2)} = \sum_i \Delta_i^{(+)}\Delta_i^{(-)} = \sum_i \Delta_i^{(-)}\Delta_i^{(+)} \qquad (3.28)$$

The covariant derivatives of the $F_{\mu\nu}$ field then look like

$$\begin{aligned} a\Delta_\rho^{(+)}F_{\mu\nu}(x) &\equiv U_\rho(x)F_{\mu\nu}(x+a\hat{\rho})U_\rho^\dagger(x) - F_{\mu\nu}(x) \\ a\Delta_\rho^{(-)}F_{\mu\nu}(x) &\equiv F_{\mu\nu}(x) - U_\rho^\dagger(x-a\hat{\rho})F_{\mu\nu}(x-a\hat{\rho})U_\rho(x-a\hat{\rho}) \end{aligned} \tag{3.29}$$

$F_{\mu\nu}$ is then improved to $\mathcal{O}(a^4)$ by making the replacement

$$F_{\mu\nu}(x) \to F_{\mu\nu}(x) - \frac{a^2}{6}\left[\Delta_\mu^{(+)}\Delta_\mu^{(-)} + \Delta_\nu^{(+)}\Delta_\nu^{(-)}\right]F_{\mu\nu}(x), \tag{3.30}$$

which, upon expanding the lattice derivatives becomes

$$\begin{aligned} F_{\mu\nu}(x) &\to \frac{5}{3}F_{\mu\nu}(x) - \frac{1}{6}[U_\mu(x)F_{\mu\nu}(x+a\hat{\mu})U_\mu^\dagger(x) \\ &+ U_\mu^\dagger(x-a\hat{\mu})F_{\mu\nu}(x-a\hat{\mu})U_\mu(x-a\hat{\mu}) - (\mu \Leftrightarrow \nu)]. \end{aligned} \tag{3.31}$$

Tadpole improvement effects from the U_μ fields must be handled cautiously here, as there are in fact some cancellations occurring in the square-bracketed terms. Terms of the form $U_\mu F_{\mu\nu} U_\mu^\dagger$ would look like six link operators (since $F_{\mu\nu}$ is a four link operator), and are therefore tadpole improved by a factor of $1/u_0^6$, but the unitarity of U means that in some cases two adjacent U fields cancel, and it would then be correct to only tadpole improve by a factor of $1/u_0^4$. To achieve this, we add a correction term (where the factor of 2 is to account for the same error in the $\mu \Leftrightarrow \nu$ terms) [40]. This term is illustrated in figure 3.2.

$$2 \times -\frac{1}{6}\left(1 - \frac{1}{u_0^2}\right)F_{\mu\nu}(x) \tag{3.32}$$

The lattice chromoelectric and chromomagnetic fields are defined in terms of the clover-leaf field $F_{\mu\nu}$ as

$$E^i(x) = F_{0i}(x), \tag{3.33}$$

$$B^i = \frac{1}{2}\epsilon_{ijk}F_{jk}(x). \tag{3.34}$$

The discretised fields relate to the continuum versions with the relation

$$U_\mu(x) \equiv Pexp\left[-ig\int_x^{x+a\hat{\mu}} A\cdot dy\right], \tag{3.35}$$

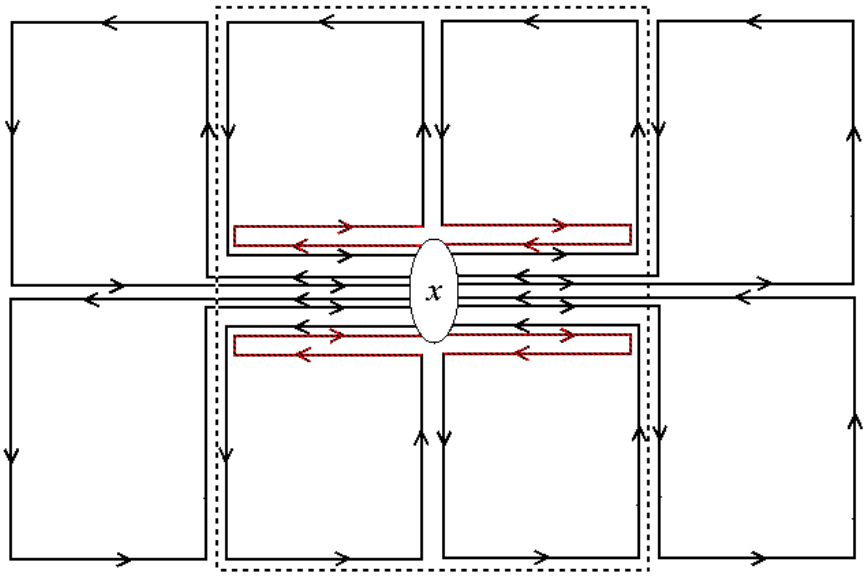

Figure 3.2: Schematic of $U_\mu(x)F_{\mu\nu}(x+a\hat{\mu})U_\mu^\dagger(x)$ (right four loops) and $U_\mu^\dagger(x-a\hat{\mu})F_{\mu\nu}(x-a\hat{\mu})U_\mu(x-a\hat{\mu})$ (left four loops). The red links cancel due to the unitarity of U_μ, leading to over-division by the tadpole improvement factor. The loops within the dashed box are therefore equivalent to $\frac{1}{u_0^2}F_{\mu\nu}$. This motivates making the correction $(1-\frac{1}{u_0^2})F_{\mu\nu}$

therefore, the difference operators would relate as

$$a\Delta_i^{(+)} \equiv exp(aD_i) - 1 = aD_i + \frac{a^2}{2}D_i^2 + \frac{a^3}{6}D_i^3... \tag{3.36}$$

$$a\Delta_i^{(-)} \equiv 1 - exp(-aD_i) = aD_i - \frac{a^2}{2}D_i^2 + \frac{a^3}{6}D_i^3... \tag{3.37}$$

which gives

$$a\Delta^{(\pm)} = \frac{1}{2}(\Delta^{(+)} + \Delta^{(-)}) = aD_i + \frac{a^3}{6}D_i^3. \tag{3.38}$$

We can suitably improve this operator by making the change

$$\Delta_i^{(\pm)} \to \Delta_i^{(\pm)} - \frac{a^2}{6}\Delta_i^{(+)}\Delta_i^{(\pm)}\Delta_i^{(-)}, \tag{3.39}$$

and, in the same fashion, improve the Laplacian by

$$\Delta^{(2)} \to \Delta^{(2)} - \frac{a^2}{12}\sum_i [\Delta_i^{(+)}\Delta_i^{(-)}]^2. \tag{3.40}$$

Finally, the temporal derivative needs to be addressed. The fact that NRQCD is non-relativistic allows for a simpler treatment of temporal derivatives than the spatial ones. Temporal derivatives have only appeared to the first power, which makes the problem one of initial value rather than boundary conditions, and thus less computationally costly to solve. If we were to improve the temporal derivative in the same way as we have the spatial, then this advantage would be lost, as we would have introduced higher powers of the derivative term. Instead, we can examine the evolution equation for a quark Green function, and make the correction there.

The quark evolution operator, at leading order, would take the form

$$G(\mathbf{x}, t+a; \mathbf{x}_0, t_0) = U_0^\dagger(\mathbf{x}, t)(1 - aH_0)G(\mathbf{x}, t; \mathbf{x}_0, t_0), \tag{3.41}$$

where $H_0 = \sum_i \frac{\Delta_i^{(+)}\Delta_i^{(-)}}{2Ma}$; this means that in momentum space, the expression is

$$G(\mathbf{p}, t+a; t_0) = \left(1 - \sum_i \frac{4\sin^2\frac{p_i a}{2}}{2Ma}\right) G(\mathbf{p}, t; t_0). \tag{3.42}$$

This is a problem, because if $\mathbf{p}_i \approx \pi/a$ then

$$G(\mathbf{p}|_{\mathbf{p}_i=\pi/a}, t+a; t_0) \approx \left(1 - \frac{12}{2Ma}\right) G(\mathbf{p}, t; t_0), \tag{3.43}$$

which is potentially unstable: if $(1 - \frac{12}{2Ma}) < -1$ or $(1 - \frac{12}{2Ma}) > 1$, then the expression will grow with time. This can only happen when $Ma < 3$.

If we replace $(1 - aH) \to (1 - aH/n)^n$ then these high momentum quark states are suppressed (and for a heavy quark meson, we expect these states to contribute little to the masses of the meson), but low momentum behaviour remains the same. The instability criterion becomes $nMa < 3$, and, as we are free to choose n, can be avoided as long as we make n suitably large.

$$G(\mathbf{x}, t+a; \mathbf{x}_0, t_0) = \left(1 - \frac{aH_0}{2n}\right)^n U_0^\dagger(\mathbf{x}, t) \left(1 - \frac{aH_0}{2n}\right)^n G(\mathbf{x}, t; \mathbf{x}_0, t_0), \tag{3.44}$$

For the sake of convenience, we have also split the operator into two parts (relabelling $n \to 2n$ in the process). This move is valid, and equivalent at tree level to the previous

formulation, but infers some advantages, particularly at the start and end points of a simulation.

Neglecting the gauge field in equation 3.44 for now, we can make a correction to the temporal derivative by observing that

$$G(\mathbf{x}, t+a) = \left(1 - \frac{aH_0}{2n}\right)^{2n} G(\mathbf{x}, t) = e^{-aH_{eff}} G(\mathbf{x}, t), \tag{3.45}$$

$$H_{eff} = -\frac{2n}{a} \log\left(1 - \frac{aH_0}{2n}\right) = H_0 + \frac{a}{4n} H_0^2, \tag{3.46}$$

which means that the temporal derivative can be corrected with the replacement $H_0 \rightarrow H_0 - \frac{a}{4n} H_0^2$. The correction $\frac{a}{4n} H_0^2 \sim a(Mv^2)^2 \sim aM^2 v^4$, and can be implemented with the term

$$\frac{a(\Delta^{(2)})^2}{16nM^2} \tag{3.47}$$

Ultimately, these corrections give rise to a quark evolution equation, given below. The c_i are functions of α_s (the strong coupling constant) and aM (the valence quark mass in lattice units), but are 1 at tree level [41], which is the value used in this work unless otherwise stated.

$$\begin{aligned}
G(\mathbf{x}, t+a) &= \left(1 - \frac{aH_0}{2n}\right)^n \left(1 - \frac{a\delta H}{2}\right) U_\mu^\dagger(\mathbf{x}, t) \left(1 - \frac{a\delta H}{2}\right) \left(1 - \frac{aH_0}{2n}\right)^n G(\mathbf{x}, t) \\
H_0 &= \frac{-\Delta^{(2)}}{2M} \\
\delta H &= -c_1 \frac{(\Delta^{(2)})^2}{8M^3} + c_2 \frac{ig}{8M^2} (\mathbf{\Delta}^{(\pm)} \cdot \tilde{\mathbf{E}} - \tilde{\mathbf{E}} \cdot \mathbf{\Delta}^{(\pm)}) \\
&- c_3 \frac{g}{8M^2} \sigma \cdot (\mathbf{\Delta}^{(\pm)} \times \tilde{\mathbf{E}} - \tilde{\mathbf{E}} \times \mathbf{\Delta}^{(\pm)}) \\
&- c_4 \frac{g}{2M} \sigma \cdot \tilde{\mathbf{B}} + c_5 \frac{a^2 \Delta^{(4)}}{24M} - c_6 \frac{a(\Delta^{(2)})^2}{16nM^2}
\end{aligned}$$

where the operators with tildes have been tadpole improved.

3.3 Simulation of the Υ Meson

The quark and anti-quark propagators we have derived can then be used in combination to produce mesons. Since $\psi^\dagger$ and $\chi^\dagger$ create a quark and an anti-quark respectively, one

can create a meson with the operator

$$\mathcal{O}^\dagger(t) = \sum_{x_1,x_2} \psi^\dagger(\mathbf{x_1}, t)\Gamma(\mathbf{x_1} - \mathbf{x_2})\chi^\dagger(\mathbf{x_2}, t) \tag{3.48}$$

The Γ operator is responsible for picking the correct quantum numbers for the meson, and makes use of a smearing function (see section 4.3) which helps to select the correct radial quantum number n. Γ is also responsible for selecting the correct spin orientations, by means of either the identity matrix for the η_b, or σ_i for the Υ.

A meson propagating from 0 to t is given by the two-point correlation function $\left\langle 0|\mathcal{O}(t)\mathcal{O}^\dagger(0)|0\right\rangle$. Since the propagator for the quark is given by $\left\langle 0|\psi(\mathbf{y}, t)\psi^\dagger(\mathbf{x}, 0)|0\right\rangle$, and the anti-quark propagator is simply the complex conjugate, we can write the meson propagator as

$$G_{meson}(t) = \sum_{\mathbf{y_1},\mathbf{y_2}} \mathrm{Tr}\left[G^\dagger(\mathbf{y_2}, t)\Gamma^{\dagger(sk)}\ (\mathbf{y_1} - \mathbf{y_2})\widetilde{G}(\mathbf{y_1}, t)\right] \tag{3.49}$$

where

$$\widetilde{G}(\mathbf{y}, t) = \sum_{\mathbf{x}} G(\mathbf{y} - \mathbf{x}, t)\Gamma^{(sc)}(\mathbf{x}) \tag{3.50}$$

and the sum over the initial anti-quark position has been removed by translational invariance. The trace is over spin and colour. This expression represents a meson being created at time 0 with smearing $\Gamma^{(sc)}$, propagating to time t and being destroyed with smearing $\Gamma^{(sk)}$ [42].

3.4 Fitting

3.4.1 Correlator Functional Form

In order to make fits to the simulation results, it is useful to investigate the general form of the correlator functions.

Consider an operator in the Heisenberg representation, $O_H(t)$. Then an Υ propagating from $t = 0$ to $t = T$ would take the form

$$_H\Big\langle 0|O_H(T)O_H^\dagger(0)|0\Big\rangle_H . \tag{3.51}$$

In Euclidean space, this is related to the time-dependent Schrödinger representation by

$$\begin{aligned} _H\Big\langle 0|O_H(T)O_H^\dagger(0)|0\Big\rangle_H &\equiv {}_H\Big\langle 0|\tau^\dagger(T)O_S\tau(T)O_S^\dagger|0\Big\rangle_H \\ &\equiv {}_S\Big\langle 0, t=T|O_S\tau(T)O_S^\dagger|0, t=0\Big\rangle_S , \end{aligned} \tag{3.52}$$

where the operator $\tau(t) \equiv e^{-Ht}$. [43]

Inserting a complete set of states $\sum |n\rangle\langle n| = 1$, we get that

$$\begin{aligned} & {}_S\Big\langle 0, t=T\Big|O_S\tau(T)O_S^\dagger\Big|0, t=0\Big\rangle_S \\ \equiv & \sum_n {}_S\Big\langle 0, t=T\Big|O_S e^{-E_nT}\Big|n\Big\rangle\Big\langle n\Big|O_S^\dagger\Big|0, t=0\Big\rangle_S \\ \equiv & \sum_n \Big|\,\big\langle 0\big|O_S\big|n\big\rangle\,\Big|^2 e^{-E_nT}. \end{aligned} \tag{3.53}$$

Therefore, the generalised functional form to fit a correlator would look like

$$G(t; A_n, E_n) = \sum_{n=0}^{\infty} A_n^2 e^{-E_n t} \tag{3.54}$$

where A_n is the matrix element $\Big|\,\big\langle 0\big|O_S\big|n\big\rangle\,\Big|$, and we define the index n so that E_n are ordered from low energy to high. Clearly, it would be impossible to fit to the infinite number of exponentials that make up this function, but it is not necessary to do so. As t increases, higher energy states become suppressed far more quickly than the lower ones, and at high values of t, the function is dominated by the low energy contributions. The most significant energy is therefore E_0, and this can be extracted from the *effective mass*, defined as

$$M_{eff}(t) = \ln \frac{G(t)}{G(t+1)}. \tag{3.55}$$

As $t \to \infty$, $M_{eff} \to E_0$, so one would expect a plot of M_{eff} against time to plateau at the ground-state energy (for an example, see figure 3.3). This would normally correspond to the meson mass, but due to the formulation of NRQCD, this is not the case here (see section 3.2.1). The exact rate at which this occurs will depend on the smearing function used in the quark creation operators. This simple technique will allow easy access to the ground-state, but in this work we are interested in higher energy levels, particularly in the $E_1 - E_0$ splitting, so we will need to make use of a more advanced fit.

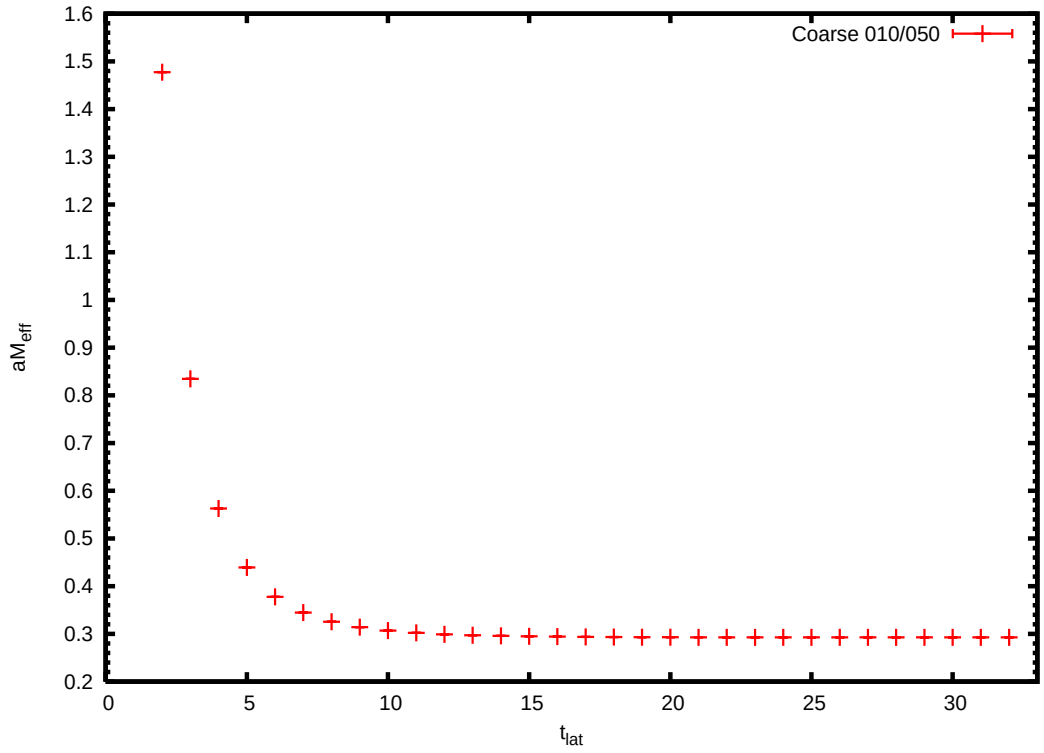

Figure 3.3: Effective mass plot for the Υ on the "coarse" 010/050 MILC ensemble.

3.4.2 Bayesian Fitting

Bayesian fitting techniques use *priors* to provide a fit with physical information. By including such information, such as the ordering of the energy levels and the expected size of excited state splittings, one can reliably fit an arbitrarily high number of exponentials. Fitting an excess of parameters (relative to the quality of the data being fitted) will not

degrade the errors or fit quality of those parameters that are well-described by the data.

A normal fitting procedure would attempt to fit to

$$G_{th}(t; A_n, E_n) = \sum_n A_n e^{-E_n t}, \tag{3.56}$$

by minimising a χ^2 defined as

$$\chi^2(A_n, E_n) \equiv \sum_{t,t'} \Delta G(t) \sigma^{-2}_{t,t'} \Delta G(t'), \tag{3.57}$$

in which

$$\Delta G(t) \equiv \overline{G(t)} - G_{th}(t; A_n, E_n), \tag{3.58}$$

and the covariance matrix is

$$\sigma^2_{t,t'} \equiv \overline{G(t)G(t')} - \overline{G(t)}\ \overline{G(t')}. \tag{3.59}$$

The over-bars indicate the Monte Carlo estimator, given by ensemble averages.

The Bayesian technique minimises an augmented χ^2 as follows:

$$\chi^2 \to \chi^2_{aug} \equiv \chi^2 + \chi^2_{prior} \tag{3.60}$$

defining χ^2_{prior} as:

$$\chi^2_{prior} \equiv \sum_n \frac{(A_n - \bar{A}_n)^2}{\tilde{\sigma}^2_{A_n}} + \sum_n \frac{(E_n - \bar{E}_n)^2}{\tilde{\sigma}^2_{E_n}}$$

The terms in χ^2_{prior} push the fit towards A_n and E_n in the ranges $\bar{A}_n \pm \tilde{\sigma}_{A_n}$ and $\bar{E}_n \pm \tilde{\sigma}_{E_n}$ respectively. The $\bar{A}_n$'s, $\bar{E}_n$'s and the $\tilde{\sigma}$'s are chosen to reflect reasonable a priori knowledge of these values [44].

The augmentation of χ^2 can be justified using Bayes' Theorem, and the assumption that the probability of getting a particular set of Monte Carlo data G given a set of parameters is Gaussian distributed $P(G|p) \propto e^{-\chi^2(p)/2}$, and that the probability of getting a particular set of parameters, p, is also Gaussian distributed with $P(p) \propto e^{-\chi^2_{prior}(p)/2}$.

We want to know the probability of getting a particular set of parameters, p, given the Monte Carlo data we are fitting to, that is $P(p|G)$. Bayes' Theorem gives:

$$P(p|G) = \frac{P(G|p)P(p)}{P(G)} \propto P(G|p)P(p) \propto e^{-\chi^2(p)/2} e^{-\chi^2_{prior}(p)/2} = e^{-\chi^2_{aug}(p)/2}$$

implying that the fit parameters are distributed according to χ^2_{aug}, consistent with equation 3.60 [44].

The fitting procedure utilises an increasing number of exponentials as the fit progresses, and is expected to become stable once a sufficiently large number of such exponentials is included, see figure 3.4. This means that once the number of exponentials is high enough to describe all states meaningfully present in the correlator, the addition of extra superfluous states does not have any impact on the fit for the lowest levels. As long as enough are fitted that the error stabilises, we can be confident that our error includes the full effect from the uncertainty associated with the higher state parameters; which would not be the case had we used a smaller number of exponentials.

All of the fitting in this thesis was done using a Python script written by G. Peter Lepage.

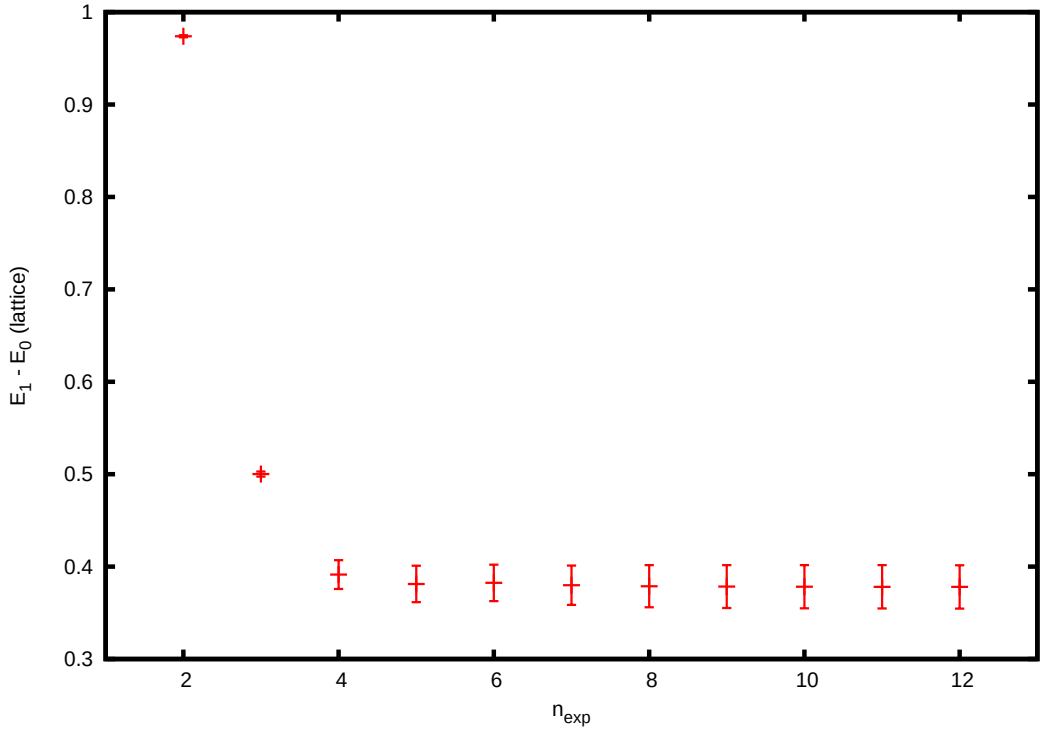

Figure 3.4: Fitting of the energy splitting $E_1 - E_0$ for an Υ point-to-point source calculated on the 010/050 MILC ensemble. As successive exponentials are added to the fit, the result and associated error stabilise.

Chapter 4

Υ Spectroscopy

4.1 Introduction

The configurations used in this thesis were generated by the MILC Collaboration [3, 45] [46], and their properties are tabulated in table 4.1.

The values of aM_b^0 are the bare-quark mass used for each ensemble, and were determined as described in section 4.4 and are consistent with the values used in similar work by Alan Gray [4]; u_{0L} is the value used for tadpole improving the simulation (equation 2.32) and is taken from the mean Landau link (equation 2.33), see section 4.2. The value of the NRQCD stability parameter n (see section 3.2.4, equation 3.44) was chosen to be appropriate for the "superfine" ensembles, and kept consistent across the set of ensembles to allow for more meaningful comparison.

In order to increase statistics, multiple time origins were used on each configuration. Origins are spaced maximally apart on the lattice, the first origin is at $t = 0$, and each subsequent origin is located T/N_{origin} time-slices later, where T is the ensemble's time extent, and N_{origin} is the number of origins used for that ensemble. The results from these origins were binned together prior to any analysis.

Lattice	V. Coarse		Coarse		Fine	Superfine
Size	$16^3 \times 48$	$16^3 \times 48$	$20^3 \times 64$	$24^3 \times 64$	$28^3 \times 96$	$48^3 \times 144$
n_f	2+1	2+1	2+1	2+1	2+1	2+1
β	6.572	6.586	6.760	6.760	7.090	7.470
$au_{0P}m_{u,d}$	0.0097	0.0194	0.010	0.005	0.0062	0.0036
$au_{0P}m_s$	0.0484	0.0484	0.050	0.050	0.031	0.018
u_{0L}	0.8218	0.8225	0.8359	0.8362	0.8541	0.8695822
aM_b^0	3.40	3.40	2.80	2.80	1.95	1.34
n	4	4	4	4	4	4
Configs	631	631	595	202 / 2083*	557	698
Origins	24	24	32	32	8	8

Table 4.1: Summary of MILC ensemble parameters[3] 'Configs' is the number of configurations used in this work, and may not represent the total number of configurations in existence for that ensemble. *initial runs were done on an easily accessible subset of ensembles, due to computation cost, storage availability and time constraints.

It is important to bin together data from the same configuration (but different start times), and in principle even to bin together data from adjacent configurations due to *auto-correlations*. The method for generating configurations means that a given configuration is not independent, but rather derived from the preceding configurations. If the number of Monte Carlo iterations between stored configurations in an ensemble is too small, then one would expect simulations on sequential configurations to be correlated. One would also expect correlations between simulations conducted on different starting times of the same configuration, particularly if the number of alternate start times means that the distance between each is less than the simulation time extent, as is the case in this thesis (typical simulation times are $\sim$ 32 time slices, and typical origin separations are only ~ 2). Even if autocorrelations do exist in repeated simulations on a single configuration, such simulations are still valuable. Auto-correlated results still add to the accuracy of the simulation, just not by as much as an uncorrelated measurement as there can still be *some* information there. The binning process allows us to make use of auto-correlated

measurements without over-estimating their significance.

To test for auto-correlations, a series of simple 1×1 Bayesian fits were produced on a selection of ensembles, each binned in four different manners. First, each is fitted with no binning, then half the origins/configuration per bin, all the origins/configuration per bin, and finally with each bin consisting of all the origins for two consecutive configurations in each bin.

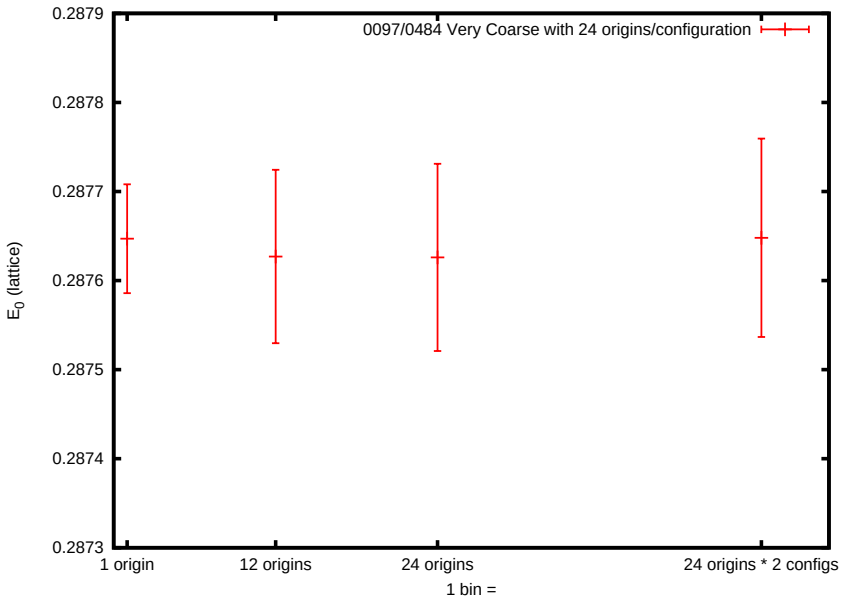

Figure 4.1: Testing for autocorrelations: plot of fit results for E_0 against bin size for the "very coarse" 0097/0484 ensemble.

In practice, the MILC configurations used here were binned over repeated uses of the same configuration. It is clear from plots 4.1 - 4.6 that even if this is unnecessarily binned, doing so does not hurt the result, whereas failing to bin can lead to under estimation of errors.

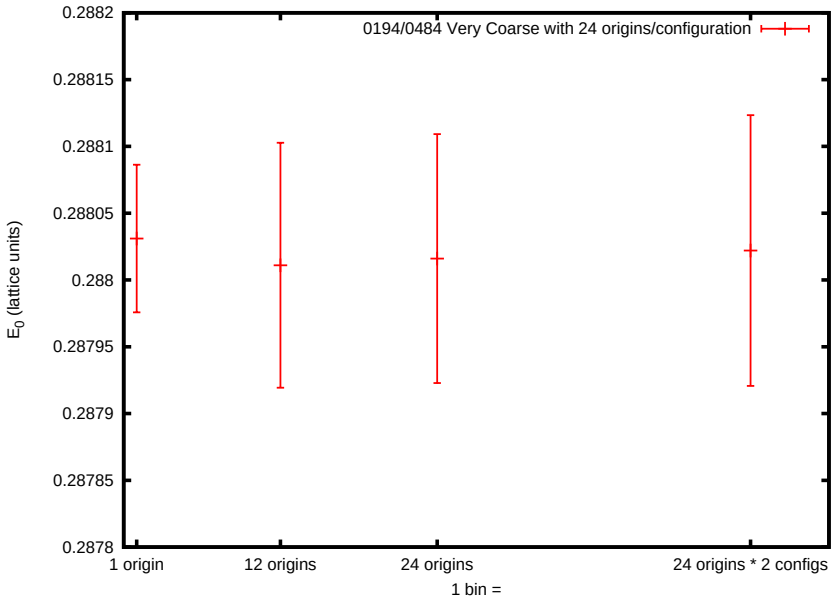

Figure 4.2: Testing for autocorrelations: plot of fit results for E_0 against bin size for the "very coarse" 0194/0484 ensemble.

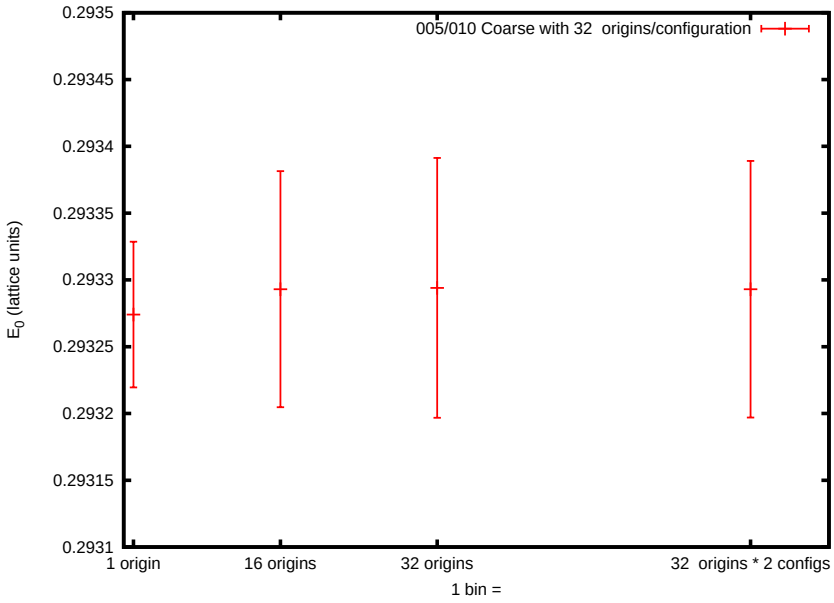

Figure 4.3: Testing for autocorrelations: plot of fit results for E_0 against bin size for the "coarse" 005/050 ensemble.

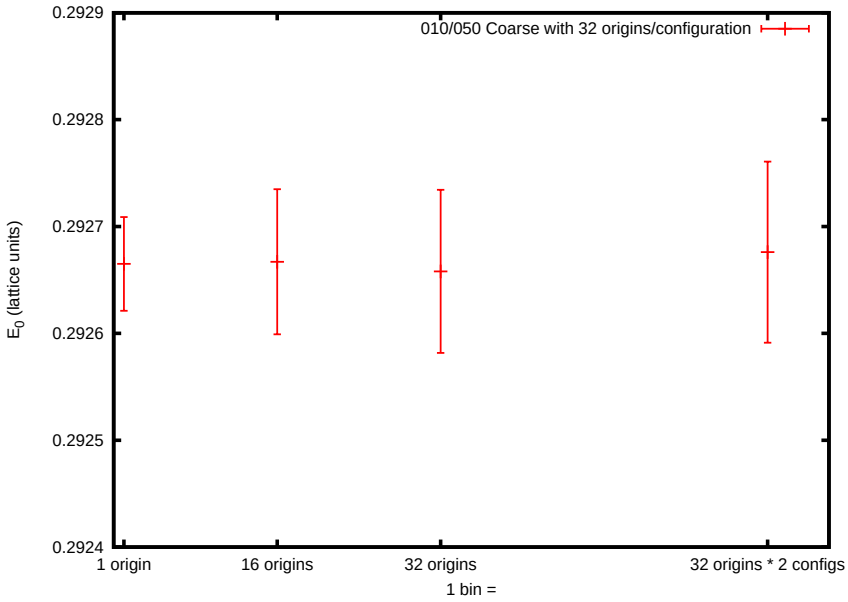

Figure 4.4: Testing for autocorrelations: plot of fit results for E_0 against bin size for the "coarse" 010/050 ensemble.

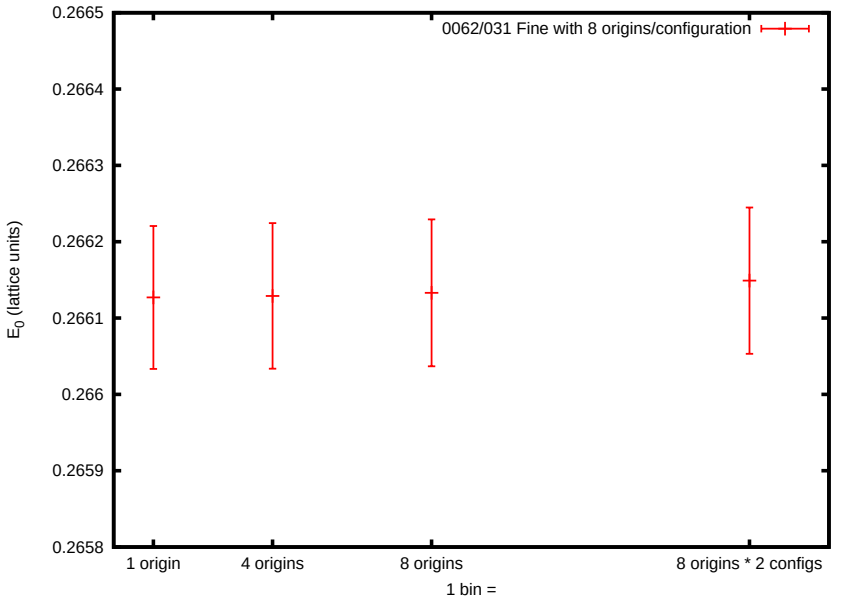

Figure 4.5: Testing for autocorrelations: plot of fit results for E_0 against bin size for the "fine" 0062/031 ensemble.

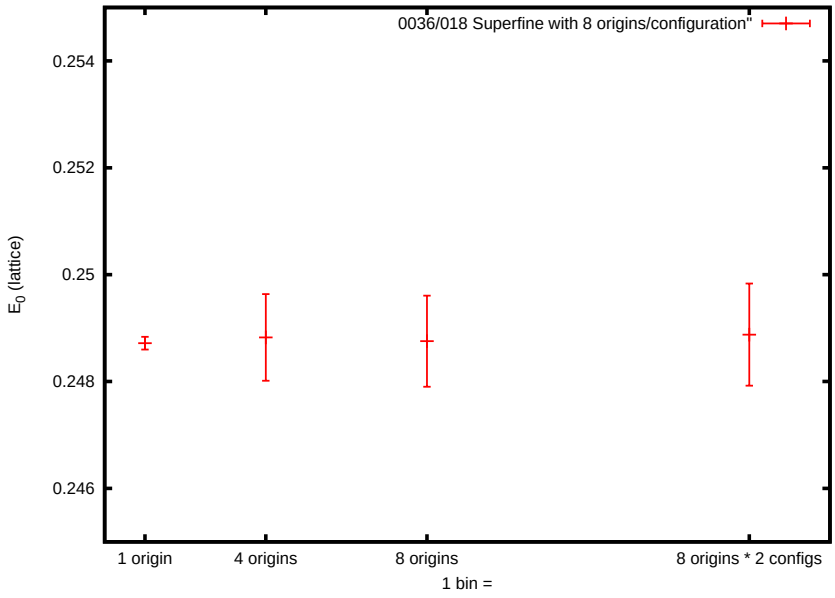

Figure 4.6: Testing for autocorrelations: plot of fit results for E_0 against bin size for the "superfine" 0036/018 ensemble.

4.2 Calculation of mean Landau links

In order to tadpole improve the gauge fields in the NRQCD action, it is necessary to determine the mean Landau link. This has already been done for some of the ensembles used in this thesis, but not for all. The existing u_0 values were taken from [4]. I calculated the value U_{0L} for both of the very coarse ensembles, and both of the coarse ensembles (although the 010/050 has an existing value that we simply chose to update to an extra decimal place).

Taking a subset of the ensemble, we update each link by multiplying them by a gauge transformation matrix. First, we take

$$M(x) = \sum_{\mu} \left(U_{\mu}(x - \hat{\mu}) - U_{\mu}(x) \right) \tag{4.1}$$

which are made Hermitian and traceless. The process is hastened by Fourier accelerating M [47]. After every iteration, the mean trace of $MM^{\dagger}$ is calculated. The gauge transform

Ensemble	U_{0L}
0097/0484	0.821794(54)
0194/0484	0.822508(89)
010/050	0.835874(40)
005/050	0.8362

Table 4.2: Values for the mean Landau link, calculated on various ensembles. Ensembles are labelled using the values for the light and strange quark masses by taking the digits after the decimal; for example the ensembles with $au_{0P}m_{u,d} = 0.010$ and $au_{0P}m_s = 0.050$ is labelled 010/050.

matrix is then

$$G(x) = I + \alpha M(x) \tag{4.2}$$

where α is a constant parameter and I is the unit matrix.

Having updated the links by $G(x)$, we find the current value of the mean gauge link. This process is repeated until the value of the mean link and the mean trace of $MM^\dagger$ plateau, after which the final value is taken to be the mean link in Landau gauge.

The results of this calculation are tabulated in table 4.2, all of which were taken to four decimal places when implemented in the Υ simulation.

4.3 Random Wall Techniques

The Random Wall algorithm allows us to increase our usage of the available configurations without any significant increase in the processing required. The idea is to attempt to simulate not just one quark/anti-quark pair at some starting spatial point on the lattice, but rather a quark/anti-quark pair at *every* spatial point.

One could do this simply be rerunning the same configuration L^3 times, but clearly this

would be very computing intensive. Instead, we wish to place all of the quark/anti-quark pairs on the lattice at once, so that they can all be processed as a single computation. This would be as fast as the original single job, and a viable way of proceeding, but there would be a lot of noise due to the ambiguity of which quark is bound to which anti-quark to form the meson. To address this, we assign each spatial point a random phase $\theta \in \mathbb{R}$ in the complex plane. This phase multiplies the smearing function used in the creation operator for a quark by $\eta = e^{i\theta}$, and thus logically the complex conjugate $\eta^\dagger = e^{-i\theta}$ of such a phase would be applied to the operator for an anti-quark. Since we use $G_{\overline{q}} = G_q^\dagger$, the conjugation of the phase occurs implicitly. Making use of the property of random unit complex numbers, η:

$$\langle \eta_a \eta_b \rangle = \delta_{ab} \tag{4.3}$$

a quark and anti-quark that are created on the same lattice site have complimentary phases, and the pair will be interpreted as a meson, whereas combinations of quark creation operator with an anti-quark operator from differing start sites will create noise that tends to cancel in the average.

Had one calculated every meson-origin separately, the results would be highly correlated, and we would bin them together to make a single representative correlator to use in our Monte Carlo average. Such a correlator would be a more accurate representation of the correlator for that configuration, leading to smaller errors in the final average. With the exception of the residual noise, the random wall has effectively given us precisely this. An example of an ensemble average correlator is depicted in figure 4.7.

Tests of the random wall showed a large improvement in the determination of the ground state energies relative to a simple point-to-point simulation, although little was gained for higher energy levels (see figures 4.9 and 4.10). Given the improved ground state, and the low cost of this procedure, its use in Υ spectroscopy can help us to reduce the statistical errors on our simulations. In chapter 5, these error improvements will allow us to examine the NRQCD dispersion relation.

Smearing functions are typically used to improve simulations by helping to pick out

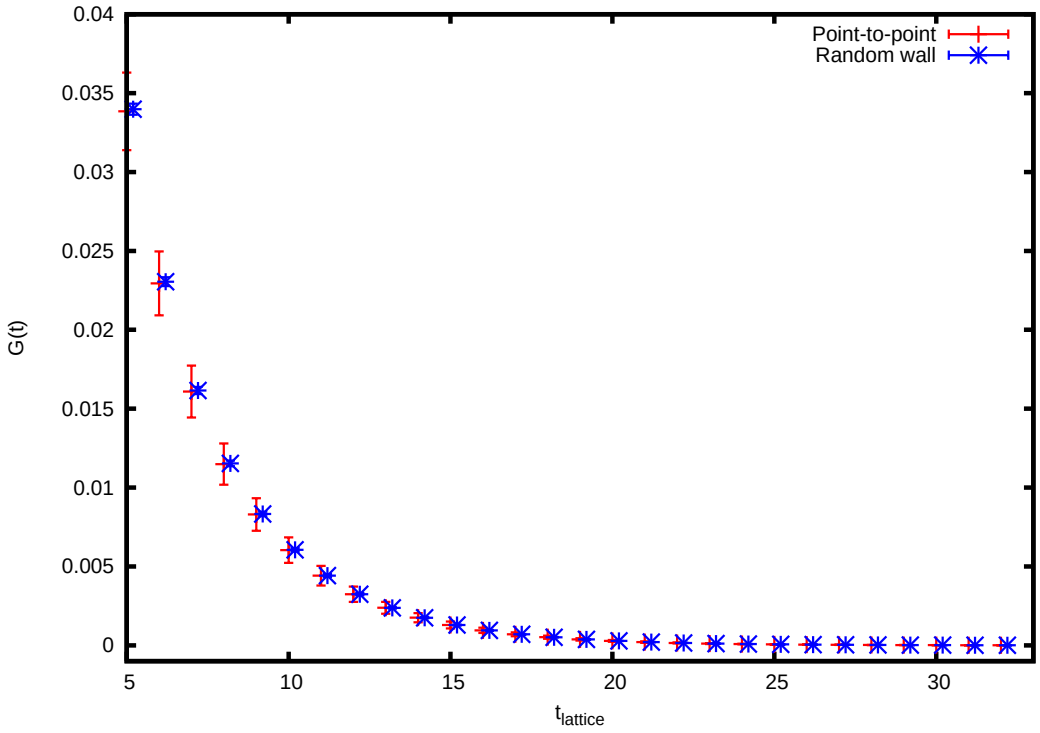

Figure 4.7: The mean correlators from the "coarse" 010/050 using a point-to-point source (dashes), and using a random wall (bursts). The bursts have been slightly off-set to the right and the x-range has been truncated at the origin for clarity.

particular radial quantum numbers for a given meson propagator. Smearing functions, $\phi(x)$, spread the quark out over the spatial extent of the lattice, and are chosen such that they have reasonable cross-over with the functional form of the Υ states that we are most interested in.

In order to improve the determination of higher energy states, we investigated combining such smearing functions with the random wall technique using a quark creation operator of the form:

$$G(\vec{x}, 0) = \sum_{\vec{y}} \phi(|\vec{x} - \vec{y}|) R(\vec{y}) \tag{4.4}$$

where $R(\vec{y})$ is the random phase from the random wall associated with co-ordinate $\vec{y}$.

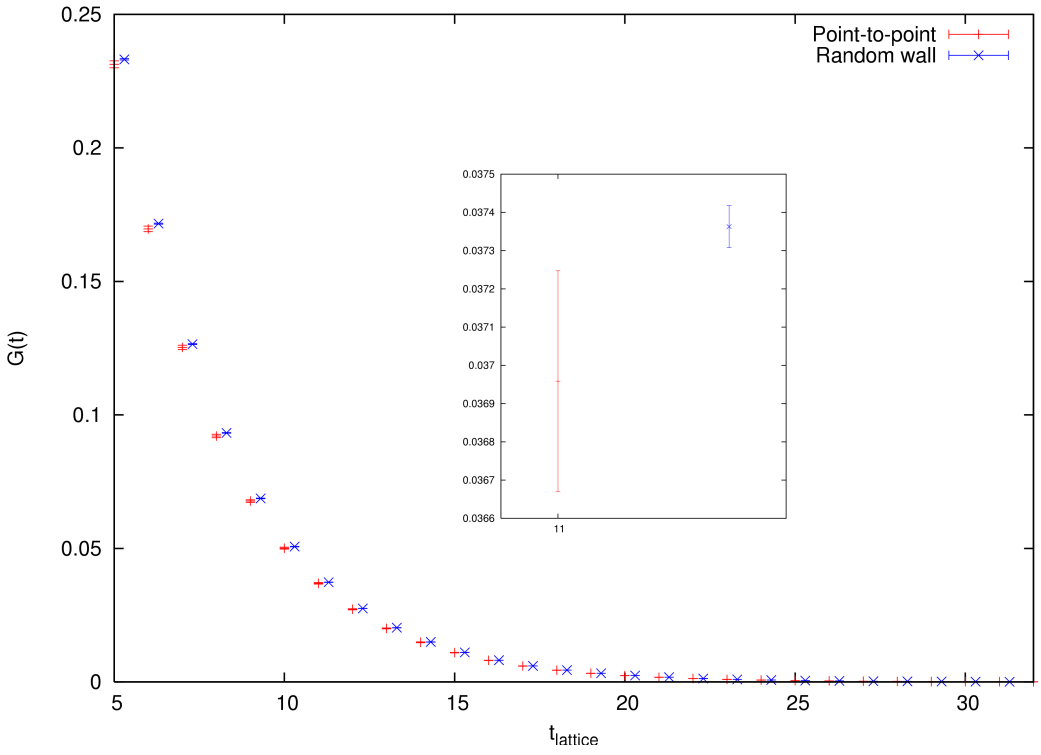

Figure 4.8: The mean correlators from the "coarse" 010/050 using a point-to-point source (dashes), and using a random wall (crosses). The crosses have been slightly off-set to the right and the x-range has been truncated at the origin for clarity. The insert shows a close up of a typical pair of points (in this case, at t=11) The error on the wall source is favourable, but not by as much as in figure 4.7.

Figure 4.8 shows a comparison of the correlator for a normal point-to-point smeared meson, and for the same meson constructed using the same smearing function applied to the random wall. As in figure 4.7, there is an improvement in the error associated with the correlator, however the effect is not as marked as before - indeed figure 4.8 requires an insert at a smaller scale for the error difference to clearly visible.

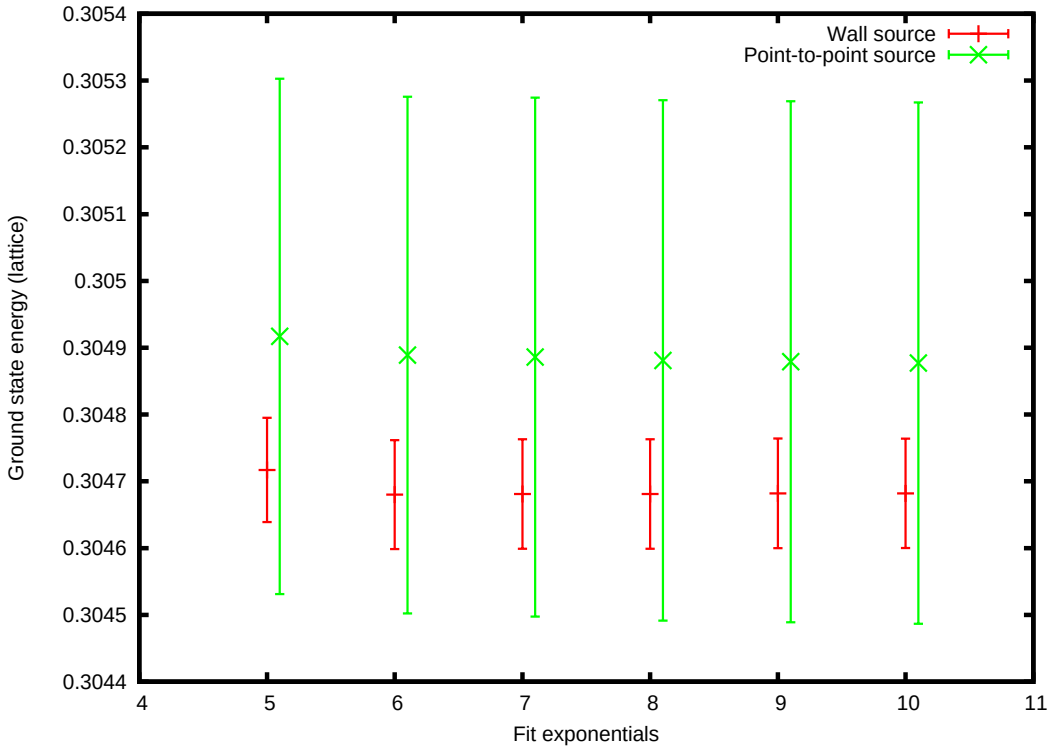

Figure 4.9: Comparison of the ground state energy of the Υ from a 2×2 matrix fit using random wall and point-to-point sources.

4.4 Bare Quark Mass and the Kinetic mass

The bare mass of the b quark must be determined as it is a free parameter of the theory. This is done by asserting that the mass of the Υ as measured in the simulation must match that of experiment, and so we tune aM_b until this is so.

Energies determined in the simulation are shifted relative to a physical zero as the

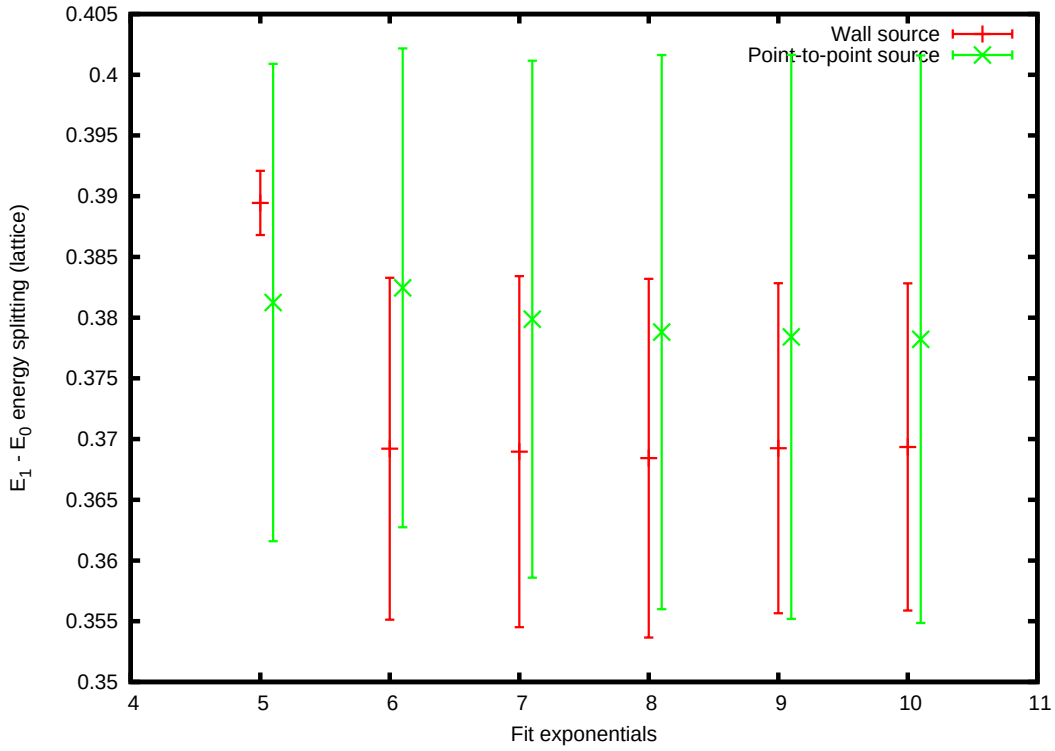

Figure 4.10: Comparison of the $E_1 - E_0$ energy splitting of the Υ from a 2×2 matrix fit using wall and point-to-point sources.

energy scale M has been removed from the simulation, and so one cannot use the normal relativistic energy/mass relation

$$E(p) = \sqrt{(M^2 + p^2)}.$$

However, since such a shift would be consistent, we can determine M if we also make two measurements - one at rest and one at a higher momentum:

$$E(p) - E(0) = \sqrt{(M^2 + p^2)} - M.$$

Then the kinetic mass is given by:

$$M = \frac{p^2 - \Delta E^2}{2\Delta E},$$

where

$$\Delta E = E(p) - E(0).$$

Values of aM_b were input in to the simulation, and used to generate ${}^3S_1$ Υ correlators at momenta of (0,0,0) and (2,0,0) (including all permutations) on each of the lattices used. It was believed [48] that the kinetic mass had little dependence on p, and so the value used to determine the kinetic mass of 2 was chosen as it represents a momentum of 1 applied to each quark in the random wall. Giving a momentum $\mathbf{p}$ to a random wall meson is done by multiplying the random phase by $\exp(i\pi\mathbf{x}\cdot\mathbf{p}/L)$ for the quark and $\exp(-i\pi\mathbf{x}\cdot\mathbf{p}/L)$ for the anti-quark (where the negative sign ensures the anti-quark has a positive momentum after complex-conjugation), i.e. half of the momentum is applied to each constituent particle.

The two momenta were concurrently fitted using the Bayesian method described previously, and converted to physical units using a value for the lattice spacing calculated in [4]. Fitting concurrently means that we fit the correlated difference ΔE directly, which is more accurately determined than fitting the energies separately, and then taking the difference. Results are tabulated in table 4.3.

		Υ	Kinetic mass		η_b	Kinetic mass	
Ensemble	aM_b	$E_0\|_{p^2=4} - E_0\|_{p^2=0}$	Lattice	GeV	$E_0\|_{p^2=4} - E_0\|_{p^2=0}$	Lattice	GeV
0097/0484	3.40	0.042548(82)	7.228(14)	9.56(15)	0.041781(24)	7.361(4)	9.74(15)
0194/0484	3.40	0.042576(69)	7.223(12)	9.49(15)	0.041825(34)	7.353(6)	9.66(15)
005/050	2.80	0.022869(38)	5.983(10)	9.73(15)	0.022676(21)	6.034(6)	9.82(15)
010/050	2.80	0.032938(32)	5.976(6)	9.62(15)	0.032597(19))	6.039(4)	9.72(15)
0062/031	1.95	0.023455(66)	4.282(12)	9.74(15)	0.023298(10)	4.311(2)	9.80(15)
0036/018	1.34	0.011217(65)	3.050(18)	9.93(17)	0.01151(22)	2.972(57)	9.68(24)

Table 4.3: Kinetic masses from tuning bare quark mass aM_b. Calculated using $r_1 = 0.321(5)$fm from [4].

4.5 r_1 scale calculation

Quantities determined on the lattice are dimensionless, containing factors of the lattice spacing which have dimensions of inverse energy. The lattice and physical values are related as:

$$E_{lattice} = aE_{physical},$$

$$A_{lattice} = a^3 A_{physical},$$

where E is an energy and A an amplitude. Therefore, to make a dimensionally meaningful determination, knowledge of a^{-1} is essential.

The lattice spacing itself is implicitly determined on the lattice by the choice of parameters that went in to its production, but is not explicitly known. To obviate this issue, one makes use of the quantity known as r_1, which is defined as the value of the heavy quark potential at which $r^2F(r) = 1.0$ (where F is the gradient of the potential) [49], and is not physically measured. Instead, we determine a^{-1} for a set of lattices and use the relevant r_1/a for each lattice to determine r_1, which can then be used to determine a^{-1} for subsequent lattices. Since a^{-1} will factor into conversion from lattice to physical results, some times at high powers, the accuracy in r_1 can be paramount to the preservation of accuracy in the final result.

With this in mind, we require the values of r_1/a for each lattice being used in this work. Thankfully, the MILC collaboration[45], whose lattices we are using, have already calculated this value for their ensembles. They do this by placing a static, infinitely heavy quark and anti-quark on the lattice, and measuring the potential between them by calculating loops between the quark/anti-quark pairs extending in the time direction. In fact, the lattices are gauge fixed to Coulomb gauge, and only products of temporal links need be multiplied [50]. The potential is then extracted from the ratio of such "loops" with temporal distances T and $T-1$ (in the case of [50], $T=5$). The potential is computed at all spatial separations, with related separations combined. This can then be fitted to the form

$$V(r) = C - \alpha/r + \sigma r + \lambda(V_{free}(r) - 1/r) \tag{4.5}$$

where the last term is only used for small values of r, and is to correct for lattice artefacts. Having fitted the static quark potential, all that remains is to calculate the value of r for which $r^2F(r) = 1.0$.

We measure the inverse lattice spacing on an assortment of lattices by comparing the 2S-1S energy splitting as measured on the lattices with that of experiment. The 2S-1S splitting is expected to have the lowest discretisation errors of the possible splittings available [4]. Systematic errors arise from three major sources: relativistic corrections, radiative correction and discretisation. In the case of relativistic errors, one must consider that we are dealing not with expectation values, but with the *difference* between expectation values - the $1S$ and $2S$ are similar enough that that the error in this difference will be smaller than expected. Discretisation errors are also expected to favour the $2S-1S$ splitting due to their similarity.

We use a 3x3 Bayesian matrix fit to obtain our results, concurrently fitting three different configurations of valence quarks at source and sink. This is achieved by applying *smearing functions* to each valence b quark. We used, in addition to the δ local operator, a hydrogenic function, applied to only one quark in the meson, to approximate the S wave state; and the convolution of the same hydrogenic function by applying it to both valence

Lattice	Very coarse		Coarse		Fine	Super Fine
	0097/0484	0194/0484	005/050	010/050	0062/031	0036/018
a_0	0.82	0.83	1.0	1.0	1.41	2.0

Table 4.4: Smearing radii for each ensemble used in out $b\overline{b}$ simulations. a_0 is changed with approximate lattice spacing.

quarks:

$$\begin{aligned}
\phi^q_{local}(x) &= \delta(x) &,\quad \phi^{\bar{q}}_{local}(x) &= \delta(x), \\
\phi^q_{1S}(x) &= (2a_0 - |x|)\, e^{(-0.5|x|/a_0)} &,\quad \phi^{\bar{q}}_{1S}(x) &= \delta(x), \\
\phi^q_{2S}(x) &= (2a_0 - |x|)\, e^{(-0.5|x|/a_0)} &,\quad \phi^{\bar{q}}_{2S}(x) &= (2a_0 - |x|)\, e^{(-0.5|x|/a_0)}.
\end{aligned}$$

where a_0 is a characteristic length for the smearing in lattice units, listed in table 4.4, and $|x|$ is the shortest distance from $\vec{x}$ to the origin, taking account of periodic boundary conditions. The S-wave shown above is intended to pick out the excited $\Upsilon(2S)$ state, not the $1S$ state - a local source with the random wall picks out the ground state so well that the $2S$ is the limiting factor, and the smearing functions are chosen with this in mind.

These smearings are then combined with the random wall (Section 4.3) and used as our (anti-)quark creation operator.

4.5.1 r_1 Results

Using the bare quark masses for each configuration, as calculated in Subsection 4.4, each ensemble was run using the local, 1S and 2S smearing functions. 3×3 Bayesian fits were made to these correlators. The results of these fits are tabulated in Tables 4.5 and 4.6, along with Q, which measures the quality of the fit and is related to the value of χ^2.

$$Q \equiv \frac{\int_x^\infty t^{a-1}e^{-t}dt}{\int_0^\infty t^{a-1}e^{-t}dt}, \tag{4.6}$$

where a is equal to half the number of degrees of freedom, and x = $\chi^2/2$.

Ensemble	E_0	$E_1 - E_0$	$E_2 - E_0$	Q
very coarse 0097/0484	0.287749(84)	0.4244(33)	0.596(74)	0.33
very coarse 0194/0484	0.288143(78)	0.4309(32)	0.707(32)	0.17
coarse 005/050	0.2933(26)	0.3439(8)	0.556(16)	0.88
coarse 010/050	0.292611(60)	0.3462(38)	0.549(42)	0.98
fine 0062/031	0.266175(49)	0.2381(37)	0.406(24)	0.3
superfine 0036/018	0.248500(33)	0.1679(14)	0.296(16)	0.36

Table 4.5: Fitted energies for the Υ from 3×3 Bayesian fits taken at $N_{exp} = 10$.

Ensemble	E_0	$E_1 - E_0$	$E_2 - E_0$	Q
very coarse 0097/0484	0.250892(69)	0.4453(38)	0.608(74)	0.65
very coarse 0194/0484	0.251723(66)	0.4522(37)	0.768(51)	0.32
coarse 005/050	0.261613(23)	0.3611(21)	0.541(57)	0.97
coarse 010/050	0.260696(50)	0.364(33)	0.539(77)	0.90
fine 0062/031	0.240843(35)	0.2534(38)	0.413(31)	0.22
superfine 0036/018	0.229198(30)	0.1781(16)	0.281(35)	0.45

Table 4.6: Fitted energies for the η_b from 3×3 Bayesian fits taken at $N_{exp} = 10$.

Q is the probability that the correct model could produce a χ^2 as poor as that of our fit. The closer Q is to one, the more likely it is that fit describes the data well. A fit is considered "good" if Q is greater than about 0.1, lower values should be treated with scepticism, and very small values are characteristic of a bad fit [51].

Table 4.7 shows the priors used in the Bayesian fits. All of the smearings are normalised, and so we would expect a reasonable amplitude to be on the range $[-1 : 1]$. The amplitude priors A_i are all set to 0.1 ± 1[1], which makes them small (which would be

[1]We could have used 0.0 ± 1, which would have given use the range $[-1 : 1]$ exactly, but for programming reasons, it was easier to use non-zero values. Since the priors are only loose constraints, this difference is not important.

Ensemble	E_0	$E_{i+1} - E_i$	$\ln(E_0)$	σ_0^2	$\ln(E_{i-1} - E_i)$	σ_i^2	A_i	σ_A^2
very coarse 0097/0484	0.25	0.38	-1.4	0.41	-0.97	0.69	0.1	1
very coarse 0194/0484	0.25	0.38	-1.4	0.41	-0.97	0.69	0.1	1
coarse 005/050 η_b	0.25	0.30	-1.4	0.41	-1.2	0.69	0.1	1
coarse 005/050 Υ	0.30	0.37	-1.2	0.41	-1.0	0.69	0.1	1
coarse 010/050	0.25	0.30	-1.4	0.41	-1.2	0.69	0.1	1
fine 0062/031	0.25	0.25	-1.4	0.41	-1.4	0.69	0.1	1
superfine 0036/018	0.25	0.17	-1.4	0.41	-1.8	0.69	0.1	1

Table 4.7: Fitting priors for 3×3 Bayesian fits to both the Υ and η_b.

expected for higher values of the i index), but constrained sufficiently weakly that any reasonable amplitude would be accepted by the fit.

The Υ spectrum energy splittings are relatively regularly spaced, so the same prior is used for all energy splittings $E_{i+1} - E_i$ on the same ensemble, where $i \geq 1$. The values are simply rough guesses to the value of a given parameter, and can be estimated using, for example, the experimental value of the splitting converted in to lattice units using an approximate lattice spacing (since MILC have an approximate idea of how large a lattice is when they create an ensemble). We take all of the $E_{i+1} - E_i$ priors to be approximately 500 MeV[2]. E_0 has its own prior, which can be estimated from an effective mass plot such as figure 3.3. The widths are chosen to be wide enough not to overly constrain the fit to these guessed values. In practice, we fit the logarithm of the energy splittings, which ensures that $E_0 > 0$, $E_{i+1} > E_i$.

These lattice results were then compared to experiment to extract the inverse lattice spacing per ensemble. These spacings were then compared to r_1/a values, tabulated in Table 4.8. The conversion factor from energy to distance is 197.327 MeV fm.

[2]The 005/050 Υ used slightly altered priors, and in this case the $E_{i+1} - E_i$ priors were taken to around 600 MeV.

Lattice	r_1/a	a^{-1}	r_1
0097/0484	2.152(5)	1.33(1)	0.319(3)
0194/0484	2.138(4)	1.31(1)	0.322(3)
005/050	2.647(3)	1.64(1)	0.318(2)
010/050	2.618(3)	1.63(2)	0.317(4)
0062/031	3.699(3)	2.36(4)	0.309(5)
0036/018	5.296(7)	3.35(3)	0.312(3)

Table 4.8: r_1/a from [3]

These results then need to be extrapolated to the continuum limit. This was done in [52] by fitting the r_1^Υ from each ensemble (i.e. $(r_1/a)_i a_i^\Upsilon$ where the i subscript denotes ensemble) to an equation for the effective r_1:

$$r_1^\Upsilon(a, \delta m_l^{sea}, \delta m_s^{sea}) = r_1 \left(1 + c_{sea}^\Upsilon \frac{2\delta m_l^{sea} + \delta m_s^{sea}}{m_s}\right) \left(1 + \sum_{j=1}^{4} c_j^\Upsilon (a/r_1)^{2j}\right),$$

by means of a Bayesian fit (where r_1, c_{sea}^Υ and c_j^Υ are fit parameters). The δm^{sea} terms are the differences between the simulated s sea-quark and the physically correct value, and between the simulation and correct u/d light sea-quark masses, which are taken to be degenerate. By "physically correct", we mean the bare mass that would give the correct mass for π, K and η_s mesons. These bare masses (in HISQ formalism) and the means by which one converts them in to ASQTAD quarks can be found in [52]. The second bracketed term corrects for discretisation errors. This gave a result of:

$$r_1 = 0.3091(44)\text{fm},$$

with a χ^2 of 0.2.

Ultimately we [52] combined the data from my Υ simulations (plotted in green in figure 4.11) with data produced by other members of the HPQCD collaboration; specifically $m_{D_s} - m_{\eta_c}/2$ and f_{η_s} which are outlined below.

The η_s is a fictitious meson composed of an s quark and anti-quark, which in reality

would mix with $u\overline{u}$ and $d\overline{d}$ states, known as the η and $\eta\prime$ mesons: $\eta = \frac{u\overline{u}+d\overline{d}-2s\overline{s}}{\sqrt{6}}$, $\eta\prime = \frac{u\overline{u}+d\overline{d}+s\overline{s}}{\sqrt{3}}$. The η_s is simpler to study on the lattice, and has the advantage of being only weakly dependent on the light sea quark masses. In the continuum, its mass and decay constants may be determined from pion and kaon data (both simulation and experimental) using chiral perturbation theory. Fitting of the η_s followed a similar procedure as that used with the Υ system. This data can be found on figure 4.11 in blue.

Using bare quark masses that give the correct η_s and η_c masses, the $m_{D_s} - m_{\eta_c}/2$ gives a better signal to noise ratio than in the Υ system because both mesons are ground-states, however it is complicated by the involvement of two quark masses. This determination was made possible by the HISQ action for simulating charm quarks [11]. In this simulation, the collaboration simulated D_s, η_c and η_s at a number of s and c quark masses, and in each case converted to physical units via the $m_{D_s} - m_{\eta_c}/2$ splitting. Fitting proceeds using a multi-exponential form, including oscillating states for D_s. It is then possible to interpolate a plot of m_{η_c} against m_{η_s} to experiment[3]. The lattice spacing is then defined as the ratio of the lattice simulation of $m_{D_s} - m_{\eta_c}/2$ to the experimental result, at simulation valence masses that reproduce η_s and η_c consistent with experiment. Two lattice spacings were used,appearing in red on figure 4.11, and were fitted in the same manner used for both the Υ and η_s methods.

To obtain the most accurate results, all three of these methods were fitted concurrently in [52], with the requirement that each fit must agree on the value of the r_1 parameter, leading to a final result of

$$r_1 = 0.3133(23)(3)\text{fm},$$

where the second error is from finite-volume corrections.

Figure 4.11 demonstrates the low a^2 dependence of the Υ splitting method, compared to the other methods. In light of this, the group's previous prediction of 0.321(5) from [4] - which differs from this new determination by about 1.5σ - is not unexpected, as without

[3]More precisely, as described in [52], interpolated to a shifted experimental value, to account for phenomena not simulated on the lattice, such as electromagnetism.

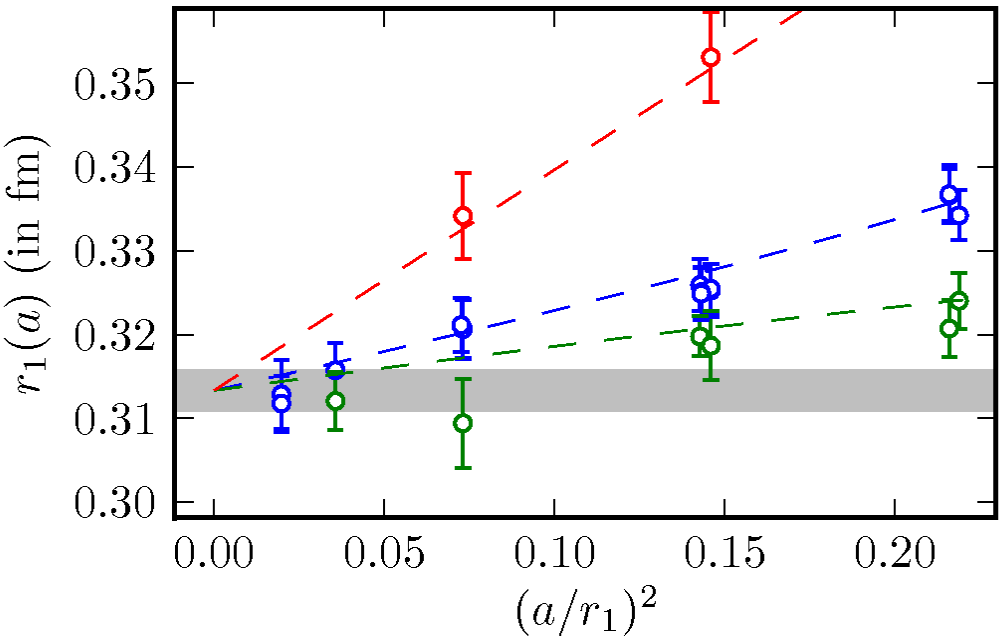

Figure 4.11: r_1 as a function of lattice spacing. Green points indicate determinations from the Υ spectroscopy presented in this thesis. The red (top line) and blue (middle line) points are from $m_{D_s} - m_{\eta_c}/2$ and f_{η_s} respectively.

the finer lattices that are now available, the flatness of the data is consistent with a higher value of r_1.

4.5.2 The Υ S-wave Spectrum

By defining the $\Upsilon(1S)$ state to match experiment, and using this new r_1 value, we can convert our S-wave results to physical units, and make comparison with experiment where appropriate. We have converted the coarse 005/050 ensemble due to the higher statistics we have for this ensemble (2083 configurations), and also our finest simulations: the 0063/031 fine and the 0036/018 superfine, plotted in figure 4.12 as dashes, crosses and bursts respectively. We must sacrifice the $\Upsilon(1S)$ state as an example of a lattice determination because this state is used to define where the zero of energy is, however the $\Upsilon(2S)$ state is not defined to match experiment because the scale determination, while including the $(2S-1S)$ splitting, also includes other physics. For comparison, figure 4.12 also includes the experimental values for the Υ states, and the $\eta_b(1S)$ state. The higher η_b states have not yet been found experimentally. The plot shows good agreement between the lattice and experimental values of the η_b. The $\Upsilon(3S)$ 005/050 determination, benefiting from improved statistics over the other ensembles, also shows good agreement with the accepted physical value.

4.6 Determination of α_s

Lattice techniques can be used to determine the value of the strong coupling α_s. By computing non-perturbative values of short-range quantities which would take the form

$$Y = \sum_{n=1}^{\infty} c_n \alpha_V^n(d/a) \tag{4.7}$$

in perturbation theory (where c_n and d are dimensionless constants independent of lattice spacing, and $\alpha_V(d/a)$ is the running QCD coupling constant with 3 light flavours in the V

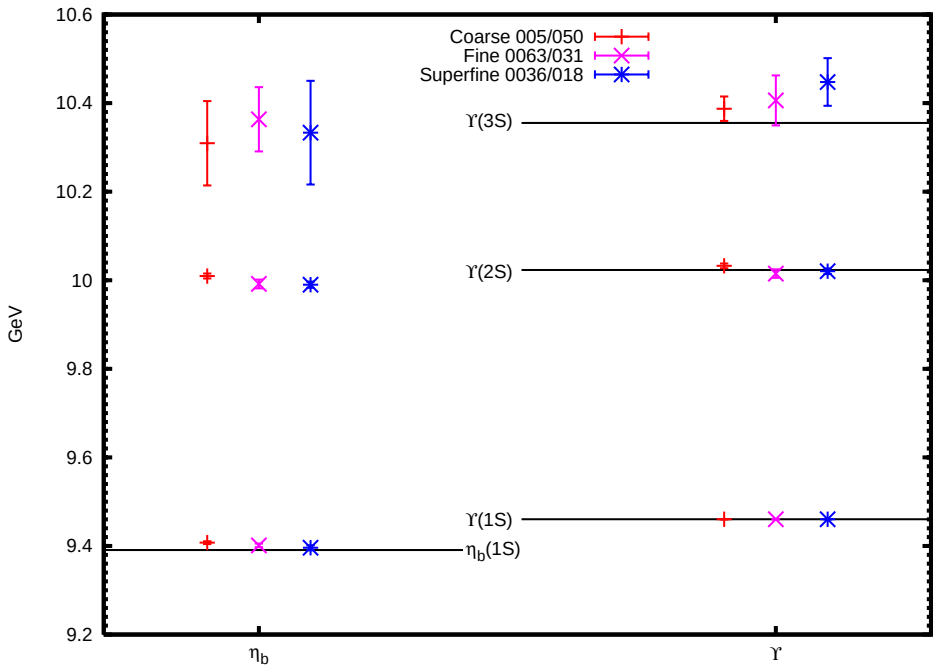

Figure 4.12: The Υ and η_b spectra in physical units for the 005/050 coarse, 0063/031 fine and 0036/018 superfine MILC ensembles. The horizontal lines represent experimental values taken from the Particle Data Group [1].

scheme, in which α_V is defined from the heavy-quark potential [53, 54]), we can, assuming one knows the values of c_n to the desired order, extract $\alpha_V(d/a)$ by choosing it such that this perturbative formula and the calculated non-perturbative value match [55]. Given the values of d and a, and the masses of the c and b quarks, the value of $\alpha_V(d/a)$ can be re-expressed in the conventional $\alpha_{\overline{MS}}(M_Z, n_f = 5)$. This is done by converting to the $\overline{MS}$ scheme (using equation 4.8, then using perturbation theory to first add in the c and b vacuum polarisation [56] and then to evolve to the Z meson mass.

$$\alpha_{\overline{MS}}^{(n_f)}(e^{5/6}q) = \alpha_V^{(n_f)}(q) \times \left(1 + \frac{2\alpha_V}{\pi} + [0.1411 n_f - 0.7344]\alpha_V^2\right) \tag{4.8}$$

Simple short-distance quantities are Wilson loop operators:

$$W_{m,n} \equiv \frac{1}{3}\left\langle 0|\mathrm{ReTr}Pe^{-ig\oint_{m,n} A\cdot dx}|0\right\rangle. \tag{4.9}$$

P represents path-ordering, A is the QCD vector potential; the loop is over a closed rectangular path of size $ma \times na$. The coefficients c_n have been calculated up to $n = 3$ for six planar rectangles and two non-planar loops (a two by one "bent" rectangle, and a corner-cube) [see, for example, [5, 57]] using Feynman diagrams.

The expansion of such a loop is dominated by its self-energy contribution, which is proportional to the loop size; as the loop becomes large, this contribution exponentiates. The perturbation series is more convergent therefore for the logarithm of the loop, which are then further reduced by tadpole improving them - dividing them by $u_0^{2(m+n)}$. The factor u_0 is defined as the fourth root of the 1×1 Wilson loop.

Lattice simulations were done using MILC ensembles described in table 4.1. Wilson loops are calculated simply as products of the tadpole improved lattice gluon fields $U_\mu(x)$, as seen earlier in this thesis, and are tabulated in tables 4.9 and 4.10. This gives us a value for eight different loops (W_i) over 5 different lattice spacings. To $\mathcal{O}(\alpha_V^3)$,

$$-\ln(W_i^{lattice}) = w_0\alpha_V \times [1 + r_1\alpha_V + r_2\alpha_V^2], \tag{4.10}$$

Loop	0097/0484		0194/0484		005/050		010/050	
1,1	0.548012	5.1e-05	0.549471	5.3e-05	0.567069	1.6e-05	0.566911	4.9e-05
1,2	0.298624	6.8e-05	0.300307	7.0e-05	0.323163	2.1e-05	0.322943	6.6e-05
1,3	0.165063	6.7e-05	0.166527	7.0e-05	0.187281	2.4e-05	0.187026	6.8e-05
1,4	0.091701	6.3e-05	0.092797	6.3e-05	0.109122	2.7e-05	0.108887	6.4e-05
2,2	0.101572	7.3e-05	0.102638	7.6e-05	0.121542	1.9e-05	0.121356	7.4e-05
2,3	0.038333	5.4e-05	0.039007	5.4e-05	0.050751	1.5e-05	0.050547	5.7e-05
BR	0.3567634	6.8e-05	0.358571	7.0e-05	0.381148	2.5e-05	0.380915	6.9e-05
CC	0.3063154	7.8e-05	0.308143	7.9e-05	0.332184	2.7e-05	0.331941	7.5e-05

Table 4.9: Tadpole-improved Wilson loops on the very coarse and coarse MILC ensembles. These loops were calculated by the author.

Loop	0082/082		0062/031		0036/018	
1,1	0.534101	1.7e-05	0.594843	6.7e-06	0.6214623	2.5e-06
1,2	0.280720	2.2e-05	0.359761	9.4e-06	0.3957172	4.2e-06
1,3	0.149263	2.1e-05	0.221624	1.0e-05	0.2567700	4.6e-06
1,4	0.079710	1.9e-05	0.137271	1.0e-05	0.1674864	4.7e-06
2,2	0.087438	2.3e-05	0.153433	1.2e-05	0.1869588	5.1e-06
2,3	0.030150	1.6e-05	0.072261	1.0e-05	0.0968520	4.7e-06
BR	0.338982	2.2e-05	0.417002	8.6e-06	0.4517979	3.8e-06
CC	0.287376	2.5e-05	0.390239	9.8e-06	0.4072097	4.5e-06

Table 4.10: Tadpole-improved Wilson loops on the super coarse, fine and superfine MILC ensembles. These loops were not calculated by the author. The 0082/082 ensemble in column 1 is the MILC ensemble with $\beta = 6.458$, $r_1/a = 1.802(10)$, $am_l = 0.0082$, $am_s = 0.082$ and dimension $16^3 \times 48$. The other ensembles are those seen previously in table 4.1.

where r_i is divided in to gluonic and fermionic parts, the coefficients for which are tabulated in 4.11:

$$r_i = r_{i,g} + r^{(1)}_{i,f} N_f + r^{(2)}_{i,f} N_f^2. \tag{4.11}$$

Loop	aq^*	w_0	$r_{1,g}$	$r^{(1)}_{1,f}$	$r_{2,g}$	$r^{(1)}_{2,f}$	$r^{(2)}_{2,f}$
1×1	3.325	3.0683955(6)	-0.7779(2)	-0.096774(12)	-0.729(36)	0.7744(52)	0.010186(4)
1×2	2.998	5.5511998(242)	-0.6213(4)	-0.079059(19)	-0.410(37)	0.6866(52)	0.007027(4)
1×3	2.934	7.8765622(481)	-0.5311(8)	-0.070857(13)	-0.260(41)	0.6484(52)	0.005850(5)
1×4	2.895	10.1715778(773)	-0.4892(8)	-0.065937(12)	-0.247(51)	0.6285(52)	0.005201(2)
2×2	2.582	9.1996965(641)	-0.4920(10)	-0.066753(16)	-0.005(44)	0.6020(53)	0.005206(7)
2×3	2.481	12.3428213 (1129)	-0.4169(13)	-0.060892(17)	0.258(54)	0.5631(54)	0.004581(2)
BR	3.221	4.8342543(125)	-0.5693(2)	-0.095123(8)	-0.399(36)	0.7018(52)	0.009845(2)
CC	3.047	5.2975794(169)	-0.5174(3)	-0.092238(9)	-0.264(36)	0.6775(52)	0.009886(2)

Table 4.11: The Lepage-Mackenzie scale and coefficients for the two-loop perturbative expansion of α_V for various Wilson loops[5].

From this, we can iteratively extract α_V for each loop / lattice-spacing combination (plotted in figure 4.13), and convert to $\alpha_{\overline{MS}}(n_f = 3)$ using equation 4.8, the results of which are plotted in figure 4.14.

A more sophisticated version of this analysis was performed in [58], which utilised the loops calculated here in addition to loops from other lattice spacings that were calculated by other members of the collaboration. Additionally, the improved version of the analysis takes in to account some higher order coefficients beyond $n = 3$. The result for $\alpha_V(7.5\text{GeV}, n_f = 3)$ from this analysis is plotted on figure 4.13 for comparison.

4.7 Input in to B_c and B_s spectroscopy

The b-quark simulations resulting from Υ spectroscopy can be put to use in studying the B_s and B_c mesons - the bound state of $b\overline{s}$ and $b\overline{c}$, respectively. Eric B. Gregory [61, 62] performed this calculation, making use of the b-propagators calculated for the previous sections by the author of this thesis.

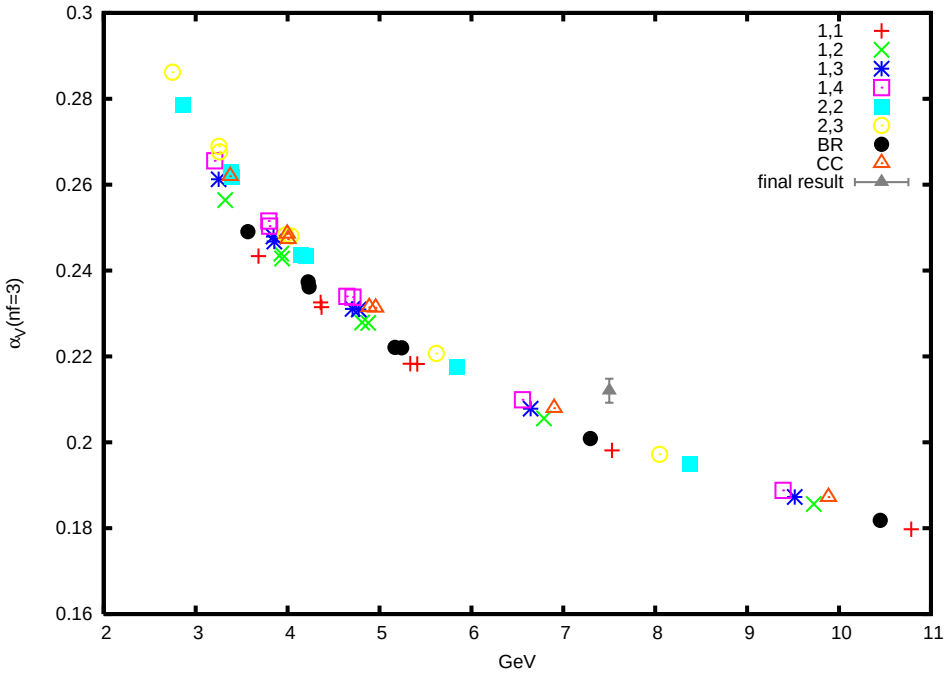

Figure 4.13: α_V as a function of energy, compared to the final result for $\alpha_V(7.5\text{GeV}, n_f = 3)$ determined in [58]

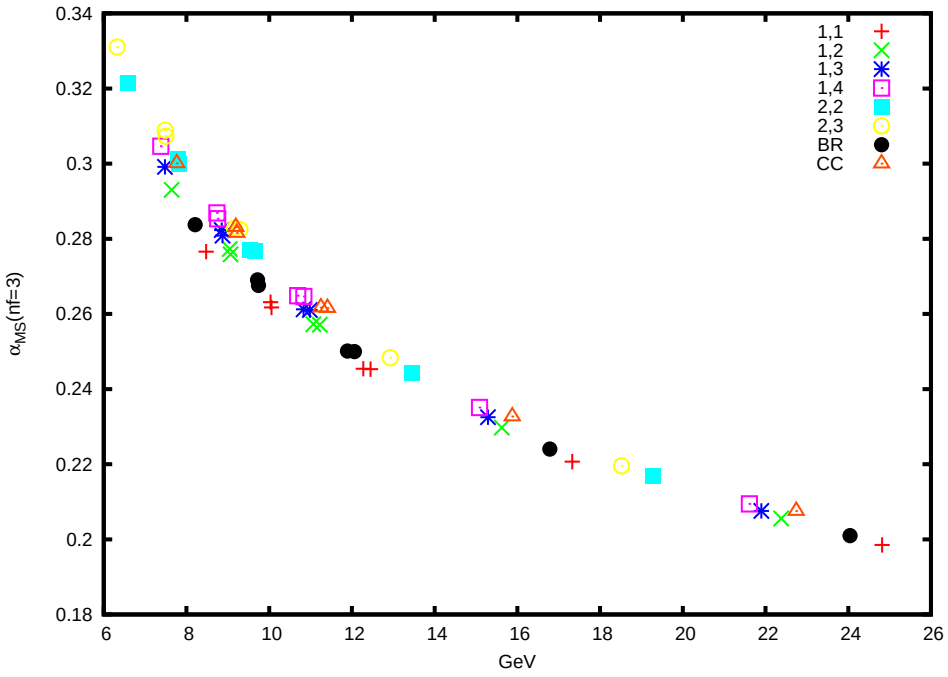

Figure 4.14: α as a function of energy, as in figure 4.13, now converted to $\alpha_{\overline{MS}}$.

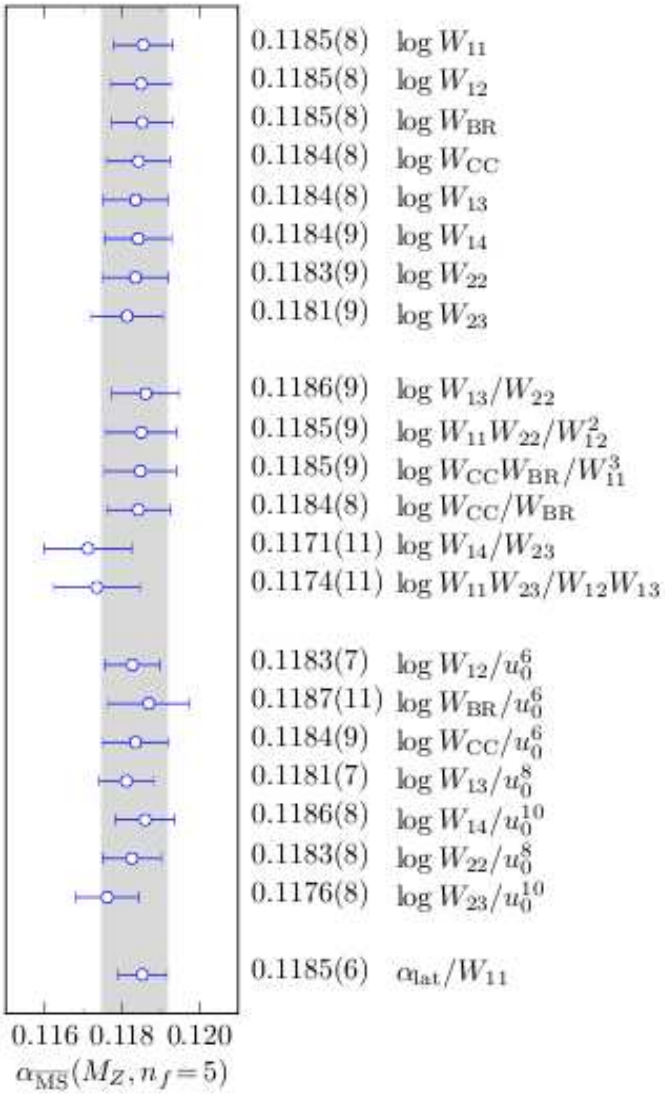

Figure 4.15: Values of $\alpha_{\overline{MS}}$ for 5-flavours at the mass of the Z-meson for each of the 22 quantities. The grey band is the final result 0.1183(8). [58]

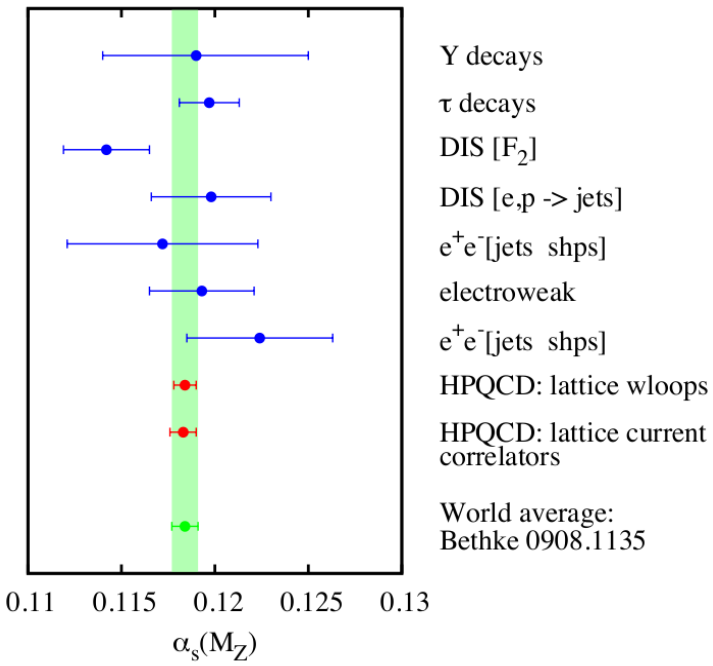

Figure 4.16: Values of $\alpha_{\overline{MS}}$ for 5-flavours at the mass of the Z-meson from a variety of different methods [59]; non-lattice results from [60].

Treatment of the c quark can pose a challenge for lattice QCD, as the mass of the quark is such that it is unclear whether it should be considered "heavy" or "light". For a $c\overline{c}$ system, the quark velocity is $\sim 0.3c^2$, which allows for a non-relativistic treatment, albeit with larger relativistic corrections. For the $b\overline{c}$, the reduced mass of the system is about 50% higher than in the charmonium case, and as such $v_c \sim 0.4c^2$ - $0.5c^2$, which makes a non-relativistic treatment even less favourable (although such an approach has be used, for example [63]). We can, instead, treat the B_c as a heavy-light system, and this is the approach that was taken in [61, 62].

Using the fine ensemble and both of the coarse and very coarse ensembles, as previously described, b-quarks propagators were created using the random wall method. Eric Gregory used the same ensembles to produce Highly-Improved Staggered Quark (HISQ) propagators for charm, strange and light quarks (taking $m_u = m_d$). The HISQ action is a fully relativistic discretisation, and is more appropriate for simulating c quarks than NRQCD. These were then paired with the b propagators along with spin matrices to form

pseudoscalar and vector mesons for B, B_s and B_c. Propagators with included smearing functions were also included to improve access to the ground state energies.

In order to combine HISQ and NRQCD propagators, it is necessary to undo the HISQ staggering transformation so that the Dirac structure of both quarks are compatible. In order to do this, one multiplies the random noise source with the staggering operator (equation 2.44)

$$\Omega(x) = \gamma_0^{x_0}\gamma_1^{x_1}\gamma_2^{x_2}\gamma_3^{x_3}. \tag{4.12}$$

Bayesian 3×3 matrix fits (on local and Gaussian smearings of different radii) were used to extract the ground state energies of interest. As in the Υ spectroscopy, the energy fit here is not the meson mass, because it contains an energy shift due to the way NRQCD is formulated. This will disappear in energy differences that contain the same NRQCD quark content, and so a similar state must also be simulated for comparison.

The first use of combining HISQ c quarks with NRQCD b quarks was to access the masses of the B_s and B_c, using three methods :

$$M_{B_s} = \left(E_{B_s} - \frac{1}{2}E_{b\overline{b}}\right)_{latt} + \frac{1}{2}M_{b\overline{b}} \tag{4.13}$$

$$M_{B_c} = \left(E_{B_c} - \frac{1}{2}(E_{b\overline{b}} + E_{c\overline{c}})\right)_{latt} + \frac{1}{2}(M_{b\overline{b}} + M_{c\overline{c}}) \tag{4.14}$$

$$M_{B_c} = (E_{B_c} - (E_{B_s} + E_{D_s} - E_{\eta_s}))_{latt} + (M_{B_s} + M_{D_s} - M_{\eta_s}) \tag{4.15}$$

where $b\overline{b}$ is the spin average of η_b and Υ, and the terms subscripted with $_{latt}$ require conversion to physical units using our previous determination of r_1. The methods appropriate for M_{B_c} compare mesons with differing electromagnetic properties, which are not simulated on the lattice, and this is corrected for. The final results give

$$M_{B_s} = 5.341(4)(10)\text{GeV} \tag{4.16}$$

(where the errors are statistical and due quark mass tunings) and

$$\begin{aligned} M_{B_c} &= 6.279(2)(1)(5)(2)\text{GeV} \\ M_{B_c} &= 6.268(4)(6)(1)(1)\text{GeV} \end{aligned} \tag{4.17}$$

where there results correspond to methods 4.14 (called the "heavy-heavy" or hh subtraction method) and 4.15 respectively, and the errors are, in order: statistical, scale conversion from r_1, systematic errors from NRQCD and electromagnetic corrections [61]. The results for the B_s and the "hh" method for B_c are pictured in figures 4.17 and 4.18 respectively, and are from [64].

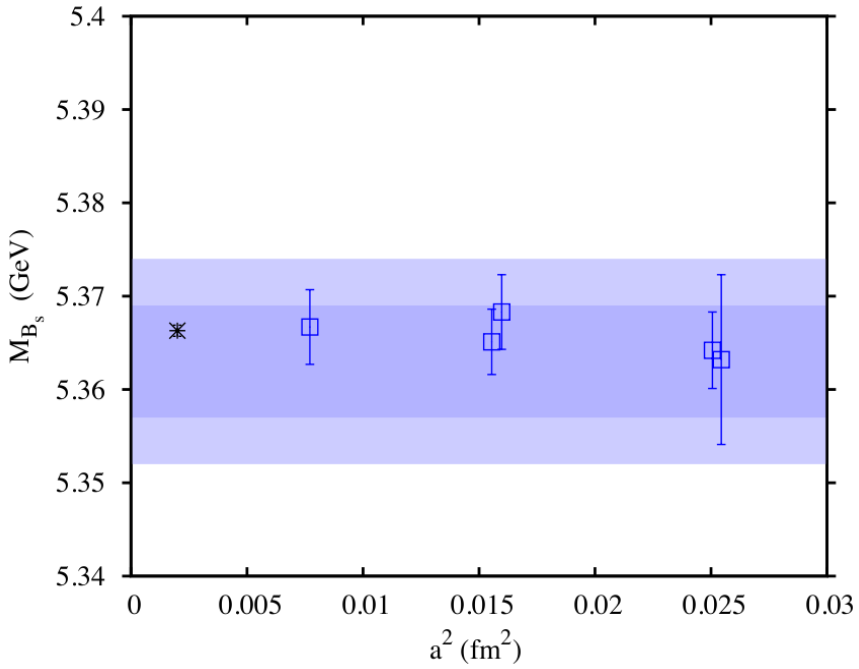

Figure 4.17: Mass of the B_s meson as a function of lattice spacing. Error bars are statistical, lattice spacing errors and tuning errors in the valence quark masses. The shaded band is the physical result allowing for sea quark mass and lattice spacing, and is described in detail in [64]. The burst symbol represents experiment. This is the first accurate lattice QCD result including the effects of u, d and s sea quarks for this quantity.

Further work was carried out[61, 62] to access the B_c^* meson state. Similarly to the $B_{s/c}$ cases above, 3×3 Bayesian fits are made using local and smeared propagators, in this fitting the $E_0(B_q^*) - E_0(B_q)$ splitting directly. There are systematic errors, such as radiative corrections to the $\sigma \cdot B$ NRQCD term, in this splitting, but these can be removed by taking the ratio

$$R = \frac{\Delta_c}{\Delta_s} = \frac{E_0(B_c^*) - E_0(B_c)}{E_0(B_s^*) - E_0(B_s)} \tag{4.18}$$

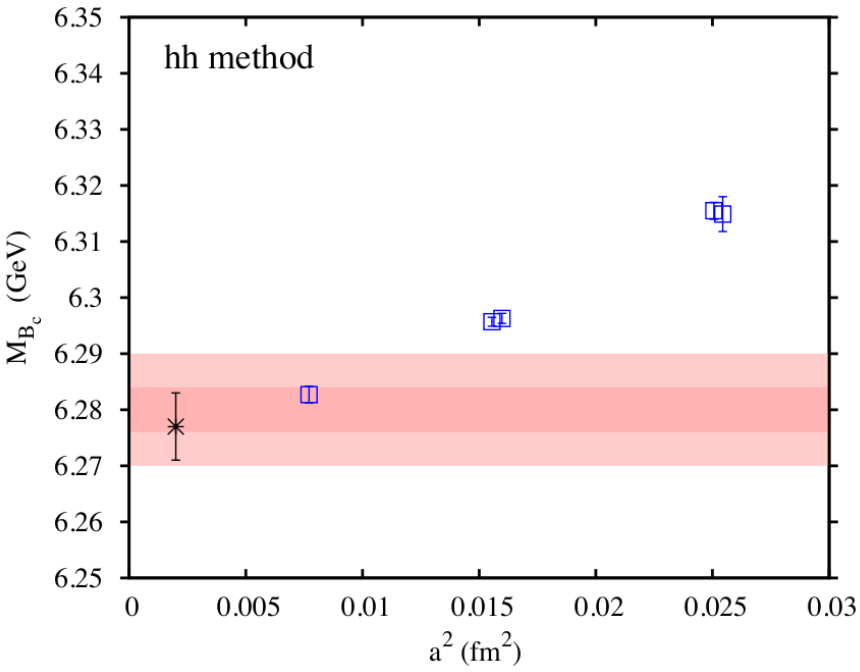

Figure 4.18: Mass of the B_c meson as a function of lattice spacing. Error bars are statistical, lattice spacing errors and tuning errors in the valence quark masses. The shaded band is the physical result allowing for sea quark mass and lattice spacing, and is described in detail in [64]. The burst symbol represents experiment.

One can then use the experimental values for $E_0(B_s^*) - E_0(B_s)$ and M_{B_c} to convert R in to a value for the mass of the B_c^* with a result [62] of 6.330(7)(2)(6) GeV, where errors are statistical, systematic and experimental respectively. Between the HISQ treatment of the c quarks, and the use of the random wall algorithm, this was the most accurate lattice prediction of a gold-plated hadron mass that has been made to date.

Chapter 5

The NRQCD Dispersion Relation

The NRQCD action coefficients c_i are all 1.0 at tree level[41], as can be seen by earlier matching in chapter 3; however these coefficients have $\mathcal{O}(\alpha_s)$ corrections which have not been taken in to account. These corrections look like, for example

$$c_i = 1 + \delta c_i \times \alpha_s + ... \tag{5.1}$$

One would therefore expect some systematic errors to arise from the NRQCD action that we have used.

Such errors would arise in quantities such as the energy of the simulated meson as a function of momentum. Using the dispersion relation

$$M_{kin}(\mathbf{p}) = \frac{\mathbf{p}^2 - \Delta E^2}{2\Delta E}. \tag{5.2}$$

In the real world, M_{kin} should be a constant. On the lattice, this will not be the case, and M_{kin} may vary not only with $\mathbf{p}$, but with the different components of $\mathbf{p}$ due to the loss of rotational invariance caused by the lattice. We can investigate this very accurately thanks to the random wall techniques developed in chapter 4.

We simulate η_b and Υ over a range of momenta on a number of ensembles, paying special attention to $p^2 = 9$ since it can be represent on the lattice as both $(3, 0, 0)$ and $(2, 2, 1)$.

5.1 Calculations on the Very Coarse 0097 ensemble

We start our investigation on the 0097/0484 "very coarse" ensemble because this is computationally the fastest.

Using $c_i = 1.0$, we calculate the kinetic mass of the Υ and the η_b for a number of different momenta, the results of which are summarised in table 5.1 and plotted in figure 5.1. In all applicable cases, we have averaged over all permutations of axes [e.g. $E|_{p^2=1}$ is taken from $\frac{1}{3}\left(E|_{(1,0,0)} + E|_{(0,1,0)} + E|_{(0,0,1)}\right)$].[1] We fit momentum 0 and p^2 together, which allows us to fit ΔE more accurately since the errors in the individual energies are correlated.

In figure 5.1, we fit not only the Υ and η_b, but also the spin average, which is defined as

$$M_{\text{spin-avg}} = \frac{3M_\Upsilon + M_{\eta_b}}{4}. \tag{5.3}$$

The results have some notable undesirable features. The "off-axis" momenta give consistent values of the kinetic mass (as expected), but the "on-axis" points (those that carry all their momentum along one lattice axis) lie on a gradient that deviates from the base line. In particular, this means that the $(2, 2, 1)$ and $(3, 0, 0)$ have a significant splitting - around ten standard deviations - when one would expect the results to be equal. Additionally the η_b results are higher than those of the Υ, which would give the hyperfine splitting the wrong sign.

The significant term in the action that is sensitive to the difference between $(3, 0, 0)$ and $(2, 2, 1)$ is the p_i^4 term (c_5), as all other terms are either insensitive to momentum (c_2, c_3, c_4), or sensitive to p^2 (c_1, c_6) which affects $(3, 0, 0)$ and $(2, 2, 1)$ equally. If one assumes that the momentum of the meson is always divided equally between the valence quarks, then one can calculate an approximation to the change in the p_i^4 coefficient c_5

[1] For simplicity, we generally refer only to one "cardinal" direction in the text to stand for all. Thus, for example, $(3, 0, 0)$ may be understood to mean (3,0,0); (0,3,0); and (0,0,3) unless otherwise stated.

	Υ				η_b			
p^2	$E_0\|_{(0,0,0)}$	$E_0\|_{p^2}$	ΔE	aM_{kin}	$E_0\|_{(0,0,0)}$	$E_0\|_{p^2}$	ΔE	aM_{kin}
1	0.287679(95)	0.298373(94)	0.010694(22)	7.204(20)	0.250830(72)	0.261357(73)	0.010527(13)	7.319(9)
2	0.287711(90)	0.309075(91)	0.021364(31)	7.206(16)	0.250875(69)	0.271910(71)	0.021035(15)	7.321(5)
3	0.287635(97)	0.319731(106)	0.032096(63)	7.200(18)	0.250860(69)	0.282445(73)	0.031584(25)	7.308(6)
4	0.287727(90)	0.330250(95)	0.042523(28)	7.243(10)	0.250844(71)	0.292625(77)	0.041781(24)	7.361(4)
6	0.287648(97)	0.351461(134)	0.063813(93)	7.213(09)	0.250823(71)	0.313528(100)	0.062705(64)	7.347(8)
8	0.287699(89)	0.372685(120)	0.084986(66)	7.216(05)	0.250864(67)	0.334302(83)	0.083438(36)	7.351(3)
$9\|_{(3,0,0)}$	0.287677(93)	0.382063(146)	0.094385(97)	7.311(12)	0.250804(70)	0.343383(107)	0.092579(70)	7.450(6)
$9\|_{(2,2,1)}$	0.287685(92)	0.383362(120)	0.095677(83)	7.199(08)	0.250820(71)	0.344637(120)	0.093818(92)	7.350(7)

Table 5.1: Fit results for kinetic masses at various momenta on the 0097/0484 very coarse ensemble. $c_i = 1.0$

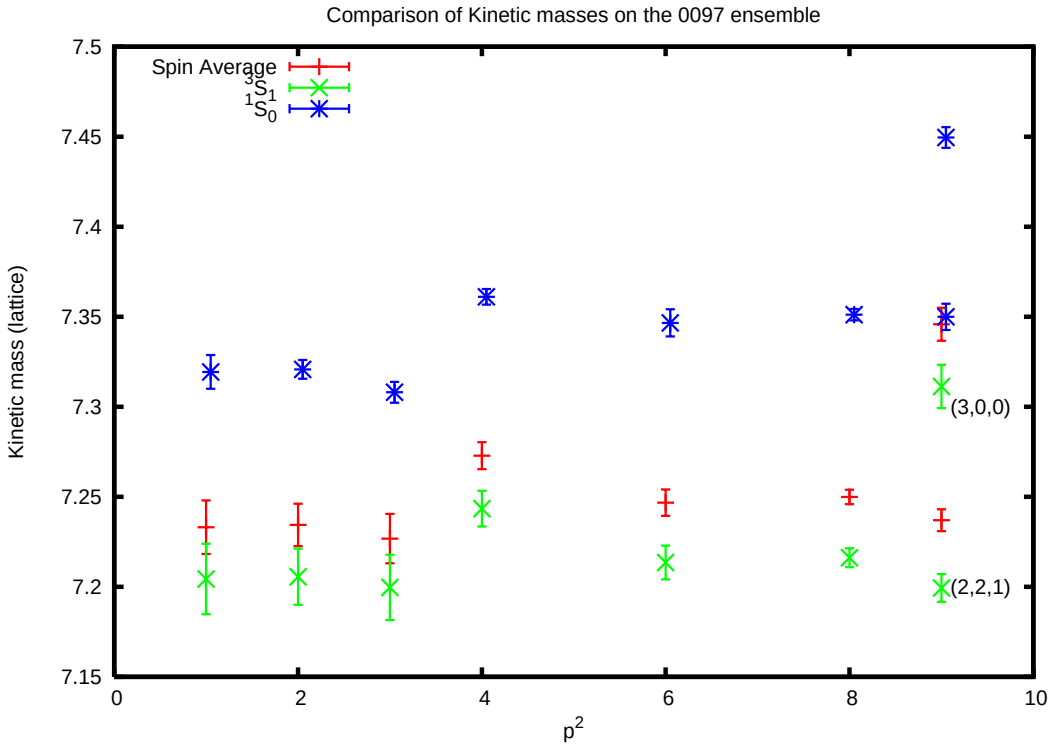

Figure 5.1: Kinetic masses in lattice units for the 0097/0484 ensemble with $c_i = 1.0$.

required to make the difference vanish. In practice, this value will not be correct (due to the over-simplified assumption), but will allow one to quickly home in on the correct value. Using this technique, I estimated a value of $c_5 = 2.6$, and this value does indeed have the desired effect of removing the $(3,0,0) - (2,2,1)$ splitting: $\Delta M_{kin} = 0.008(10)$. However, this coefficient also creates a strong, and undesirable, momentum dependence on the value of the kinetic mass, which can be seen in figure 5.2.

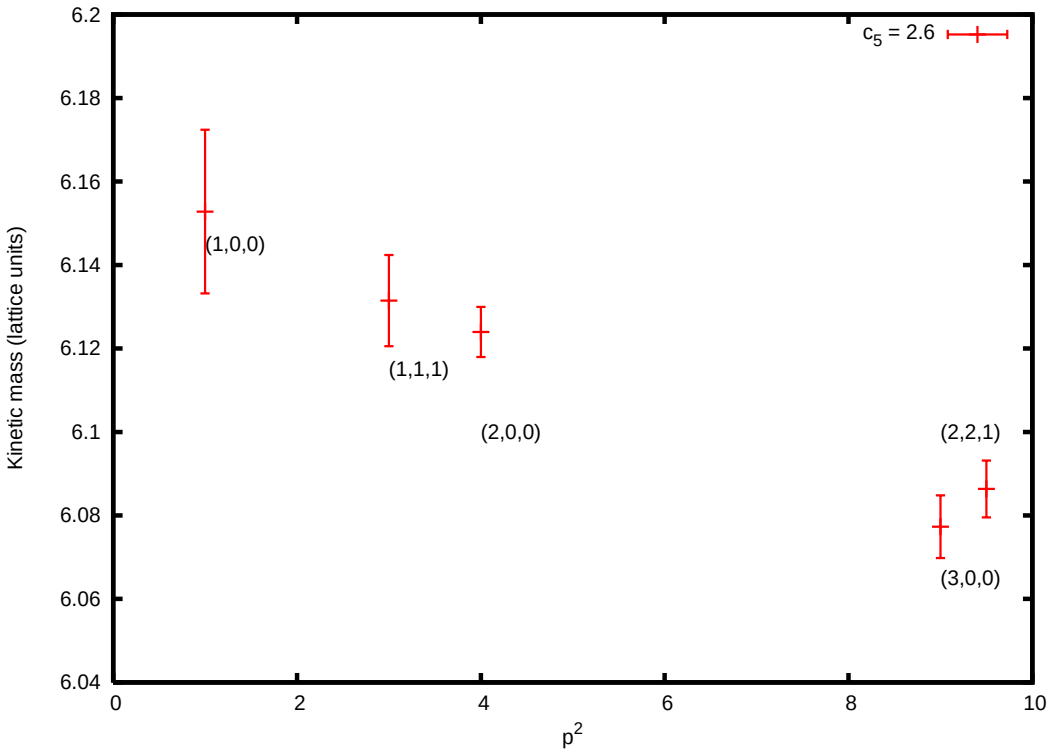

Figure 5.2: Kinetic masses for the Υ in lattice units for the 0097/0484 ensemble with $c_5 = 2.6$.

Eike Müller [65] has calculated corrections, the δc_i's in equation 5.1, to the tree level coefficients c_1, c_5 and c_6 of the action using perturbation theory by calculating the one-loop (see figure 5.3) NRQCD quark self-energy

$$\Sigma(w, \mathbf{p}) = \Sigma_0(w) + \Sigma_1(w)\frac{\mathbf{p}^2}{2m} + \Sigma_2(w)\frac{(\mathbf{p}^2)^2}{8m^2} + \Sigma_3(w)\mathbf{p}^4 \tag{5.4}$$

He then demands that the quark match full relativistic QCD. Expanding in w, he finds expressions for c_1 and c_5 (and also c_6, as we will describe shortly). This method is not

dissimilar to the rationale we used to calculate $c_5 = 2.6$, except that we calculate the meson directly, whereas Eike Müller calculates for the valence quarks. Correcting the quarks should correct the meson to the same order.

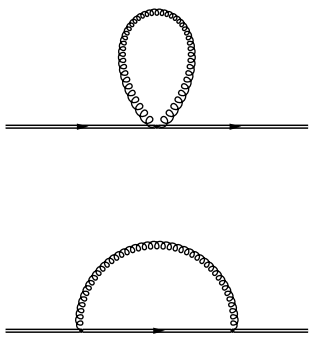

Figure 5.3: Feynman diagrams which contribute to the heavy quark self-energy. The solid line represents a heavy quark, and the patterned line a gluon.

Using these correction terms, we evolve α_s in equation 5.1 to the appropriate energy scale q^* for each coefficient, as found in Morningstar [41] which gives values of aq^*. In principle, the energy scales to which we evolve are sensitive to the bare quark mass aM, however the figures in [41] change the stability parameter n for different aM, which we do not. We therefore choose to use a single value for each aq^*, taken at $aM = 3.4$. We expect the aq^* curves to be flatter than those presented in [41] when n is kept constant, and so we do not expect aq^* to change significantly in our case. On this basis, we evolve to $\alpha_s(\frac{1.8}{a})$ for c_1 and for c_5 we evolve to $\alpha_s(\frac{1.4}{a})$. We use our previous determination of α_s as a starting point for the evolution: $\alpha_V(7.5\text{GeV}, n_f = 3) = 0.2120(28)$.

The δc_i are sensitive to the bare quark mass (expressed in lattice units), and these are tabulated along with our results for the coefficients in table 5.2.

Ensemble	aM	δc_1	δc_5	c_1	c_5	c_6
0097/0484	3.4	0.952(30)	0.445(10)	1.36	1.21	1.36
010/050	2.8	0.951(26)	0.406(11)	1.31	1.16	1.31
0062/031	1.95	0.774(21)	0.392(17)	1.21	1.12	1.21

Table 5.2: Perturbative coefficients for the NRQCD action.

The coefficients c_1 and c_6 have a redundancy as they both multiply the $(\Delta^{(2)})^2$ term. In principle, one can simply combine the terms as in [65], such that

$$\tilde{c}_1 = (c_1 + \frac{m}{2n}c_6)/(1 + \frac{m}{2n}), \tag{5.5}$$

thus we always set $c_1 = c_6$. Using these coefficients in the action (table 5.2), I re-ran the lattice simulations for the kinetic masses on the 0097 ensemble, see table 5.3 and figure 5.4. The effect is not of high significance, but it does reduce the $(3,0,0) - (2,2,1)$ splitting; $\Delta M_{kin} = 0.087(15)$, or nearly seven standard deviations (c.f. ten standard deviations from the tree level case).

	Υ				η_b			
p^2	$E_0\|_{(0,0,0)}$	$E_0\|_{p^2}$	ΔE	aM_{kin}	$E_0\|_{(0,0,0)}$	$E_0\|_{p^2}$	ΔE	aM_{kin}
1	0.289633(95)	0.300344(95)	0.010711(23)	7.187(18)	0.252776(72)	0.263310(74)	0.010533(15)	7.315(10)
2	0.289669(91)	0.311087(92)	0.021418(32)	7.190(15)	0.252773(72)	0.273820(76)	0.021047(25)	7.317(9)
3	0.289599(97)	0.321719(106)	0.032120(63)	7.191(15)	0.252773(72)	0.284323(80)	0.031549(37)	7.316(9)
4	0.299418(74)	0.342266(76)	0.042849(89)	7.217(9)	0.252812(71)	0.294674(77)	0.041862(19)	7.347(3)
$9\|_{(3,0,0)}$	0.289601(97)	0.384238(166)	0.094636(121)	7.291(12)	0.252757(71)	0.345530(108)	0.092773(71)	7.434(6)
$9\|_{(2,2,1)}$	0.289603(96)	0.385322(126)	0.095719(96)	7.204(9)	0.252771(71)	0.346477(121)	0.093707(93)	7.359(7)

Table 5.3: Fit results for kinetic masses at various momenta on the 0097/0484 very coarse ensemble. $c_1 = c_6 = 1.36$, $c_5 = 1.21$.

5.1.1 The Hyperfine Splitting

We can also compare the results of modifying the c_i coefficients on the hyperfine splitting as a function of momentum. From our lattice simulations, we can extract the spin-dependent hyperfine slitting in two way. Firstly, we can simply take the differences of the

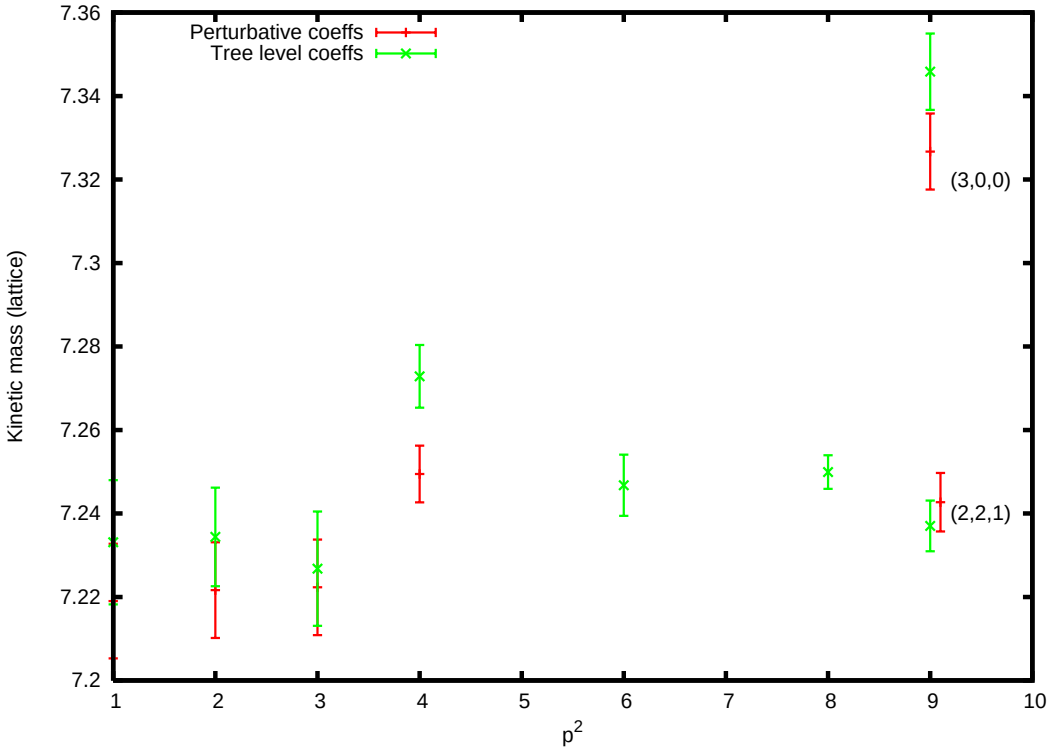

Figure 5.4: Kinetic masses for the Υ in lattice units for the 0097/0484 ensemble, comparing results with c_i=1.0 with c_i as in table 5.2.

ground-state Υ and η_b energies at zero momentum. Since the Υ and η_b data from each configuration-origin is correlated with data from the others, making concurrent fits to this splitting will yield a more accurate result than simply subtracting the values from chapter 4; results from a concurrent fit, first for tree level coefficients $c_i = 1.0$, are tabulated in 5.4.

We plot the hyperfine splitting from the concurrent fit in figure 5.5, in which we also include a line for the expected hyperfine splitting at a given momentum. This is calculated

as:

$$E(p^2) = \sqrt{p^2 + M^2} = M + \frac{p^2}{2M} \tag{5.6}$$

$$\begin{aligned} dE(p^2 \neq 0) &= (M_\Upsilon - M_{\eta_b}) + \frac{p^2}{2M_\Upsilon} - \frac{p^2}{2M_{\eta_b}} \\ &= dE(0) + \frac{p^2}{2(M_{\eta_b} + dE(0))} - \frac{p^2}{2M_{\eta_b}}, \end{aligned} \tag{5.7}$$

where M_{η_b} is chosen at some momentum (usually (1,1,1) where available since we do not need to worry about permutations of axes), and then kept constant. We see a large deviation from the expected line, although this is to be expected, and is consistent with the fact that out Υ and η_b kinetic masses are wrong (in particular that their difference has the wrong sign).

p^2	$E_0(^3S_1) - E_0(^1S_0)$
0.0	0.036798(53)
1.0	0.036971(45)
2.0	0.037130(56)
3.0	0.037335(59)
4.0	0.037501(70)
6.0	0.037952(69)
8.0	0.038442(83)
$9.0\vert_{(3,0,0)}$	0.038599(88)
$9.0\vert_{(2,2,1)}$	0.038719(106)

Table 5.4: The spin-dependent hyperfine splitting $\Upsilon - \eta_b$ on the 0097/0484 ensemble at $c_i = 1.0$.

One could also extract the splitting, in principle, by calculating the kinetic mass of both particles, and taking the difference. However, as noted earlier in this chapter, this gives the wrong sign for the splitting. The simulation data has a self-consistency issue in which the η_b has a lower mass than the Υ, yet has a higher kinetic mass. In figure 5.6, a

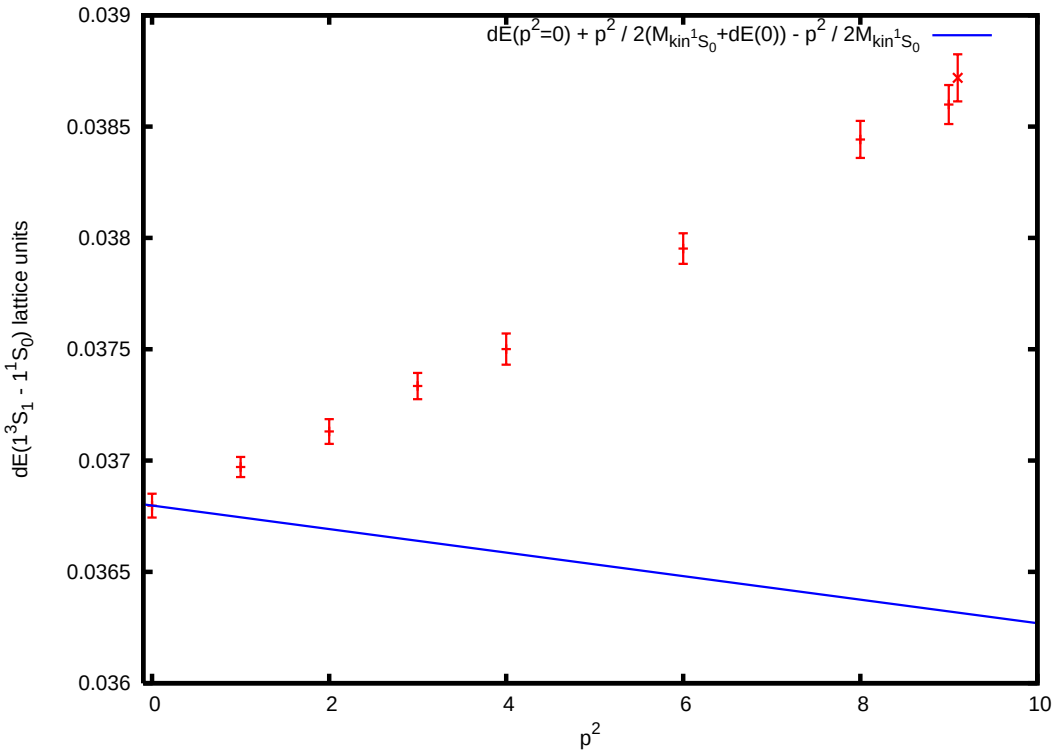

Figure 5.5: Hyperfine splitting as a function of momenta on the 0097/0484 ensemble ($c_i = 1.0$). The solid line is the expected splitting, calculated using equation 5.8, where M is taken from the kinetic mass at $p = (1, 1, 1)$. The cross represents $p^2 = (2, 2, 1)$.

comparison of direct and kinetic mass based determinations of the hyperfine splitting is plotted for momenta ranging from $p^2 = 0$ to $p^2 = 9$.

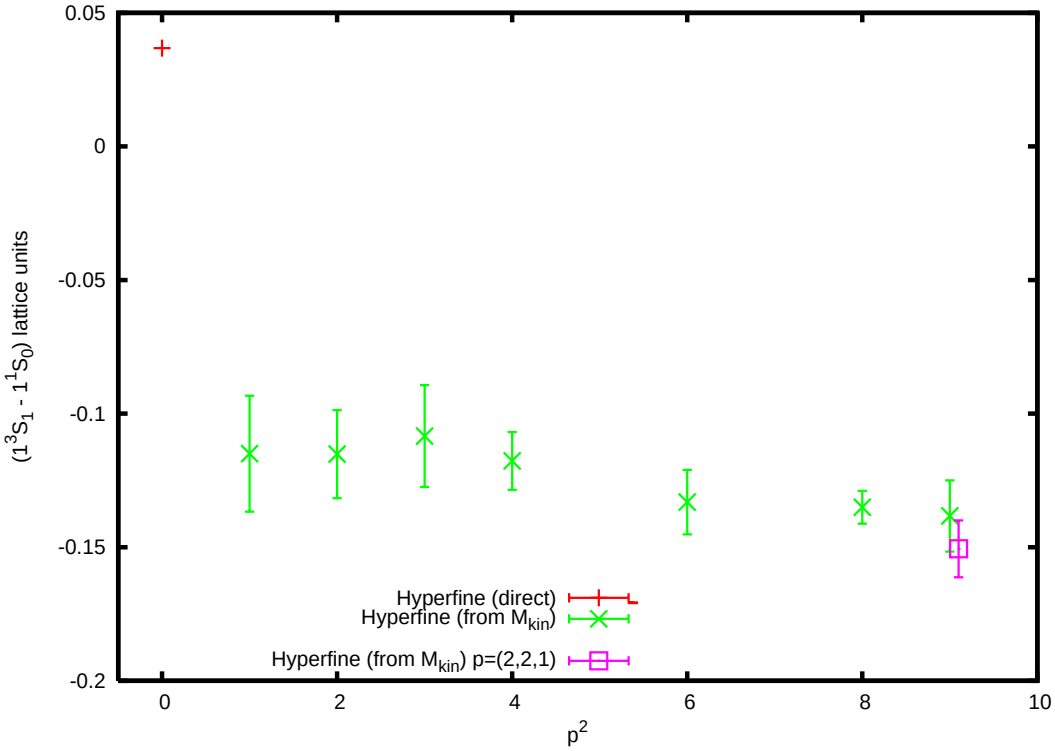

Figure 5.6: Hyperfine splittings in lattice units for the 0097/0484 ensemble with $c_i = 1.0$. The difference in kinetic masses between the Υ and the η_b are inconsistent with the hyperfine splitting as extracted directly from the simulation data.

Continuing in this vein, we repeat the above for the perturbative coefficients of table 5.2, which can be seen in table 5.5 and in figure 5.7. These are not significantly different from the tree level case, which is as expected since we have not modified any terms to which the hyperfine splitting is sensitive, specifically the spin-dependent terms c_3 and c_4, which contain a σ. We will revisit this issue on the coarse ensemble, where we will modify the spin sensitive term c_4.

p^2	$E_0(^3S_1) - E_0(^1S_0)$
0.0	0.036806(54)
1.0	0.036980(50)
2.0	0.037168(55)
3.0	0.037374(58)
4.0	0.037559(83)
$9.0\|_{(3,0,0)}$	0.038708(88)
$9.0\|_{(2,2,1)}$	0.038823(106)

Table 5.5: The spin-dependent hyperfine splitting $\Upsilon - \eta_b$ on the 0097/0484 ensemble at $c_1 = c_6 = 1.36$, $c_5 = 1.21$.

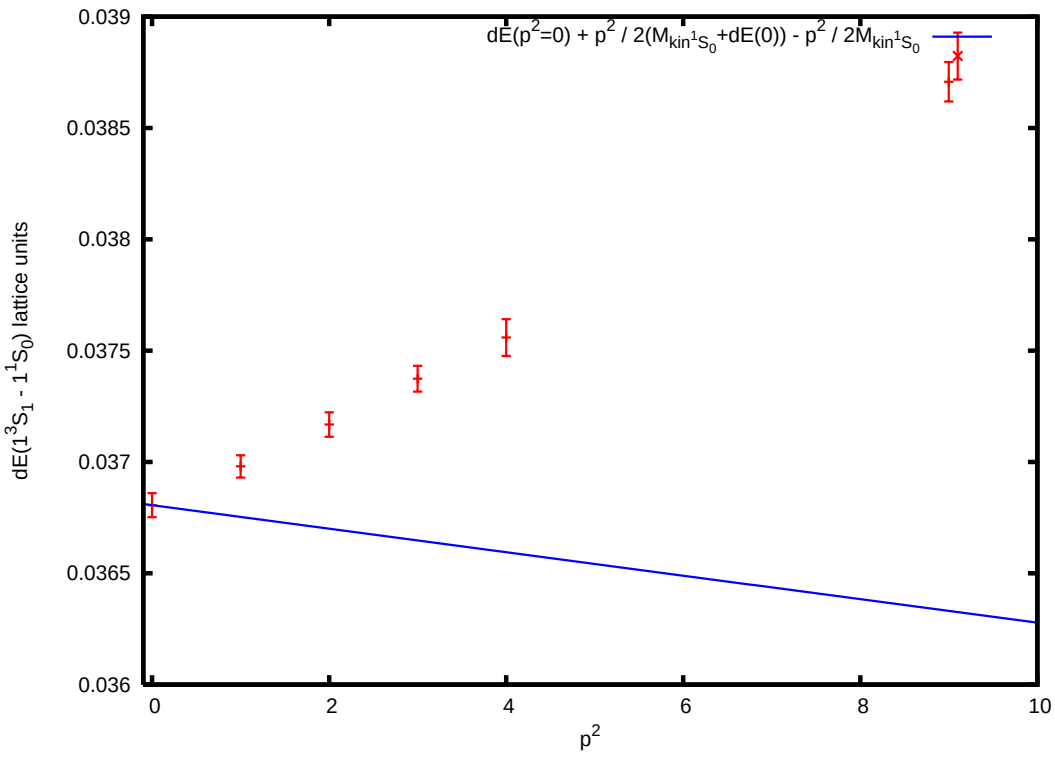

Figure 5.7: Hyperfine splitting as a function of momenta on the 0097/0484 ensemble ($c_1 = c_6 = 1.36$, $c_5 = 1.21$). The solid line is the expected splitting, as in equation 5.8 with M_{η_b} taken at (1,1,1). The cross represents $p^2 = (2, 2, 1)$.

5.1.2 Improvement to p^6

We may also attempt to improve the NRQCD action dispersion relation by improving the action to $\mathcal{O}(p^6)$. We implement this change in two stages. First, we remove p_i^6 terms by modifying the $\Delta^{(4)}$ operator:

$$\Delta^{(4)} \to \Delta^{(4)} + \frac{\Delta^{(6)}}{6} \tag{5.8}$$

then, in addition to this, we modify the operator $\Delta \cdot E$ to improve it through $\mathcal{O}(\alpha^2)$ by improving the Δ operator.

$$\Delta \to -\frac{1}{6}\left(U_\mu(x+\hat{\mu})U_\mu(x) - U_\mu^\dagger(x-2\hat{\mu})U_\mu^\dagger(x-\hat{\mu})\right) + \frac{4}{3}\left(U_\mu(x) - U_\mu^\dagger(x-\hat{\mu})\right) \tag{5.9}$$

We then calculate the splitting between the two $p^2 = 9$ states for both the Υ and η_b, which are plotted in figure 5.8. We can see that making this order improvement reduces the splitting by a factor of approximately 2. The change to the $\Delta \cdot E$ term would seem to work against us, but should be included to make the level of improvement in the action consistent.

5.1.3 Tuning the Darwin Term Coefficient

We test the effects of modifying the spin-independent term c_2, known as the Darwin term, in the NRQCD action to investigate how important it is to the dispersion relation, and how feasible it is to non-perturbatively tune. First we examine the effect on the spin-dependent splitting $\Upsilon - \eta_b$, then we calculate the kinetic mass in each case.

As in initial guess, we increase c_2 to $c_2 = 3.0$, a shift of $+2.0$. This decreases the hyperfine splitting, which was already decreased when we changed c_5 to 2.6. We make another attempt, this time shifting c_2 by -2.0, so that $c_2 = -1.0$, increasing the hyperfine splitting slightly. A comparison of these simulations with the $c_2 = 1.0$ can be seen in figure 5.9. It is clear from this plot that in order to remove the shift in the spin-dependent caused by retuning c_5 would require a significant shift in c_2.

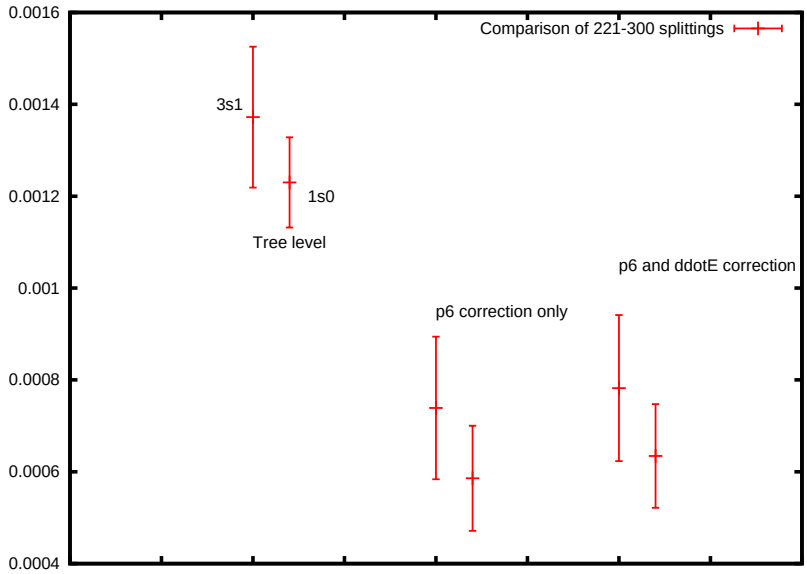

Figure 5.8: Splittings between the $p^2 = 9$ terms E(p=(2,2,1)) - E(p=(3,0,0)) [y-axis, in lattice units], for the unimproved case, and for both levels of improvement given in the text (equations 5.8 and 5.9).

One may also compare the kinetic masses from each of these simulations in order to assess the kinetic mass' sensitivity to this term. We expect that the kinetic mass will not change significantly with this coefficient. This expectation is supported by figure 5.10, particularly when one considers the magnitude of the changes to c_2.

We conclude that the effect of the Darwin term on such quantities is small, and unlikely to have a major effect on our results. It is therefore not of great importance to improve c_2 beyond the tree level value of 1.0.

5.1.4 Summary

The very coarse ensemble has demonstrated a number of issues with the NRQCD action. We have a consistency issue at tree level with the kinetic mass as a function of momentum, in particular at the degenerate momentum $p^2 = 9$. While we can naïvely correct the discrepancy at $p^2 = 9$ via non-perturbative tuning, this approach is inadequate overall.

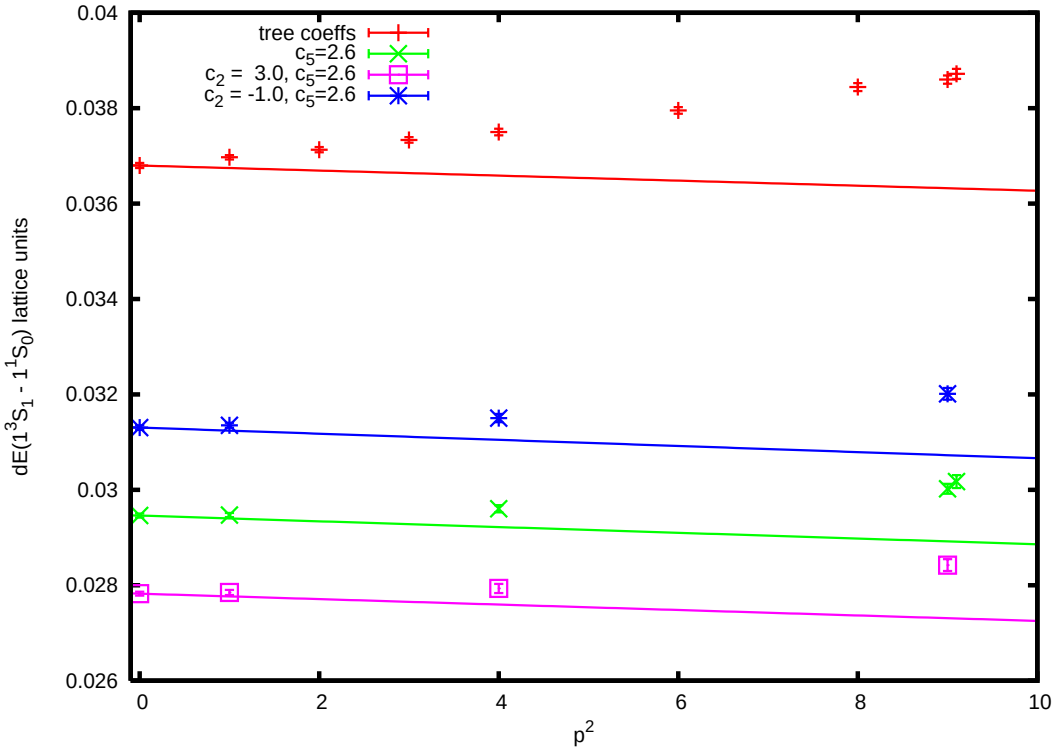

Figure 5.9: Hyperfine splitting as a function of momenta on the 0097/0484 ensemble. The solid line is the expected splitting, as in equation 5.8 using M_{η_b} at (1,1,1).

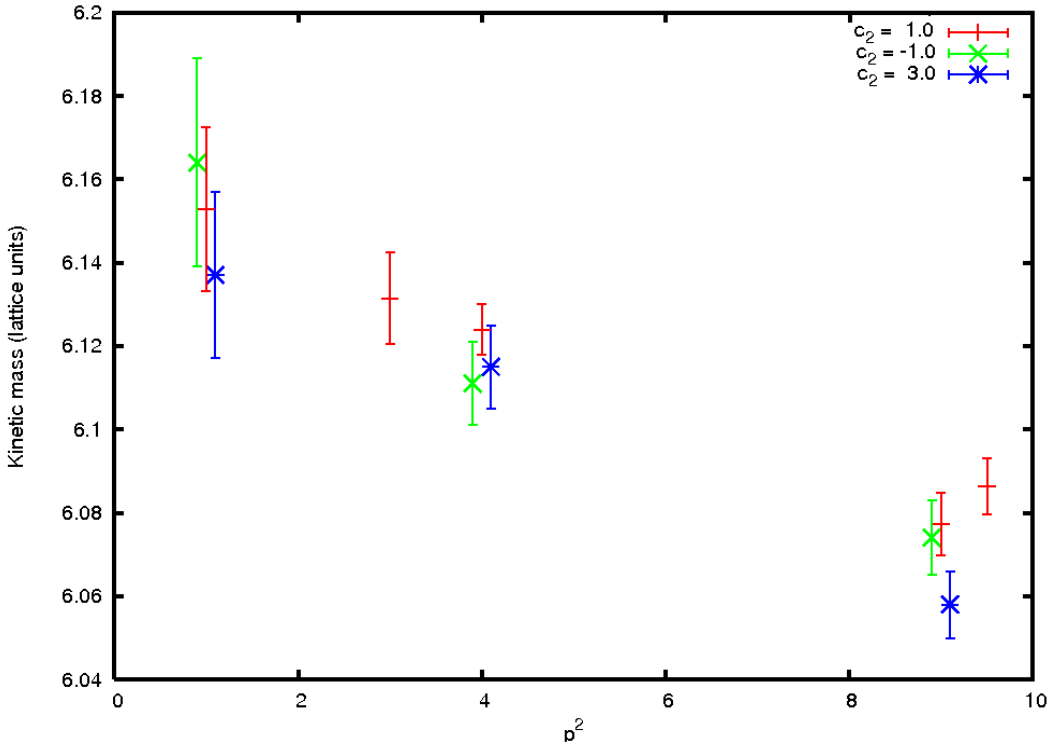

Figure 5.10: Υ kinetic mass as a function of momenta on the 0097/0484 ensemble. We compare the resulting kinetic masses from setting $c_2 = 3.0$ and $c_2 = -1.0$ with the kinetic masses from $c_2 = 1.0$. In all three cases, $c_5 = 2.6$ as in figure 5.2 in section 5.1.

If, instead, we use perturbative coefficients then this goes some way to ameliorating the $p^2 = 9$ situation.

We also have a problem with the hyperfine splitting, which has the wrong sign when calculated from kinetic masses. This causes the hyperfine splitting to scale incorrectly as a function of momentum. To truly study these effects, we will need to look at finer lattices, and so I repeat these simulations on the 010/050 coarse and 0062/031 fine ensembles.

5.2 Coarse and Fine Simulations

We calculate the perturbative values of the NRQCD coefficients for use on the 010/050 and 062/0031 ensembles, as tabulated in table 5.2. We fit Υ and η_b propagators at a variety of momenta, as tabulated in 5.6 and 5.7. In the coarse run, we have added an extra much higher momentum state in the form of $p = (3, 3, 3)$. We wished to see the effects of high momentum on the kinetic masses and hyperfine splittings as a function of p^2, although we find the error bars are prohibitive.

Since the $p^2 = 9$ splitting is a discretisation problem, it should vanish as we approach the continuum. The coarse ensemble, plotted in figures 5.11 and 5.12, shows a more significant improvement than the "very coarse", consistent with what one would expect.

Once we reach the granularity of the fine ensemble, plotted in figures 5.13 and 5.14, the $p^2 = 9$ splitting is small, and has all but disappeared in the simulations using perturbative coefficients. The tree level results are now within about 1.5 standard deviations of each other, and the perturbatively tuned results are within 1.

One can be confident that this discretisation phenomenon will not affect results after extrapolation to the continuum has occurred. The use of coefficients calculated in perturbation theory, as in [65], diminishes the effect and removes the erroneous splitting faster.

	Υ				η_b			
p^2	$E_0\|_{(0,0,0)}$	$E_0\|_{p^2}$	ΔE	aM_{kin}	$E_0\|_{(0,0,0)}$	$E_0\|_{p^2}$	ΔE	aM_{kin}
	$c_i = 1.0$							
1	0.292656(69)	0.300917(69)	0.008262(16)	5.969(12)	0.260735(52)	0.268923(52)	0.008187(8)	6.024(6)
3	0.292644(69)	0.317456(76)	0.024812(43)	5.954(10)	0.260727(52)	0.285274(54)	0.024547(23)	6.019(6)
4	0.292642(70)	0.325580(81)	0.032938(32)	5.976(6)	0.260727(52)	0.293324(57)	0.032597(19)	6.039(4)
$9\|_{(3,0,0)}$	0.292637(69)	0.366251(97)	0.073614(59)	5.996(5)	0.260715(51)	0.333534(61)	0.072819(30)	6.063(3)
$9\|_{(2,2,1)}$	0.292629(68)	0.366605(102)	0.073976(70)	5.967(6)	0.260712(51)	0.333944(65)	0.073232(40)	6.028(3)
27	0.292663(69)	0.51085(95)	0.21819(94)	5.997(27)	0.260737(52)	0.47675(37)	0.21601(37)	6.060(11)
	$c_1 = c_6 = 1.31$, $c_5 = 1.16$; $c_2 = c_3 = c_4 = 1.0$							
1	0.297657(69)	0.305880(69)	0.008222(17)	5.998(12)	0.265319(52)	0.273452(52)	0.008133(8)	6.064(6)
3	0.297644(70)	0.322321(76)	0.024677(43)	5.987(10)	0.265311(52)	0.289680(54)	0.024369(23)	6.063(6)
4	0.297760(63)	0.330592(67)	0.032832(13)	5.996(2)	0.265337(51)	0.297743(54)	0.032406(11)	6.075(2)
$9\|_{(3,0,0)}$	0.297636(69)	0.370893(96)	0.073257(58)	6.026(5)	0.265298(51)	0.337622(61)	0.072324(29)	6.105(2)
$9\|_{(2,2,1)}$	0.297627(69)	0.37112(10)	0.073493(71)	6.006(6)	0.265302(50)	0.337908(63)	0.072606(37)	6.081(3)
27	0.297662(69)	0.51352(92)	0.21585(92)	6.065(27)	0.265320(52)	0.47857(35)	0.21325(35)	6.141(10)

Table 5.6: Kinetic masses on the 010/050 coarse ensemble. The upper half of the table represents tree level coefficients, whereas the lower half uses the perturbative coefficients.

	Υ				η_b			
p^2	$E_0\|_{(0,0,0)}$	$E_0\|_{p^2}$	ΔE	aM_{kin}	$E_0\|_{(0,0,0)}$	$E_0\|_{p^2}$	ΔE	aM_{kin}
	$c_i = 1.0$							
1	0.266279(50)	0.272136(49)	0.005857(14)	4.296(10)	0.240867(34)	0.246704(34)	0.005837(6)	4.311(4)
2	0.266303(49)	0.289748(59)	0.023446(21)	4.284(4)	0.240895(34)	0.264192(38)	0.023297(10)	4.311((2)
$9\|_{(3,0,0)}$	0.266231(53)	0.318832(73)	0.052601(56)	4.282(5)	0.240885(34)	0.293092(43)	0.052208(22)	4.314(2)
$9\|_{(2,2,1)}$	0.266205(52)	0.318882(76)	0.052677(60)	4.275(5)	0.240867(33)	0.293127(44)	0.052260(27)	4.310(2)
	$c_1 = c_6 = 1.21$, $c_5 = 1.12$; $c_2 = c_3 = c_4 = 1.0$							
1	0.277899(50)	0.283728(59)	0.005828(14)	4.317(10)	0.251901(34)	0.257695(34)	0.005794(6)	4.343(5)
$9\|_{(3,0,0)}$	0.277859(50)	0.330120(70)	0.052260(44)	4.310(4)	0.251912(33)	0.303692(42)	0.051780(21)	4.350(2)
$9\|_{(2,2,1)}$	0.277838(50)	0.330140(75)	0.052302(53)	4.306(3)	0.251893(33)	0.303692(44)	0.051799(26)	4.349(2)

Table 5.7: Kinetic masses on 0062/031 fine ensemble. The upper half of the table represents tree level coefficients, whereas the lower half uses the perturbative coefficients.

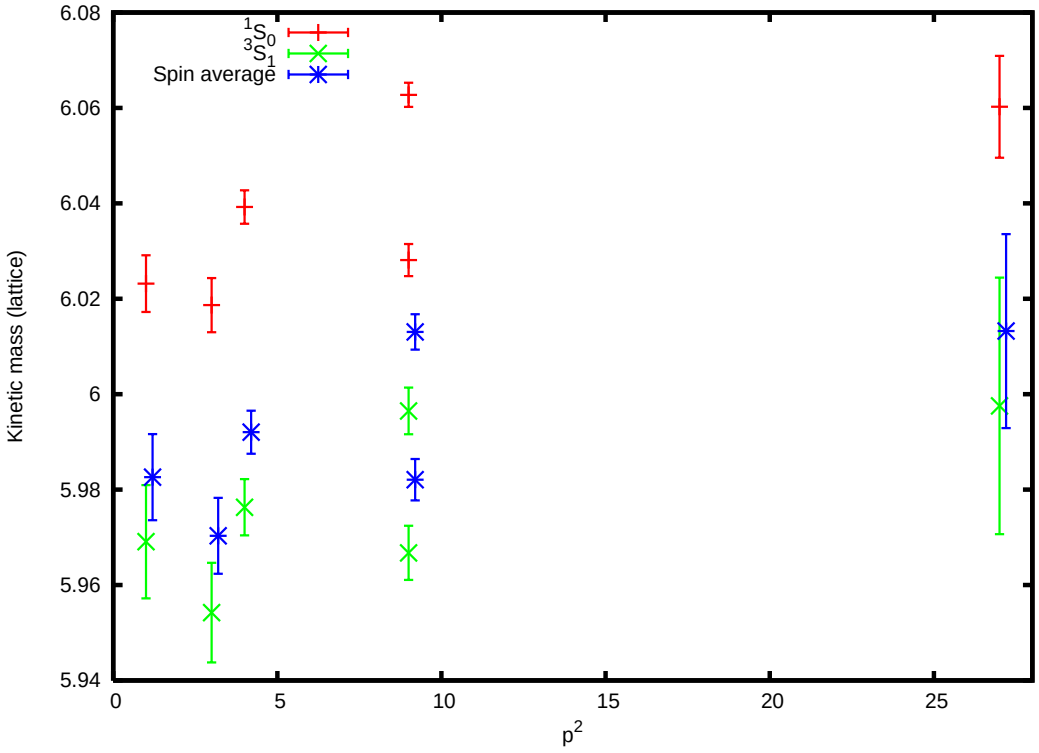

Figure 5.11: Kinetic masses in lattice units for the 010/050 ensemble with $c_i = 1.0$.

These results, however, continue to display the feature that the hyperfine splitting, as determined from the difference in the kinetic masses Υ and η_b calculated here, still has the wrong sign.

5.3 Hyperfine Splittings

We return to the spin dependent splitting $\Upsilon - \eta_b$, now simulated on the coarse and fine ensembles from the previous section. There we focused on the splitting between $M_{kin}(3,0,0)$ and $M_{kin}(2,2,1)$ for the same spin state, however tables 5.6 and 5.7 also show that for any given momentum, the kinetic mass of the η_b is higher than the Υ.

It would seem that the inconsistency between a direct determination of the hyperfine splitting, and the splitting taken from the kinetic masses of the two spin states remains despite simulating on lattices closer to the continuum. In figures 5.15 and 5.16, we once

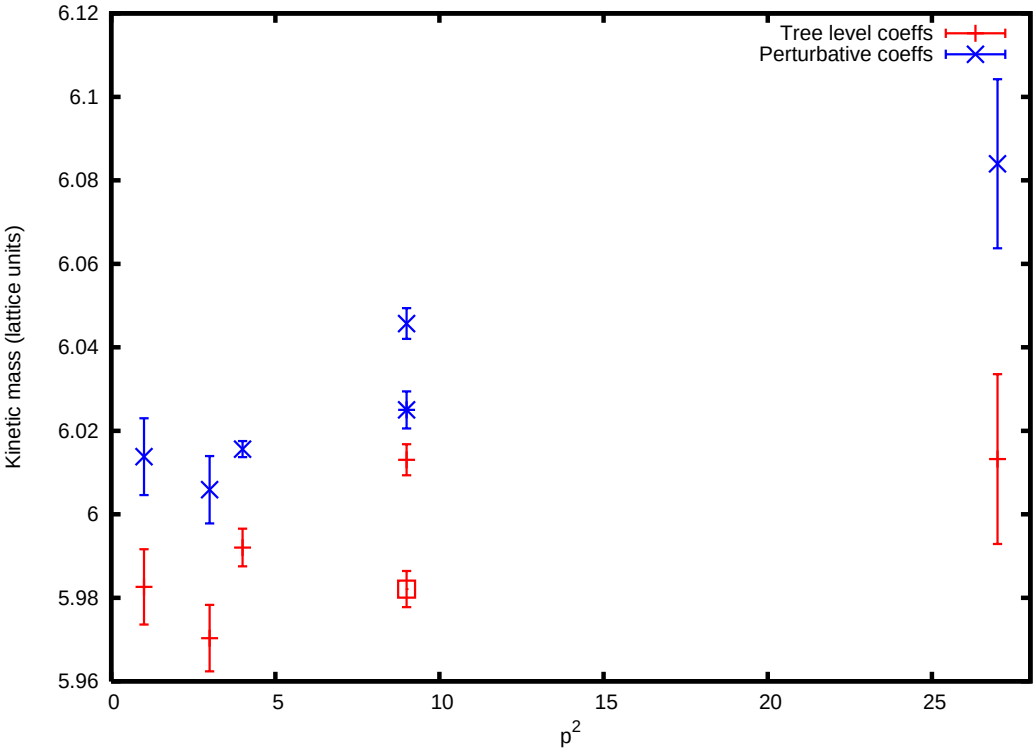

Figure 5.12: Spin-averaged $b\overline{b}$ kinetic masses in lattice units for the 010/050 ensemble, comparing results with c_i=1.0 with c_i as in table 5.2. The splitting between (3,0,0) and (2,2,1) is slightly reduced in the latter case. The momentum (2,2,1) has a different symbol from the rest of the series in each case (a box for the dash series, and a burst for the cross series).

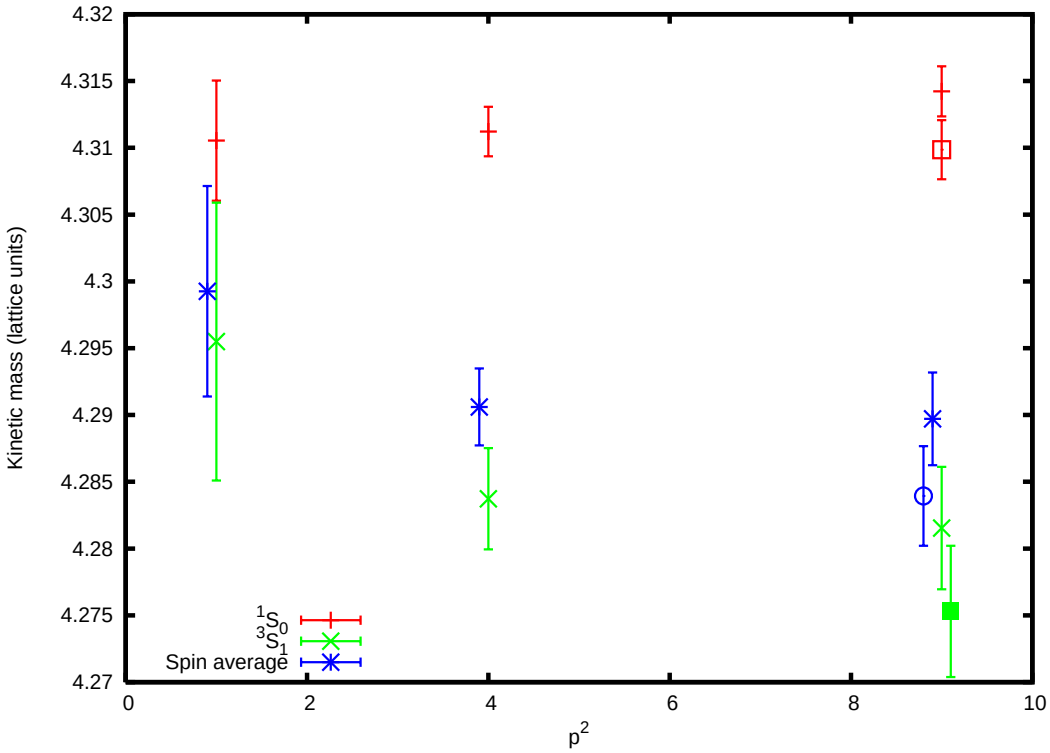

Figure 5.13: Kinetic masses in lattice units for the 0062/031 ensemble with $c_i = 1.0$. The $(2, 2, 1)$ data point is shown with an open-box for the ${}^1S_0$, a closed-box for the ${}^3S_1$ and a circle for the spin-average.

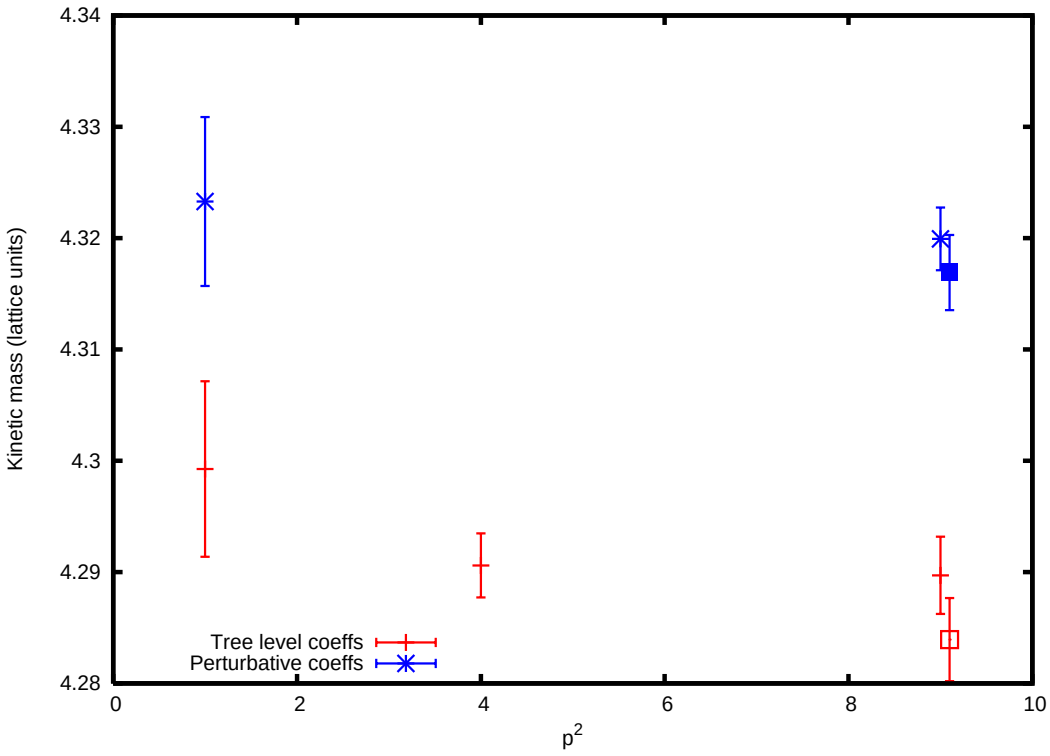

Figure 5.14: Spin-averaged $b\bar{b}$ kinetic masses in lattice units for the 0062/031 fine ensemble, comparing results with c_i=1.0 with c_i as in table 5.2. The splitting between (3,0,0) and (2,2,1), which is small in the tree level case, is consistent with zero in the perturbative case. The momentum (2,2,1) has a different symbol from the rest of the series in each case: the open-box belongs to the tree level data series, and the closed-box to the perturbative.

again plot the hyperfine splitting as a function of momentum along with a line indicating the expected behaviour. The line and points should correspond, but they do not - just as in the very coarse ensemble. Again, this is due to the incorrect relationship between the Υ and η_b kinetic masses, the wrong sign in the splitting effectively giving the wrong sign to the gradient of the hyperfine data points as a function of p^2.

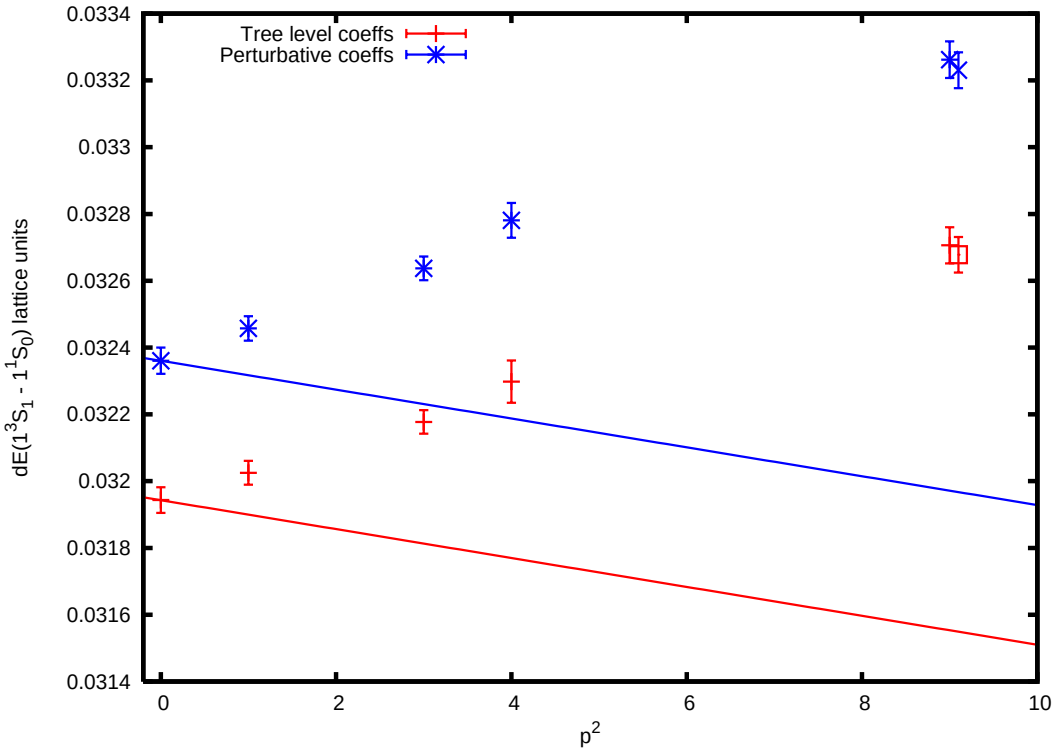

Figure 5.15: Hyperfine splitting $\Upsilon - \eta_b$ on the 010/050 ensemble. The line indicates the function given in 5.8, using M_{η_b} at (1,0,0). The open-box is the tree-level (2,2,1) data point, and the cross is the perturbative (2,2,1).

We take this to indicate errors in the spin-dependent terms of the action, and can attempt to correct it by adding in the lattice version of the term $\frac{g}{8M^3}\psi^\dagger\{\mathbf{D}^2, \boldsymbol{\sigma}\cdot\mathbf{B}\}\psi$ in equation 3.17 to the NRQCD action, with some coefficient c_7. As mentioned in section 3.2.2, the action typically only includes terms up to $\mathcal{O}(v^2)$ relative to leading order. As there are no spin-dependant terms at leading order, which means that spin-dependent quantities such as the hyperfine splitting will be suppressed by an extra factor of v^2. We should therefore carry spin-dependent terms through to $\mathcal{O}(v^4)$ relative to leading order.

	tree-level		perturbative	
p^2	$dE(\Upsilon - \eta_b)$	$a_0(^3S_1)/a_0(^1S_0)$	$dE(\Upsilon - \eta_b)$	$a_0(^3S_1)/a_0(^1S_0)$
0	0.031944(38)	0.90031(48)	0.032361(39)	0.89844(49)
1	0.032025(36)	0.89993(42)	0.032457(37)	0.89806(43)
3	0.032177(35)	0.89911(32)	0.032637(36)	0.89721(32)
4	0.032298(64)	0.89941(85)	0.032781(52)	0.89753(66)
$9\vert_{(3,0,0)}$	0.032706(54)	0.89692(50)	0.033262(55)	0.89505(50)
$9\vert_{(2,2,1)}$	0.032678(53)	0.89734(47)	0.033231(54)	0.89547(47)

Table 5.8: Hyperfine splittings and ratios of amplitudes ($\Upsilon(1S)$ and $\eta_b(1S)$ in the local smearing), simulated on the coarse 010/050 ensemble.

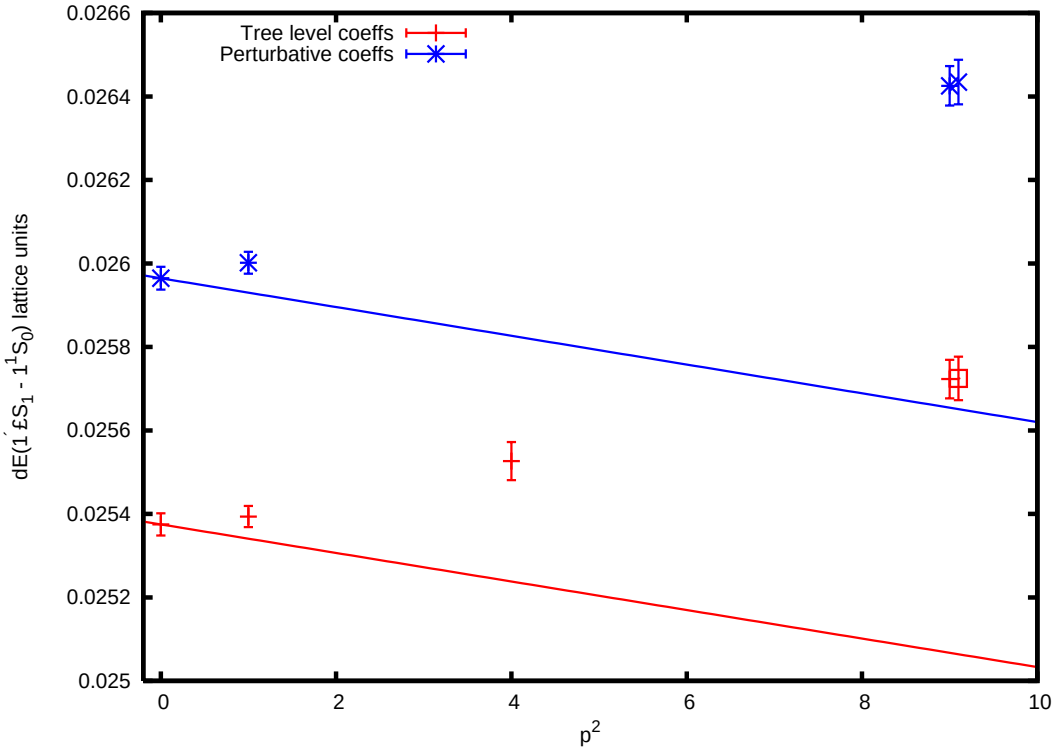

Figure 5.16: Hyperfine splitting $\Upsilon - \eta_b$ on the 0062/031 ensemble. The line indicates the function given in 5.8, using M_{η_b} at (1,0,0). The open-box is the tree-level (2,2,1) data point, and the cross is the perturbative (2,2,1).

	tree-level		perturbative	
p^2	$dE(\Upsilon - \eta_b)$	$a_0(^3S_1)/a_0(^1S_0)$	$dE(\Upsilon - \eta_b)$	$a_0(^3S_1)/a_0(^1S_0)$
0	0.025375(27)	0.83390(31)	0.025965(27)	0.82892(32)
1	0.025394(25)	0.83343(30)	0.026002(26)	0.82852(31)
4	0.025526(46)	0.83279(58)	N/A	N/A
$9\vert_{(3,0,0)}$	0.025723(46)	0.83185(51)	0.026426(47)	0.82655(52)
$9\vert_{(2,2,1)}$	0.025724(52)	0.83208(57)	0.026435(53)	0.82690(58)

Table 5.9: Hyperfine splittings and ratios of amplitudes ($\Upsilon(1S)$ and $\eta_b(1S)$ in the local smearing), simulated on the fine 0062/031 ensemble.

With the exception of the term given here, the terms at this order are redundant or have small coefficients, therefore $\frac{g}{8M^3}\psi^\dagger\{\mathbf{D}^2, \boldsymbol{\sigma}\cdot\mathbf{B}\}\psi$ is the only term we include at this order [66, 67]. The addition of this term should allow us to better model the spin-dependent behaviour manifest both the hyperfine splitting and the differences in Υ and η_b kinetic masses.

We start with a slight aside: to investigate the importance of $\mathbf{B}$ terms, we start by simulating on the 010 "coarse" ensemble without any $\mathbf{B}$ term at all. We then add the $\mathbf{B}$ term, but without tadpole improvement. We compare these to the full action in plot 5.17, which demonstrates that the $\mathbf{B}$ term is the most significant of the spin-dependent terms in the NRQCD action. We also show the kinetic masses of the no $\mathbf{B}$ term case compared to the full action in 5.18.

Having verified the effect of the pre-existing $\mathbf{B}$ term, simulations including the extra term (c_7) were carried out at momenta $p^2 = 0$ and $p^2 = 3$, with the coefficient c_7 set to 1 and 1.5, which is plotted in figure 5.19. As we tune the value of c_7 up, we find a small decrease in the direct hyperfine splittings (both at zero and finite momentum), accompanied by a large increase in the difference in Υ and η_b kinetic masses, until the two measurements are almost equal. This is a valid method of tuning this term, and we can infer that the correct value is close to 1.5. We would, however, have to then retune c_4, which we have made no attempt at here. The figure also includes the experimental result from BaBar [35] for reference, however we do not expect a match with this result -

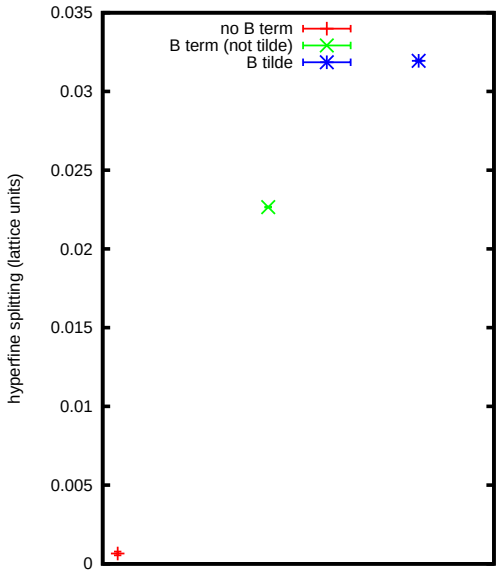

Figure 5.17: Spin dependent hyperfine splittings calculated at zero momentum on the 010/050 ensemble.

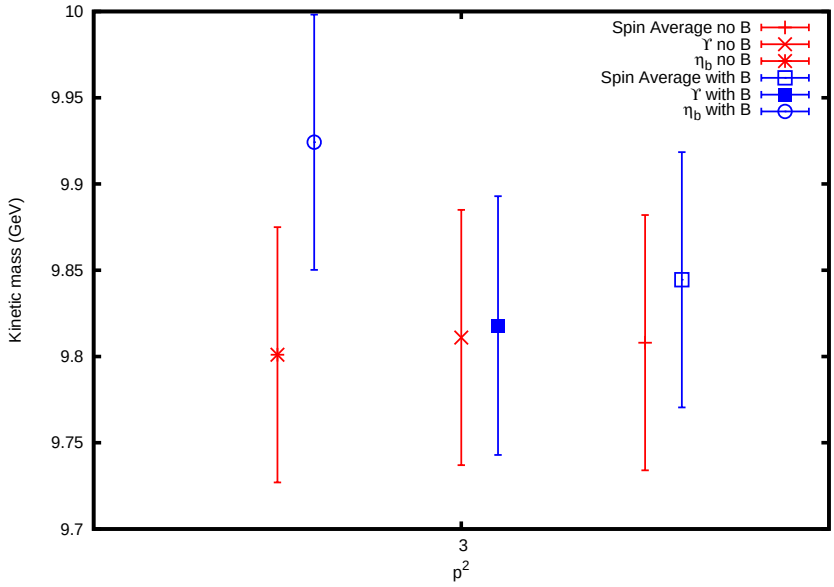

Figure 5.18: Kinetic masses from (1,1,1) on the 010/050 ensemble with and without the **B** term.

the data present here is from a single coarse lattice spacing; furthermore, we would need to retune c_4 (as mentioned) and the bare quark mass before attempting physics runs.

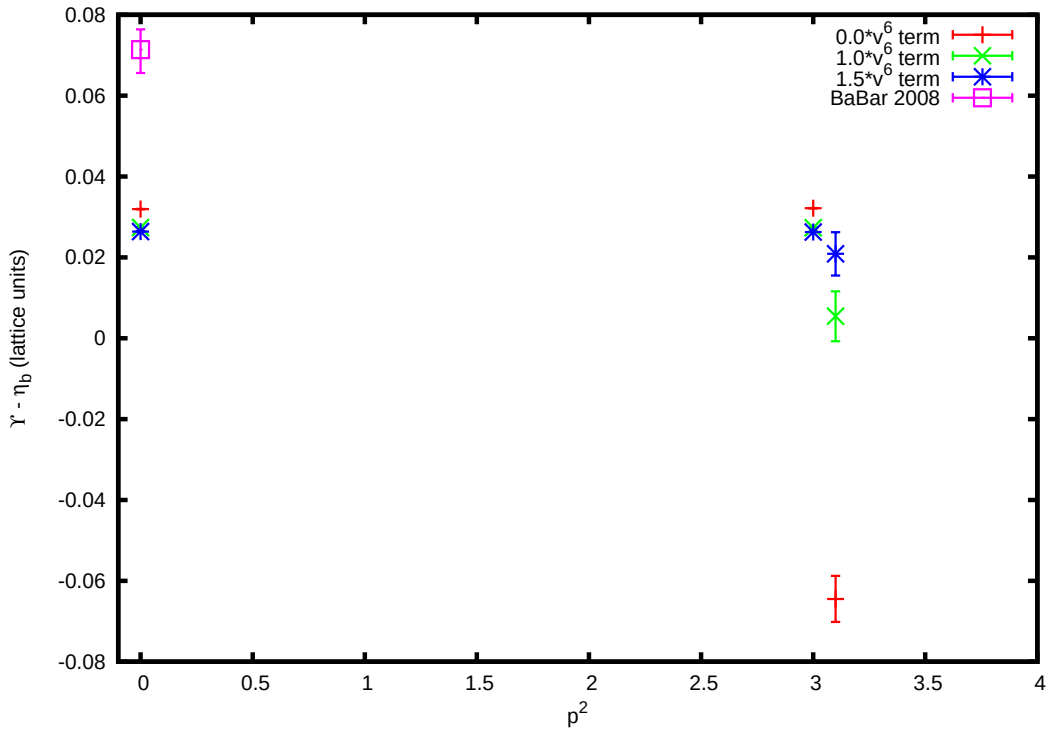

Figure 5.19: Hyperfine splittings, calculated on the 010/050 ensemble. The off-set points at $p^2 = 3$ are the differences between the Υ and η_b kinetic masses. For reference, the BaBar observation [35] has been included (rescaled to lattice units for this ensemble).

5.4 Amplitude Plots

As another check of our dispersion relation, we plot the ratios of the amplitudes of energies in the local smearing. In figures 5.20, 5.21 and 5.22 this is the ratio of the ground-state at finite momentum to the zero-momentum case. Lorentz contraction will decrease the width of the finite momentum state, therefore the amplitude must increase by the square root of the Lorentz factor to conserve probability, thus:

$$\frac{a_0(p)}{a_0(0)} \approx \frac{\sqrt{\gamma}a_0(0)}{a_0(0)} \approx \sqrt{1+\frac{v^2}{2}} \approx \sqrt{1+\frac{p^2}{2M^2}} \approx 1+\frac{p^2}{4M^2}, \tag{5.10}$$

where the p terms must pick up a factor of $2\pi/L$, and L is the spatial length of the lattice. M is the kinetic mass, and we take it from $p = (1,1,1)$ where we have data, and $p = (1,0,0)$ otherwise, using the tree level coefficients. The difference in taking it it from a different momentum, or from the perturbative coefficients is negligible. While each plot deviates from the expected result, and more so for the perturbative coefficients than the tree level, it is clear from these plots that the degree of deviation decreases from the coarsest to finest plots. We would therefore expect this effect to disappear in the continuum limit.

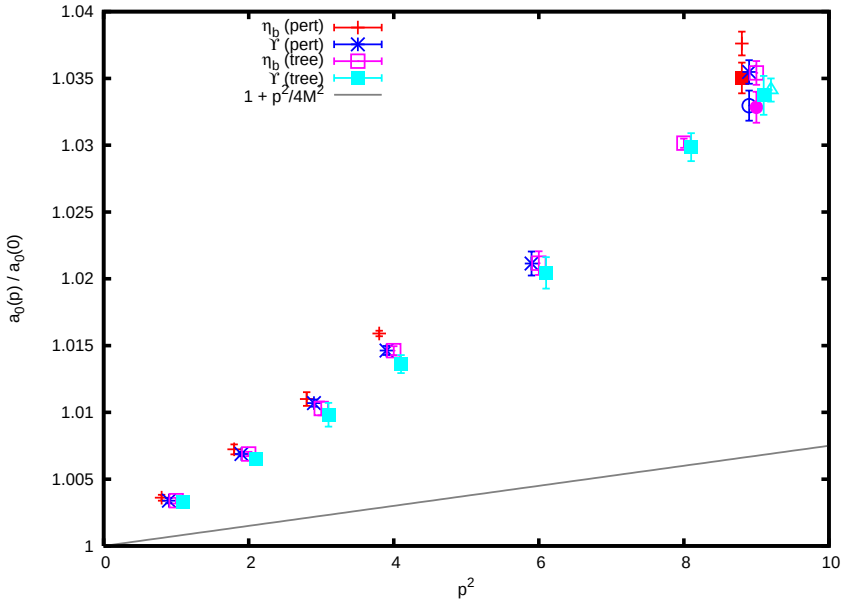

Figure 5.20: Very coarse KM amplitudes. In each case, the (2,2,1) uses a different symbol (same colour) from the rest of its data series. With the exception of the tree-level Υ (open-triangle), these points are all immediately below the (3,0,0) point from the same series. The trend line is the expected ratios, as given be the formula in equation 5.10.

We also plot the local amplitude ratios for the ground state Υ to the ground state η_b, which can be found in figures 5.23, 5.24 and 5.25.

All of these amplitude ratios could be improved upon by adding current corrections, which we investigate in chapter 6.

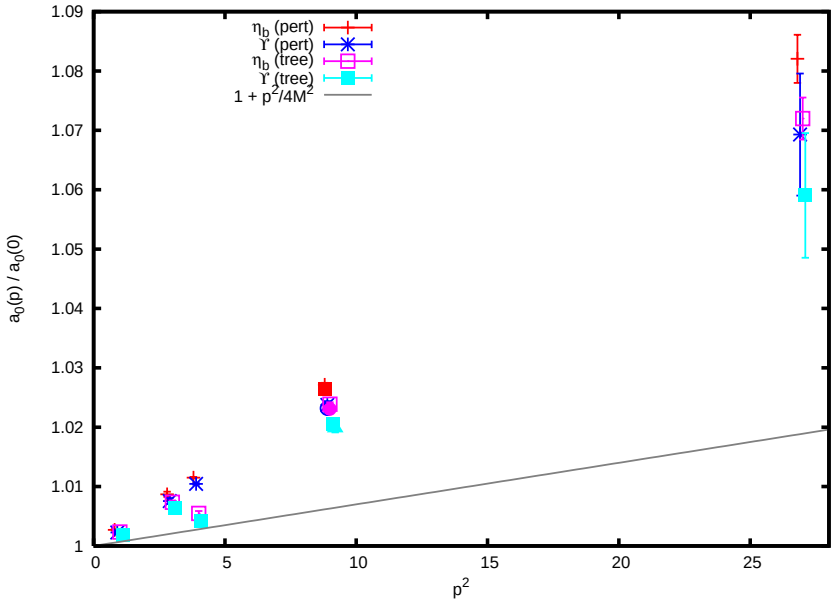

Figure 5.21: Coarse KM amplitudes. The trend line is the expected ratios, as given be the formula in equation 5.10.

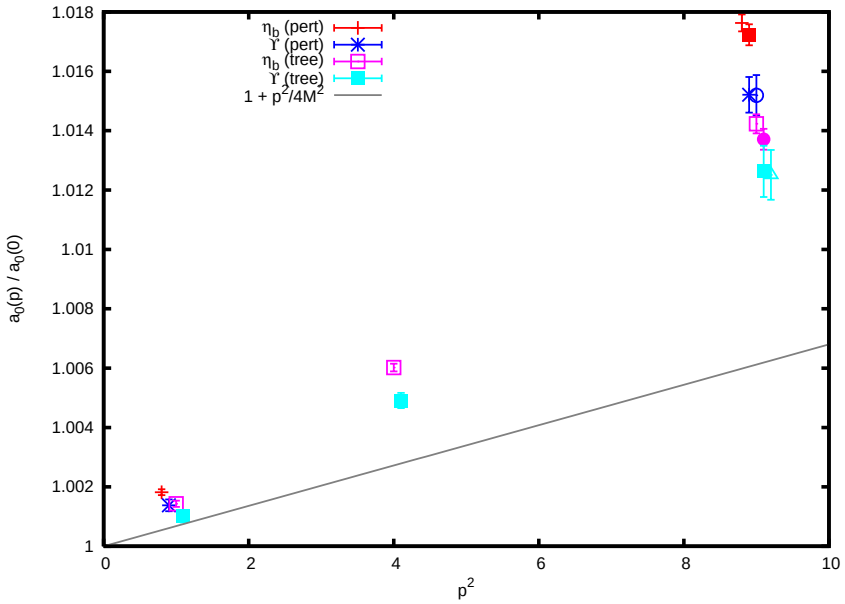

Figure 5.22: Fine KM amplitudes. In each case, the (2,2,1) uses a different symbol (same colour) from the rest of the data series to which it belongs (and is in close proximity to the related (3,0,0) point). The trend line is the expected ratios, as given be the formula in equation 5.10.

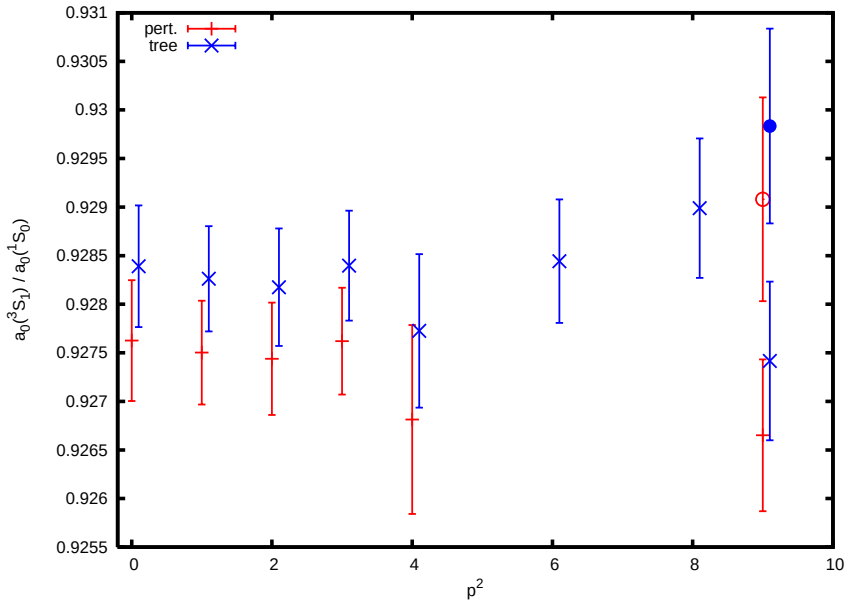

Figure 5.23: Very coarse Hyperfine amplitudes. The closed-circle is the (2,2,1) point for the tree-level data, the open-circle is the (2,2,1) point for the perturbative data.

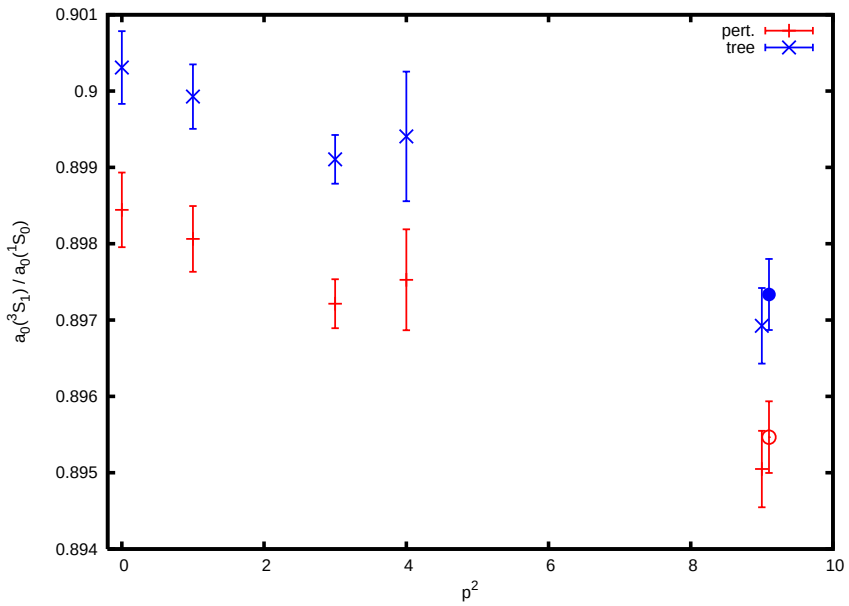

Figure 5.24: Coarse Hyperfine amplitudes. The closed-circle is the (2,2,1) point for the tree-level data, the open-circle is the (2,2,1) point for the perturbative data.

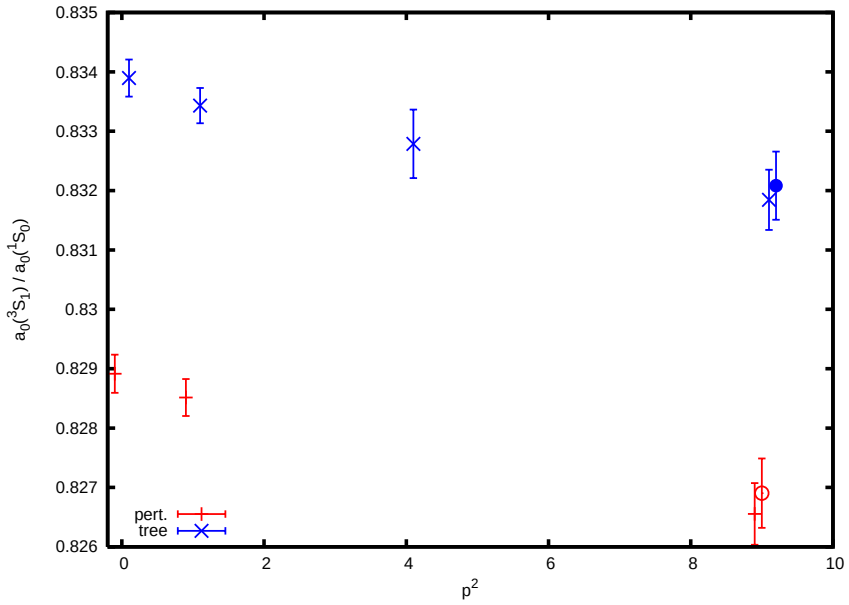

Figure 5.25: Fine Hyperfine amplitudes. The closed-circle is the (2,2,1) point for the tree-level data, the open-circle is the (2,2,1) point for the perturbative data.

5.5 Dispersion Relation Conclusions

With the random wall techniques developed in this thesis, we can now resolve minor discrepancies in the NRQCD dispersion relation. While we can attempt to correct some of these issues, the ultimate arbiter of success is the effect we see in the continuum limit. Drawing from the data presented throughout this chapter, figure 5.26 presents the mismatch between the $p = (3, 0, 0)$ and $p = (2, 2, 1)$ kinetic masses in physical units as a function of a^4. This appears to show a linear dependency, heading to the origin; which would be consistent with higher order effects that will vanish in a continuum extrapolation.

The issue with the hyperfine splitting, however is not so easily dismissed. Again drawing from the data presented earlier in this chapter, we plot the differences in Υ and η_b kinetic masses in physical units as a function of a^2, where the negative values indicate that the η_b has a greater mass than the Υ. On the basis of this plot, one would not expect the hyperfine splitting to reach a positive value in the continuum limit, and certainly not reach one of the magnitude we would expect from the direct fits to the spin-dependent

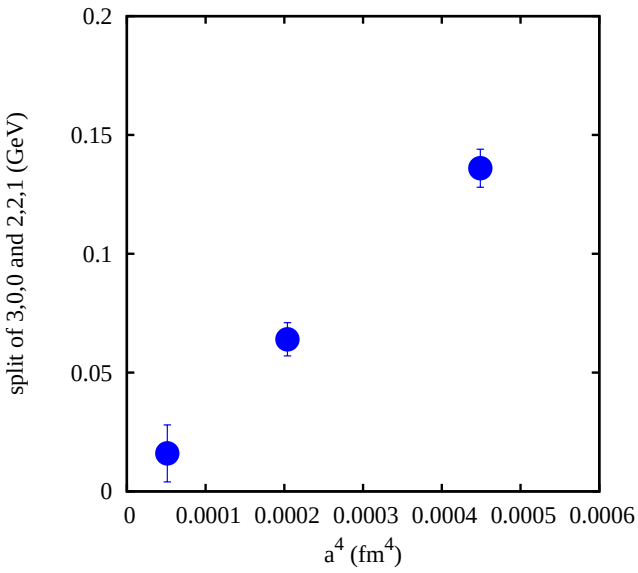

Figure 5.26: The (3,0,0)-(2,2,1) splitting, converted in to physical units, as a function of a^4.

splitting.

We conclude, therefore that in future simulations, it is preferable to use the perturbatively tuned coefficients. Kinetic masses should be tuned using the spin averaged mesons, and not the Υ or η_b. This will avoid mistunings based on the anomalous kinetic mass splitting. Future simulations may also wish to include the additional term $\frac{g}{8M^3}\psi^\dagger\{\mathbf{D}^2, \boldsymbol{\sigma}\cdot\mathbf{B}\}\psi$, added in figure 5.19, with an appropriately tuned coefficient.

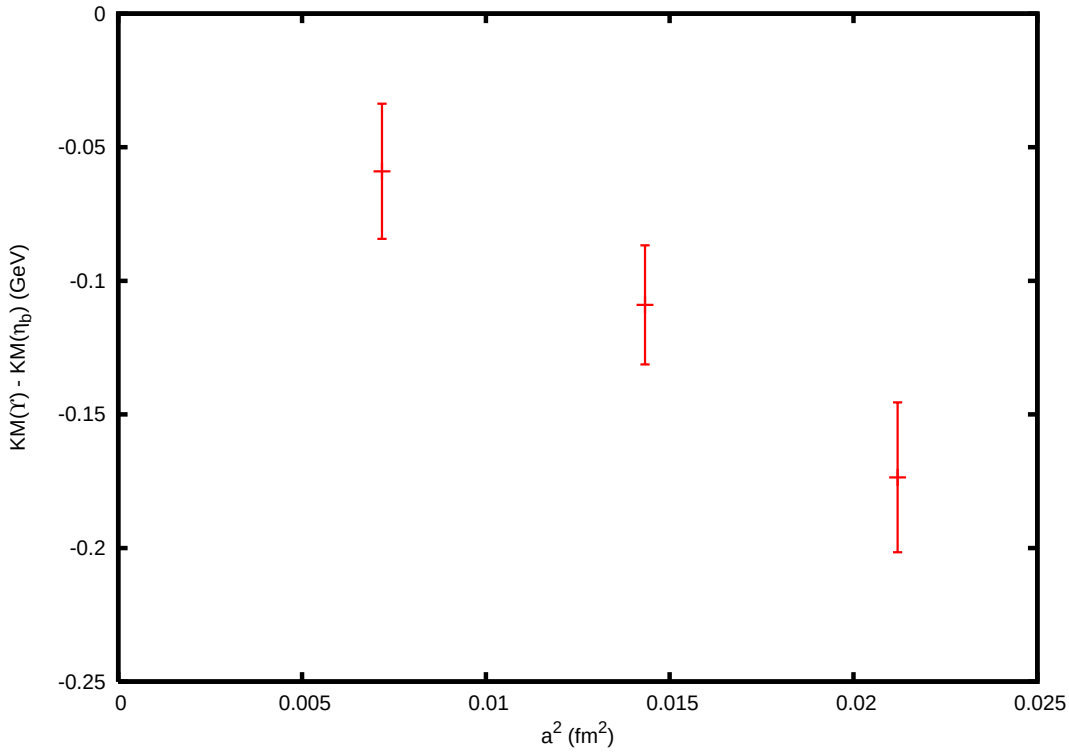

Figure 5.27: The hyperfine splitting as calculated from the differences is Υ and η_b kinetic masses, converted in to physical units, as a function of a^2. This data does not include the $\frac{g}{8M^3}\psi^\dagger\{\mathbf{D}^2, \boldsymbol{\sigma}\cdot\mathbf{B}\}\psi$ correction term.

Chapter 6

Current Corrections and the Υ Leptonic Width

The leptonic width of the Υ to two leptons, Γ_{ee}, is given by the matrix element of the $b\overline{b}$ vector current between the Υ and the vacuum:

$$\Gamma_{ee}(nS) = 16\pi\alpha_{em}^2 e_b^2 \frac{\langle \Upsilon_n | J_v | 0 \rangle}{6M_{\Upsilon(nS)}^2} (Z_{\text{match}})^2 \tag{6.1}$$

in which α_{em} is the electromagnetic coupling constant, e_b is the electric charge, in units of electron charge, of the b quark and $M_{\Upsilon(nS)}$ is the mass of the nth radial excitation of the Υ meson. The factor Z_{match} is a renormalisation constant, and it is required in order to match the lattice current to a renormalisation scheme in the continuum. Calculation of Z_{match} can be done perturbatively.

We can calculate the matrix element on the lattice, and thereby calculate the Υ leptonic width. Before we attempt this, however, we shall make a brief aside in light of the previous chapter.

6.1 Simulation Parameters

From chapters 4and 5, we can conclude that using the Υ to tune the bare quark mass is not optimal due to the ambiguity seen in chapter 5's kinetic masses, and that it is preferable to use the perturbative values for c_i in the NRQCD action. Rather than using the Υ as a reference point for the bare quark mass, we now instead use the spin-average Υ and η_b:

$$M_{\text{spin-avg}} = \frac{3M_\Upsilon + M_{\eta_b}}{4}. \tag{6.2}$$

Since we wish to now simulate with different values of c_i from before, a retuning of the bare quark masses would be necessary, and so we take this opportunity to tune with the perturbative c_i in the action.

We use the existing kinetic masses from chapter 5 that already use the perturbative coefficients, but still use the original bare quark masses, to make an approximate calculation of what we believe the new bare quark mass to be. This approximation simply assumes that all discrepancy between the simulation value of the spin-averaged kinetic mass and that of experiment comes from an error in the bare quark mass. We take the experimental value of the spin averaged $b\overline{b}$ to be 9.445 GeV.

The value of the bare quark mass extrapolated by this method is then confirmed with a kinetic mass simulation at $p^2 = 0$ and $p^2 = 3$, and retuned if necessary. The change from using $p^2 = 2$ to $p^2 = 3$ is again motivated by chapter 5, in particular figure 5.1 and related plots, in which the "on-axis" momenta are less consistent with the rest of the simulation data.

With new bare b quark masses for the lattice we are using, we can now proceed to the examination of the leptonic width of the Υ. We run a lattice simulation calculating propagators for the local and excited state quark smearings (with local smearings on the anti-quark):

$$\phi^q_{local}(x) = \delta(x), \tag{6.3}$$

$$\phi^q_{1S}(x) = (2a_0 - |x|)\, e^{(-0.5|x|/a_0)} \tag{6.4}$$

Ensemble	Previous aM_b	Resulting KM	New aM_b	Final KM
0097/0484	3.4	9.789(77) GeV	3.28	9.467(61) GeV
010/050	2.8	9.903(75) GeV	2.66	9.435(74) GeV
0062/031	1.95	10.058(78) GeV	1.818	9.468(58) GeV

Table 6.1: Spin-averaged kinetic masses calculated using perturbative c_i, first using the same bare quark mass as used for tree-level c_i, then using retuned bare-quark masses extrapolated by comparing the previous kinetic mass with the experimental value of 9.445. With the exception of the 0062/031 ensemble, all kinetic masses were calculated at $p^2 = 3$. For the 0062/031, the final mass is from $p^2 = 3$, but the preceding kinetic mass is taken at $p^2 = 1$ since no existing $p^2 = 3$ data existed for this ensemble with these coefficients; since this mass is only used to aid in tuning the final bare quark mass, this distinction is unimportant as long as the final kinetic mass is correct.

using the perturbative coefficients of described in chapter 5 and these new bare quark masses.

6.2 Simulation Results and the Leading Order Leptonic Width

We perform 2×2 Bayesian fits to the simulation data generated following the end of the previous section, using the same fitting priors as in chapter 4, table 4.7. Since we have changed many of the simulation parameters, we do not expect exact agreement with chapter 4.

From these results, we calculate the leading order ratio of the leptonic widths

$$\frac{\Upsilon(2S)M^2_{\Upsilon(2S)}}{\Upsilon(1S)M^2_{\Upsilon(1S)}}.$$

This is exceptionally simple, as the result is merely the ratio (squared) of two amplitudes

from the Bayesian fit; specifically the amplitudes of the local smearing in the first excited state and the ground state, known as the wave-function at the origin $a^{3/2}|\Psi_n(0)|$.

$$\frac{\Gamma_{ee}(2S)M^2_{\Upsilon(2S)}}{\Gamma_{ee}(1S)M^2_{\Upsilon(1S)}} = \frac{|\Psi_2(0)|^2}{|\Psi_1(0)|^2} \tag{6.5}$$

The advantage of this is that, as a ratio, the majority of factors from equation 6.1 cancel, in particular Z_{match}, allowing for straightforward comparison with experiment (for example [68, 1]).

Ensemble	E_0	$E_1 - E_0$	$E_2 - E_0$	a_0(local)	a_1(local)	$\frac{\lvert\Psi_2(0)\rvert^2}{\lvert\Psi_1(0)\rvert^2}$
0097/0484	0.302004(39)	0.4194(62)	0.710(27)	0.38747(11)	0.3074(85)	0.629(35)
010/050	0.312530(60)	0.3410(49)	0.535(45)	0.29411(13)	0.2280(73)	0.601(38)
0062/031	0.305234(31)	0.2449(14)	0.442(27)	0.171288(45)	0.1347(10)	0.598(39)

Table 6.2: The amplitudes of the ground and first excited states in the local smearing, and the square of their ratio, which gives $\frac{\Gamma_{ee}(2S)M^2_{\Upsilon(2S)}}{\Gamma_{ee}(1S)M^2_{\Upsilon(1S)}}$ as in equation 6.5

We assume that there is no dependence on the light quark mass (see, for example, [4]), but that there is a dependence on a^2. A plot of these ratios against a^2 is presented later in this chapter, in figure 6.2, along with the current experimental result.

6.3 Current Corrections to the Leptonic Width

So far, we have only calculated the ratio of leptonic widths for the Υ and Υ', and it is only the absence of Z_{match} that has prevented us from calculating the widths explicitly. In this section, we shall attempt to use perturbative results and our lattice data to make this explicit calculation.

There are higher order current corrections to the true QCD matrix element that describes the leptonic width, which may in principle be calculated on the lattice. Following

[6], we choose these currents to be

$$\mathbf{J}_i = \boldsymbol{\sigma} \left(\frac{\Delta^2}{M^2} \right)^i, \tag{6.6}$$

in which M is the bare b-quark mass. The QCD value is then related to these currents as

$$\left\langle 0|\mathbf{J}^{QCD}|\overline{Q}Q\right\rangle = \sum_i k_i \left\langle 0|\mathbf{J}_i|\overline{Q}Q\right\rangle, \tag{6.7}$$

where k_i are matching coefficients (which takes account of Z_{match}, which are expanded as a power series in α_s:

$$k_i = \sum_n \alpha_s^n k_i^{(n)}. \tag{6.8}$$

The (n) denotes the order in α_s to which the coefficient $k_i^{(n)}$ contributes. These have been calculated in [6], and for convenience the $k_i^{(n)}$ used in this work are tabulated in table 6.3. It should be noted that the coefficients from [6] are calculated at a different stability parameter n and bare quark mass than we are using (we use $n = 4$, rather than 2, and we have updated the quark masses having changed coefficients in the action). We disregard these issues for the coarse and fine ensembles, for which the masses in this work are close to those in the reference. For the very coarse, we disregard n, but we attempt to linearly interpolate to a slightly lower mass. Interpolating between $aM_b = 2.8$ and $aM_b = 4.0$, we get $k_0^{(0)} = -0.1554$ and $k_1^{(1)} = -2.15$.

To $\mathcal{O}(\alpha_s)$, the QCD current is calculated as:

$$\begin{aligned} J^{QCD} &= J_0 + \alpha_s k_0^{(1)} J_0 \\ &+ \frac{1}{6} J_1 + \alpha_s k_1^{(1)} J_1 \end{aligned} \tag{6.9}$$

The current J_0 is just the amplitude of the meson state in the local smearing (as in section 6.1), and we can calculate J_1 by calculating the smearing functions described in section 6.1, plus the operator in equation 6.6 with $i = 1$ applied to each such smearing, and extending our Bayesian fit to a 3×2 matrix. Using equations 6.1 and 6.9 with $\alpha_{em} = 1/132$ and $\alpha_s = \alpha_V(\frac{1.8}{a})$, we calculate the leptonic widths of the Υ and Υ'. Fit results and values of the width Γ_{ee} are given in table 6.4.

aM	n	$k_0^{(1)}$	$k_1^{(1)}$
1.95	2	-0.1358(16)	-0.16(16)
2.8	2	-0.1732(16)	-1.35(22)
4.0	2	-0.1288(27)	-3.32(29)
3.28*	-	-0.1554	-2.15
$k_0^{(0)} = 1$		$k_1^{(0)} = 1/6$	

Table 6.3: Coefficients for the α_s expansion of the matrix element J^{QCD} in terms of the NRQCD currents given in equation 6.6. These are taken from [6], where they are denoted $a_i^{(n)}$ (we use the symbol k instead because we reserve the symbol a for lattice spacings). * interpolated from $aM = 2.8$ and $aM = 4.0$.

	Υ			Υ'		
Ensemble	J_0	J_1	Γ_{ee} (keV)	J_0	J_1	Γ_{ee} (keV)
0097/0484	0.38750(12)	-0.074306(60)	1.518(61)	0.3089(85)	-0.0947(33)	0.9822(74)
010/050	0.294190(90)	-0.068700(40)	1.411(48)	0.2263(72)	-0.0813(30)	0.7955(61)
0062/031	0.171064(55)	-0.051156(27)	1.137(33)	0.1325(25)	-0.0590(11)	0.5844(34)

Table 6.4: The NRQCD currents for the Υ ground state and first excited state (Υ').

In figure 6.1, we plot the leptonic widths calculated here as function of a^2. It is clear that they would extrapolate to a value too low to be consistent with the experimental values included in the figure. This is not entirely surprising, as this is only $\mathcal{O}(\alpha_s)$, and $\mathcal{O}(\alpha_s^2)$ may be up to $\sim 10\%$. We must also consider that the coefficients we have used from perturbation theory are used in the absence of coefficients that match our values of aM_b and n.

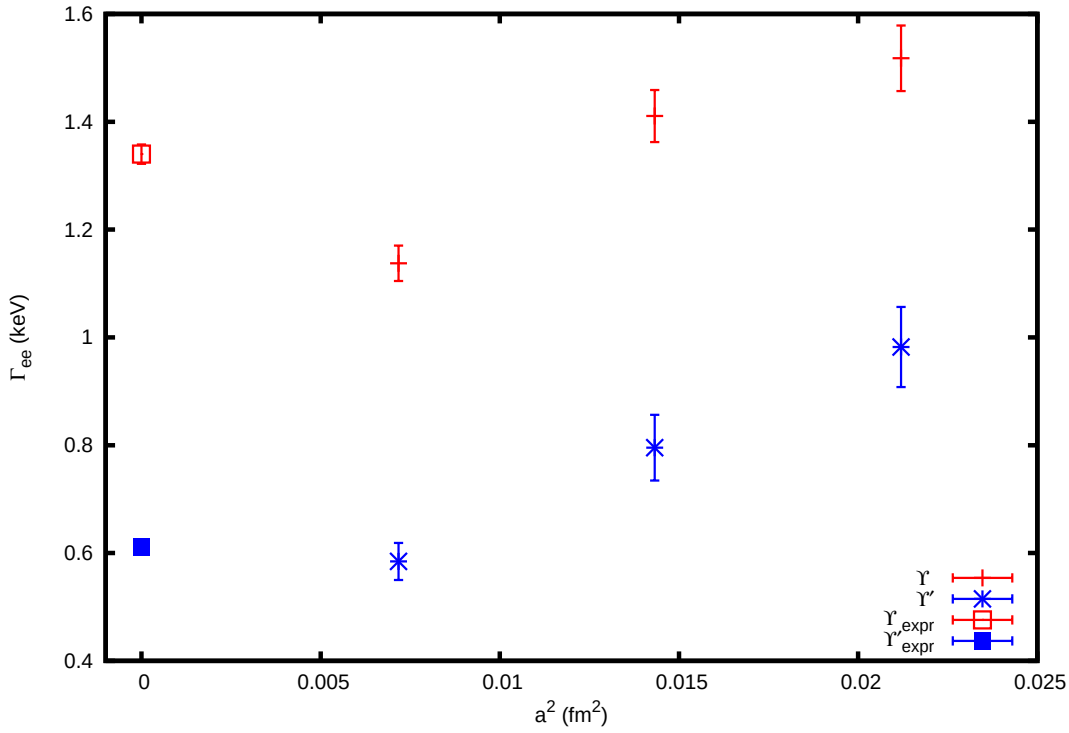

Figure 6.1: The leptonic with Γ_{ee} of the Υ (dashes) and Υ' (bursts) in keV. The open and closed boxes represent the respective experimental values [1].

The correction currents J_1 contains a portion that looks like J_0, and may be a large fraction of the current J_0. To demonstrate, we plot the ratio J_1/J_0 for each lattice in figure 6.3. The figure shows that the J_1 currents are indeed a significant fraction of the currents J_0, and the magnitude grows as lattice spacing decreases. However, one must also be aware that at higher loop orders, J_1 will contribute at lower orders of v^2 than would otherwise be expected; called "mixing downward" in [6]. It is therefore better to define subtracted currents $\overline{J}_i \equiv z_{ij} J_j$ that ensure each current contributes only at its own

order or higher. $z_{ij}^{(0)} = \delta_{ij}$ and $z_{ij}^{(n>0)} = 0$ for all $j \geq i$ (because it is only necessary to prevent mixing downwards, not upwards), therefore for $\mathcal{O}(v^2)$:

$$\overline{J}_1 = J_1 + z_{10} J_0 = J_1 + z_{10}^{(1)} \alpha_s J_0,$$

and the ratio J_1/J_0 becomes $\overline{J_1}/J_0 = J_1/J_0 + z_{10}^{(1)}\alpha_s$. This can also be seen in table 6.5 and plot 6.3.

		Υ		Υ'	
Ensemble	$z_{10}^{(1)}$	J_1/J_0	$\overline{J}_1/J_0$	J_1/J_0	$\overline{J}_1/J_0$
0097/0484	0.14400(9)*	-0.19176(17)	-0.13762(17)	-0.307(14)	-0.252(14)
010/050	0.16171(8)	-0.23352(15)	-0.18064(15)	-0.359(18)	-0.306(18)
0062/031	0.22289(11)	-0.29905(18)	-0.23887(18)	-0.445(12)	-0.385(12)

Table 6.5: The ratios J_1/J_0 and $\overline{J}_1/J_0$. The perturbative parameter $z_{10}^{(1)}$ is from [6], with the exception of * which was interpolated from $z_{10}^{(1)}(aM = 2.8) = 0.16171(8)$ and $z_{10}^{(1)}(aM = 4.0) = 0.11743(5)$

.

The fact that these subtracted corrections are still large presents a challenge in calculating the leptonic width in this way - with corrections being so large, we would ideally want to go to higher order if we are to expect good agreement with experiment. With this in mind, we would hope that $\overline{J}_2/J_0$ presents a much smaller ratio that J_1. In figure 6.4, we plot the ratio J_2/J_0 (but not $\overline{J}_2$ as we do not have values for the z_{20} parameters). The values for J_2 are tabulated in 6.6. The magnitude of the ratio is indeed smaller, as expected.

Despite the mismatch with experiment, we can use the current corrected leptonic widths to re-calculate the ratio of leptonic widths times the square of the mass from section 6.2. One would hope that much of the discrepancy, present in both our Υ and Υ' determinations, would cancel in the ratio. For comparison, this ratio is plotted on figure 6.2 along with the tree-level determination and experiment. The current corrected

version gives a more pronounced a^2 dependency, and suggests a slightly lower continuum extrapolation than the tree-level equivalent. With the given errors on both data sets, the results are consistent with experiment as we approach zero lattice spacing.

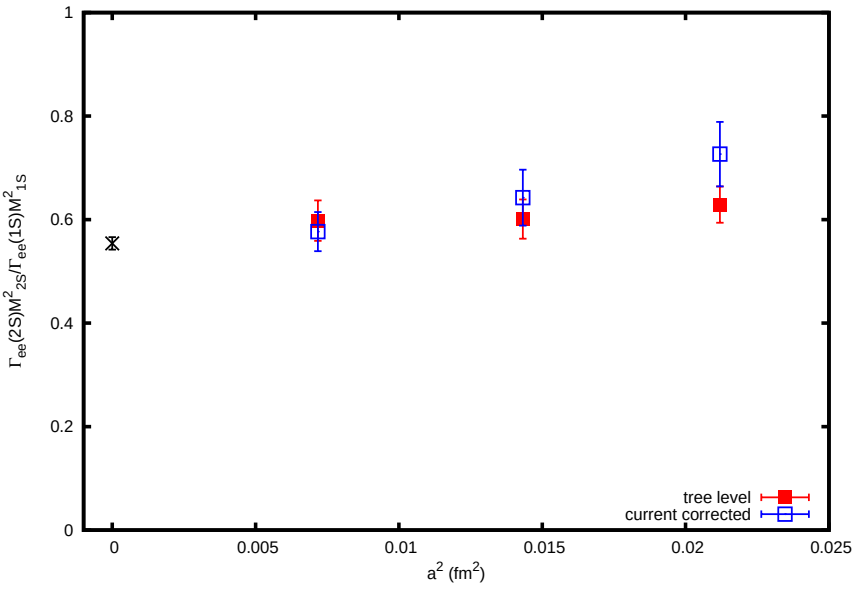

Figure 6.2: The ratio of leptonic width times the mass squared for Υ' and Υ as a function of a^2. The cross is the experimental value, taken from the Particle Data Group [1].

	Υ		Υ'	
Ensemble	J_2	J_2/J_0	J_2	J_2/J_0
0097/0484	0.0125577(7)	0.032457(21)	0.01842(60)	0.0600(25)
010/050	0.015439(10)	0.052497(40)	0.0109(68)	0.0913(26)
0062/031	0.014828(8)	0.086664(45)	0.0208(4)	0.1565(32)

Table 6.6: The values of J_2 and the ratios J_2/J_0 for both Υ and Υ'

.

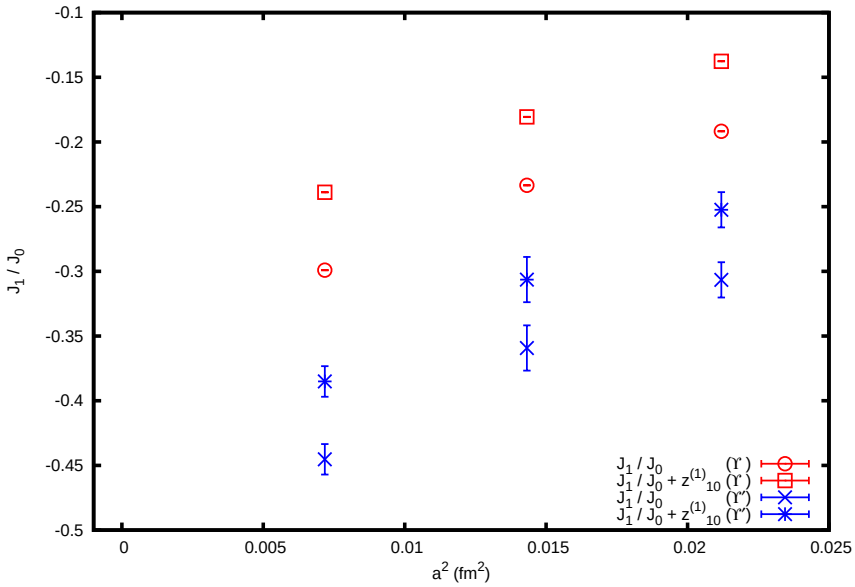

Figure 6.3: The ratio J_1/J_0 for each lattice spacing a^2.

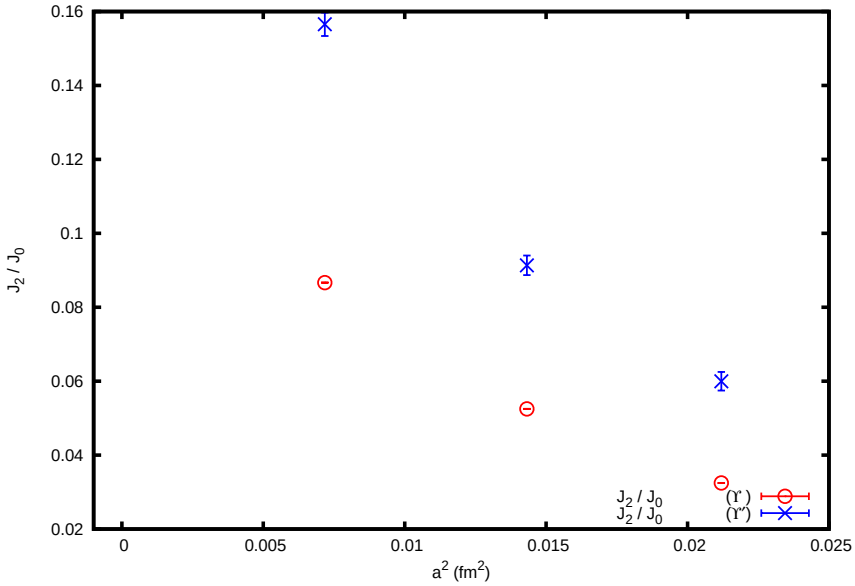

Figure 6.4: The ratio J_2/J_0 for each lattice spacing a^2.

Chapter 7

Conclusion

The development of the random wall algorithm has allowed us to improve the precision of with which we can simulate the b quark on the lattice. By combining the random wall with the already established use of smearing functions, we can perform Υ spectroscopy with greater accuracy than previously. In particular, the random wall has allowed us to produce very accurate b quark propagators from which we can make very precise fits to the ground state energies of the $\Upsilon(1S)$ and $\eta_b(1S)$ mesons.

Using the NRQCD quark action, we tune the b bare quark masses for a variety of MILC ensembles using Bayesian fits to the energy difference between the Υ at zero and non-zero momenta to calculate the kinetic mass, and then match to experiment. We then match the $\Upsilon(2S) - \Upsilon(1S)$ splitting to experiment, and in doing so we can determine the heavy quark potential scale parameter r_1 with $\sim 1\%$ errors. By combining this result with other lattice calculations, the final result gives $r_1 = 0.3133(23)(3)$fm. We were able to reproduce the bottomonium spectrum in agreement with experiment.

In addition to Υ spectroscopy, the lattice can be used to determine the strong coupling constant α_s. We calculate Wilson loops on the MILC ensembles we have been studying, and compare this non-perturbatively determined value to a third order perturbative expansion. A necessary input in to this calculation is knowledge of the lattice spacings used,

and we use our value of r_1 to obtain this. The final result gives $\alpha_{\overline{MS}} = 0.1183(8)$.

The very accurate b propagators produced with NRQCD using a random wall can also be used in other simulations, and have been important in studying the B_c meson in combination with c HISQ quarks.

We then investigate the NRQCD dispersion relation, with a view to improvement. At the error levels we can achieve with the random wall technique, we can now resolve the discrepancy between the two $p^2 = 9$ states as a several standard deviation effect. We can decrease or even remove this effect by modifying the NRQCD coefficients beyond tree level, either via non-perturbative tuning or by simulating using coefficients calculated through perturbation theory [65]. We also see an issue with the splitting between the Υ and η_b kinetic masses, which has the wrong sign relative to both a direct lattice determination of the spin-dependent splitting and experiment. We have shown that this can be resolved by the addition of an extra higher order term to the NRQCD action. Future simulations incorporating this additional term (see, for example, [30]) and perturbative coefficients may provide a more consistent and accurate picture of the Υ spectrum. We also conclude that bare quark masses can be better tuned by using spin-averaged mesons, which are not affected by problems in the spin-dependent spectrum.

Amplitudes from fits to Υ simulations using the perturbative coefficients and retuned bare quark masses suggested by our investigation of the dispersion relation provided the wave-function at the origin. The wave-functions can be used to give the leading order in v^2 ratio of the leptonic width of the Υ ground state, and the excited state Υ', where the perturbative matching factors cancel in the ratio, allowing for comparison with experiment.

We then followed a perturbative matching procedure to match NRQCD currents to the continuum, including a higher order current J_1. We compare the leptonic widths calculated with this procedure to experiment, and find a mismatch. This is likely due to the magnitude of the corrections made, and a discrepancy between the parameters of the

action used in the original perturbative matching calculation and our lattice simulation. Future works should investigate higher order terms; it is possible that α_s^2 may contribute by as much as $\sim 10\%$. It may also be fruitful to include matching to the higher order current J_2. Further efforts may also utilise other approaches to determine the leptonic width, such as current-current correlators.

Bibliography

[1] **Particle Data Group** Collaboration, C. Amsler *et al.*, "Review of particle physics," *Phys. Lett.* **B667** (2008) 1.

[2] G. P. Lepage, L. Magnea, C. Nakhleh, U. Magnea, and K. Hornbostel, "Improved nonrelativistic QCD for heavy quark physics," *Phys. Rev.* **D46** (1992) 4052–4067, arXiv:hep-lat/9205007.

[3] A. Bazavov *et al.*, "Full nonperturbative QCD simulations with 2+1 flavors of improved staggered quarks," *Rev. Mod. Phys.* **82** (2010) 1349–1417, arXiv:0903.3598 [hep-lat].

[4] A. Gray *et al.*, "The Upsilon spectrum and m(b) from full lattice QCD," *Phys. Rev.* **D72** (2005) 094507, arXiv:hep-lat/0507013.

[5] Q. J. Mason, "High precision lattice QCD: Perturbations in a non-perturbative world.". UMI-31-14569.

[6] A. Hart, G. M. von Hippel, and R. R. Horgan, "Leptonic widths of heavy quarkonia: S-Wave QCD/NRQCD matching coefficients for the electromagnetic vector annihilation current at $O(\alpha_s v^2)$," *Phys. Rev.* **D75** (2007) 014008, arXiv:hep-lat/0605007.

[7] I. Montvay and G. Munster, "Quantum fields on a lattice,". Cambridge University Press (1994) 491 p.

[8] K. G. Wilson, "Quarks and Strings on a Lattice,". New phenomena In Subnuclear Physics. Part A. Proceedings the First Half of the 1975 International School of Subnuclear Physics, Erice, Sicily, July 11 - August 1, 1975, ed. A. Zichichi, Plenum Press, New York 1977, p. 69, CLNS-321.

[9] N. Metropolis, A. W. Rosenbluth, M. N. Rosenbluth, A. H. Teller, and E. Teller, "Equations of state calculations by fast computing machines," *J. Chem. Phys.* **21** (1953) 1087–1092.

[10] M. A. Clark, B. Joo, and A. D. Kennedy, "Comparing the R algorithm and RHMC for staggered fermions," *Nulc. Phys. Proc. Suppl.* **119** (2003) 1015–1017, `arXiv:hep-lat/0209035`.

[11] **HPQCD** Collaboration, E. Follana *et al.*, "Highly Improved Staggered Quarks on the Lattice, with Applications to Charm Physics," *Phys. Rev.* **D75** (2007) 054502, `arXiv:hep-lat/0610092`.

[12] H. J. Rothe, "Lattice gauge theories: An Introduction," *World Sci. Lect. Notes Phys.* **59** (1997) 1–512.

[13] M. E. Peskin and D. V. Schroeder, "An Introduction to Quantum Field Theory,". Reading, USA: Addison-Wesley (1995) 842 p.

[14] G. P. Lepage and P. B. Mackenzie, "On the viability of lattice perturbation theory," *Phys. Rev.* **D48** (1993) 2250–2264, `arXiv:hep-lat/9209022`.

[15] C. J. Morningstar, "The Heavy quark selfenergy in nonrelativistic lattice QCD," *Phys. Rev.* **D48** (1993) 2265–2278, `arXiv:hep-lat/9301005`.

[16] H. D. Trottier, "Quarkonium spin structure in lattice NRQCD," *Phys. Rev.* **D55** (1997) 6844–6851, `arXiv:hep-lat/9611026`.

[17] K. Symanzik, "Continuum Limit and Improved Action in Lattice Theories. 1. Principles and phi**4 Theory," *Nucl. Phys.* **B226** (1983) 187.

[18] M. G. Alford, W. Dimm, G. P. Lepage, G. Hockney, and P. B. Mackenzie, "Lattice QCD on small ccomputers," *Phys. Lett.* **B361** (1995) 87–94, arXiv:hep-lat/9507010.

[19] M. Luscher, "Advanced lattice QCD," arXiv:hep-lat/9802029.

[20] J. Kogut and L. Susskind, "Hamiltonian formulation of Wilson's lattice gauge theories," *Phys. Rev.* **D11** (1975) 395.

[21] L. Susskind, "Lattice Fermions," *Phys. Rev.* **D16** (1977) 3031–3039.

[22] G. P. Lepage, "Notes on Naive/Staggered Quarks." Unpublished, 2005.

[23] S. Durr, "Theoretical issues with staggered fermion simulations," *PoS* **LAT2005** (2006) 021, arXiv:hep-lat/0509026.

[24] M. Creutz, "Diseases with rooted staggered quarks," *PoS* **LAT2006** (2006) 208, arXiv:hep-lat/0608020.

[25] C. Bernard, M. Golterman, Y. Shamir, and S. R. Sharpe, "'t Hooft vertices, partial quenching, and rooted staggered QCD," *Phys. Rev.* **D77** (2008) 114504, arXiv:0711.0696 [hep-lat].

[26] D. H. Adams, "The rooting issue for a lattice fermion formulation similar to staggered fermions but without taste mixing," *Phys. Rev.* **D77** (2008) 105024, arXiv:0802.3029 [hep-lat].

[27] G. P. Lepage, "Flavor-symmetry restoration and Symanzik improvement for staggered quarks," *Phys. Rev.* **D59** (1999) 074502, arXiv:hep-lat/9809157.

[28] S. Naik, "On-shell Improved Lattice Action For QCD With Susskind Fermions And Asymptotic Freedom Scale," *Nucl.Phys.* **B316** (1989) 238.

[29] S. Meinel, "The bottomonium spectrum from lattice QCD with 2+1 flavors of domain wall fermions," *Phys. Rev.* **D79** (2009) 094501, arXiv:0903.3224 [hep-lat].

[30] S. Meinel, "Bottomonium spectrum at order v^6 from domain-wall lattice QCD: precise results for hyperfine splittings," arXiv:1007.3966 [hep-lat].

[31] W. R. Innes *et al.*, "Observation of structure in the Υ region," *Phys. Rev. Lett.* **39** (1977) 1240.

[32] F. Pauss *et al.*, "Observation of χ_b production in the exclusive reaction $\Upsilon' \to \gamma\chi_b \to \gamma\gamma\Upsilon \to \gamma\gamma$ (e^+ e^- or μ^+ μ^-)," *Phys. Lett.* **B130** (1983) 439.

[33] G. Eigen *et al.*, "Evidence for χ_b' production in the exclusive reaction $\Upsilon'' \to \gamma\chi_b' \to$ (γ γ Υ' or γ γ Υ)," *Phys. Rev. Lett.* **49** (1982) 1616–1619.

[34] K. Han *et al.*, "Observation of P wave B anti-B bound states," *Phys. Rev. Lett.* **49** (1982) 1612–1616.

[35] **BABAR** Collaboration, "Observation of the bottomonium ground state in the decay Upsilon(3S) —> gamma eta_b," arXiv:0807.1086 [hep-ex].

[36] **BABAR** Collaboration, P. Grenier, "Observation of the bottomonium ground state, η_b, at BaBar," arXiv:0809.1672 [hep-ex].

[37] B. A. Thacker and G. P. Lepage, "Heavy quark bound states in lattice QCD," 1991.

[38] R. Sommer, "Introduction to Non-perturbative Heavy Quark Effective Theory," arXiv:1008.0710 [hep-lat].

[39] A. X. El-Khadra, A. S. Kronfeld, and P. B. Mackenzie, "Massive Fermions in Lattice Gauge Theory," *Phys. Rev.* **D55** (1997) 3933–3957, arXiv:hep-lat/9604004.

[40] M. Wingate, J. Shigemitsu, C. T. H. Davies, G. P. Lepage, and H. D. Trottier, "Heavy-lightmesons with staggered light quarks," *Phys. Rev.* **D67** (2003) 054505, arXiv:hep-lat/0211014.

[41] C. J. Morningstar, "Radiative corrections to the kinetic couplings in nonrelativistic lattice QCD," *Phys. Rev.* **D50** (1994) 5902–5911, arXiv:hep-lat/9406002.

[42] C. T. H. Davies *et al.*, "Precision Upsilon spectroscopy from nonrelativistic lattice QCD," *Phys. Rev.* **D50** (1994) 6963–6977, arXiv:hep-lat/9406017.

[43] F. Mandl and G. Shaw, "Quantum Field Theory, Revised Edition,". Chichester, UK: Wiley (1993) 358 P. (A Wiley-interscience Publication).

[44] G. P. Lepage *et al.*, "Constrained curve fitting," *Nucl. Phys. Proc. Suppl.* **106** (2002) 12–20, arXiv:hep-lat/0110175.

[45] C. W. Bernard *et al.*, "The QCD spectrum with three quark flavors," *Phys. Rev.* **D64** (2001) 054506, arXiv:hep-lat/0104002.

[46] C. Aubin *et al.*, "Light hadrons with improved staggered quarks: Approaching the continuum limit," *Phys. Rev.* **D70** (2004) 094505, arXiv:hep-lat/0402030.

[47] C. T. H. Davies *et al.*, "Fourier Acceleration in lattice gauge theories. 1. Landau gauge fixing," *Phys. Rev.* **D37** (1988) 1581.

[48] A. Gray, "*Upsilon Spectroscopy and Leptonic Decays using Fully Unquenched Lattice QCD*,". PhD thesis, University of Glasgow, 2003.

[49] R. Sommer, "A New way to set the energy scale in lattice gauge theories and its applications to the static force and alpha-s in SU(2) Yang-Mills theory," *Nucl. Phys.* **B411** (1994) 839–854, arXiv:hep-lat/9310022.

[50] C. W. Bernard *et al.*, "The static quark potential in three flavor QCD," *Phys. Rev.* **D62** (2000) 034503, arXiv:hep-lat/002028.

[51] W. H. Press, s. A. Teukolsky, W. T. Vetterling, and B. P. Flannery, "Numerical Recipes in C,". Cambridge University Press (2002) 994 p.

[52] **HPQCD** Collaboration, C. T. H. Davies, E. Follana, I. D. Kendall, G. P. Lepage, and C. McNeile, "Precise determination of the lattice spacing in full lattice QCD," *Phys. Rev.* **D81** (2010) 034506, arXiv:0910.1229.

[53] G. P. Lepage and P. B. Mackenzie, "On the viability of lattice perturbation theory," *Phys. Rev.* **D48** (1993) 2250–2264, arXiv:hep-lat/9209022.

[54] S. J. Brodsky, G. P. Lepage, and P. B. Mackenzie, "On the Elimination of Scale Ambiguities in Perturbative Quantum Chromodynamics," *Phys. Rev.* **D28** (1983) 228.

[55] **HPQCD** Collaboration, Q. Mason *et al.*, "Accurate determinations of alpha(s) from realistic lattice QCD," *Phys. Rev. Lett.* **95** (2005) 052002, arXiv:hep-lat/0503005.

[56] K. G. Chetyrkin, B. A. Kniehl, and M. Steinhauser, "Strong coupling constant with flavour thresholds at four loops in the MS-bar scheme," *Phys. Rev. Lett.* **79** (1997) 2184–2187, arXiv:hep-ph/9706430.

[57] Q. Mason, H. Trottier, C. Davies, K. Foley, and G. P. Lepage, "The Strong Coupling Constant," *Nucl. Phys. Proc. Suppl.* **140** (2005) 713–715.

[58] **HPQCD** Collaboration, C. T. H. Davies, I. D. Kendall, G. P. Lepage, C. McNeile, J. Shigemitsu, and H. Trottier, "Update: Accurate Determinations of α_s from Realistic Lattice QCD," arXiv:0807.1687 [hep-lat].

[59] C. McNeile, C. T. H. Davies, E. Follana, K. Hornbostel, and G. P. Lepage, "High-Precision c and b Masses, and QCD Coupling from Current-Current Correlators in Lattice and Continuum QCD," arXiv:1004.4285 [hep-lat].

[60] S. Bethke, "The 2009 World Average of $\alpha_s(M_Z)$," *Eur. Phys. J.* **C64** (2009) 689–703, arXiv:0908.1135 [hep-ph].

[61] E. B. Gregory *et al.*, "B spectroscopy with NRQCD and HISQ," arXiv:0911.2133 [hep-lat].

[62] E. B. Gregory *et al.*, "A Prediction of the B_c^* mass in full lattice QCD," *Phys. Rev. Lett.* **104** (2010) 022001, arXiv:0909.4462.

[63] **HPQCD** Collaboration, I. F. Allison *et al.*, "Mass of the B/c meson in three-flavor lattice QCD," *Phys. Rev. Lett.* **94** (2005) 172001, arXiv:hep-lat/0411027.

[64] **HPQCD** Collaboration, E. B. Gregory *et al.*, "Precise B, B_s and B_c meson spectroscopy from full lattice QCD." Unpublished, 2010.

[65] E. Mueller. PhD thesis, University of Edinburgh, 2009.

[66] C. Bernard *et al.*, "Tuning Fermilab Heavy Quarks in 2+1 Flavor Lattice QCD with Application to Hyperfine Splittings," arXiv:1003.1937 [hep-lat].

[67] M. B. Oktay and A. S. Kronfeld, "New lattice action for heavy quarks," *Phys. Rev.* **D78** (2008) 014504, arXiv:0803.0523 [hep-lat].

[68] **CLEO** Collaboration, J. L. Rosner *et al.*, "Di-electron widths of the Upsilon(1S,2S,3S) resonances," *Phys. Rev. Lett.* **96** (2006) 092003, arXiv:hep-ex/0512056.